Cranfield University

Mark Tillman

Effect of constrained sintering on the piezoelectric properties of PZT thick films.

School of Applied Science

PhD

Academic Year: 2011-2012

Supervisor: Prof. Rob Dorey

February 2012

Cranfield University

School of Applied Science

PhD

Academic Year: 2011-2012

Mark Tillman

Effect of constrained sintering on the piezoelectric properties of PZT thick films.

Supervisor: Prof. Rob Dorey

February 2012

© Cranfield University, 2012. All rights reserved. No part of this publication may be reproduced without the written permission of the copyright holder.

Acknowledgements

First and foremost I would like to thank my supervisor Prof. Rob Dorey for his patient and insightful guidance without which I could not have completed this thesis. My thanks go to the entire Microsystems and Nanotechnology group, in particular the kind support during the experimental work from Dr. Chris Shaw, Mr. Andrew Stallard and Mr. Matthew Taunt. I would also like to thank my friends in the group for the morale and academic support throughout this work; Dr. Joe Briscoe, Mr. Matt Hockley, Dr. Paul Jones, Dr. Glenn Leighton, Mr. Tony Lusiola, Mr. Andy Pickwell and Mr. Matt Stock.

Special thanks go to my parents Jane and Martin, my brother Paul and sister Ellen for the love, support and friendship through the years. My thanks also go to Granny, Grandad, Uncle Stephen, Auntie Sue and cousins.

My gratitude and thanks is extended to all of my fantastic friends, especially: Mr. Adrian Bayliss, Mr. Mathew Baker, Mr. Jason Buckley, Miss. Joanna Coleman, Mr. Nick Collis, Mr. Mark Cram, Miss. Sam Ginnelly, Mr. Tom Halliday, Mrs. Laura Martin-Read, Mr. Nathan Martin-Read, Mr. Marcus Richardson, Mr. Adam Scoggins, Mr. Byron Slater, Mr. Mike Stockdale and Mr. Gareth Vipers. My thanks also go to all those who have played the great sport of Rugby with me at Cranfield University and Bletchley Rugby Club.

Finally, I would like to thank the financial support from the EPSRC and Cranfield University.

Abstract

This thesis concerns the processing of thick lead zirconate titanate (PZT) films integrated with rigid substrates. The aim was to better understand the evolution of the microstructure, stress, and electrical properties of the films under constrained sintering conditions. This is an important process to understand because of the degrading effects that constrained sintering has on PZT films, which are employed vastly in commercial applications. It is hypothesised that the better understandings can lead to the development of PZT films that exhibit superior dielectric and piezoelectric properties than those in current production. The shrinkage of PZT films was examined in order to better understand the ways in which the rigidity of the substrate affects densification during sintering. This was done by processing isolated regions of PZT film on silicon substrates. These were sintered using a halogen bulb which exhibited a spot at a temperature of 725°C and with a ramp rate of less than 10 seconds. In this way the sintered regions could be 'frozen' mid sintering. The shrinkage of the films was determined at various sintering times. It was found that film shrinkage had finished within 2 minutes of sintering. The evolution of the constrained films during sintering was then examined as a function of the microstructure, stress and electrical property development. It was found that the grain sizes and electrical properties increased within 2 minutes of sintering. However, at longer sintering times there was a degradation of the films. Furthermore, tensile stresses developed during sintering which had degrading effects. This work was expanded upon by motioning the PZT films in a single line scan through the sintering spot to sinter larger areas of the film in one motion. This resulted in a high control over the sintering times, which was vital as the highest electrical properties were found at short sintering times. Next it was examined if the electrical properties could be further increased by applying a compressive stress. It was found that the dielectric properties increased as a result of increased domain wall vibrations. However, there was a decrease in domain reorientation during poling as a result of the effect of the compressive stress, thus the piezoelectric properties reduced. The evolution of PZT films under constrained sintering was better understood as a result of these studies, and led to the development of a sintering method in which the dielectric and piezoelectric properties were increased.

Nomenclature

1, 2, 3	-	Directional vectors
4, 5, 6	-	Spin vectors
2-ME	-	2- methoxyethanol
A	-	Area of plate capacitors
$BaTiO_3$	-	Barium Titanate
C	-	Capacitance
CTE	-	Coefficient of thermal expansion
d	-	Piezoelectric coefficient relating to the mechanical strain of a material with an applied electric field
D	-	Dielectric displacement
e	-	Piezoelectric coefficient relating to the mechanical stress of a material with an applied electric field
E	-	Young's modulus
E_c	-	Coercive field exhibited by a ferroelectric material
E_F	-	Applied electric field
EGS	-	Ethylene glycol based PZT

EHDA	-	Electrohydrodynamic atomisation
FIB	-	Focused Ion Beam
FWHM	-	Full width half maximum
g	-	Piezoelectric coefficient relating to the open circuit electric field of a material with an applied mechanical stress
h	-	Piezoelectric coefficient relating to the open circuit electric field of a material with an applied mechanical strain
H_d	-	Greatest thickness
L	-	Separation between capacitor plates
MEMS	-	MicroElectroMechanical Systems
MPB	-	Morthotropic Phase Boundary
NS	-	PZT without sintering aids
P	-	Induced polarisation
P_r	-	Remnant polarisation exhibited by a ferroelectric material
P_s	-	Spontaneous polarisation exhibited by a ferroelectric material
PZT	-	Lead zirconate titanate
QF1	-	Quality factor 1

QF2	-	Quality factor 1
R_0	-	Initial radius of curvature
R	-	Radius of curvature
R_p	-	Parallel resistance in a circuit
R_s	-	Series resistance in a circuit
R_{ss}	-	Radius of the sintering spot
S	-	Induced strain
s^E	-	Elastic compliance
SEM	-	Scanning Electron Microscope
s_n	-	Separation between the line scans.
T	-	Temperature
Tanδ	-	Dielectric loss
t_s	-	Substrate thickness
t_f	-	Film thickness
W_n	-	Width of the sintering spot
X	-	Applied stress

x	-	Strain
x_n	-	Width of the sintering spot away from the centre of the spot
XRD	-	X-ray diffraction
z	-	Distance between the edges of a beam
δ_x	-	Displacement of a beam.
θ_0	-	Bragg peak position in an XRD trace of an unstressed system.
2θ	-	Bragg peak position in an XRD trace of a stressed system
Ψ	-	Sample tilt
ε_r	-	Relative permittivity
ε_0	-	Permittivity of free space
σ	-	Stress
ω	-	Angular frequency
$\omega(0)$	-	Stress free phonon mode in Raman spectroscopy
$\omega(\sigma)$	-	Stress phonon mode in Raman spectroscopy
υ	-	Poisson’s ratio

Table of contents

ACKOWLEDGEMENTS	i
ABSTRACT	ii
NOMENCLATURE	iii
TABLE OF CONTENTS	vii
LIST OF FIGURES	xii
LIST OF EQUATIONS	xx
CHAPTER 1: INTRODUCTION TO THE THESIS	**Pg. 1**
1.1 Background	Pg. 2
1.2 Aims and objectives	Pg. 3
1.3 Thesis structure	Pg. 3
CHAPTER 2: LITERATURE REVIEW	**Pg. 4**
2.1 Introduction	Pg. 5
2.2 Dielectric materials	Pg. 5
2.3 Piezoelectric materials	Pg. 6
2.3.1 The piezoelectric effect	Pg. 6
2.3.2 Crystal classes	Pg. 7
2.3.3 Piezoelectric equations	Pg. 7
2.4 Ferroelectric materials	Pg. 8
2.4.1 Perovskite crystal structure	Pg. 8
2.4.2 Domain formation	Pg. 10
2.4.3 Poling	Pg. 11
2.4.4 Doping	Pg. 11
2.4.5 Hysteresis loops	Pg. 12
2.5 An introduction to PZT	Pg. 13
2.5.1 Introduction	Pg. 13
2.5.2 Crystal structure	Pg. 13

2.5.3 Domain formation in PZT Pg. 14
2.6 Processing PZT Pg. 16
2.6.1 Solid state synthesis Pg. 16
2.6.2 Chemical synthesis Pg. 16
2.6.3 Sol-gel processing Pg. 17
2.6.4 Composite production Pg. 18
2.7 PZT film fabrication Pg. 19
2.7.1 Dip coating Pg. 19
2.7.2 Spin coating Pg. 20
2.7.3 Electrohydrodynamic atomisation Pg. 20
2.8 Free sintering Pg. 22
2.8.1 Preparation prior to sintering Pg. 22
2.8.2 Densifying sintering mechanisms Pg. 22
2.8.3 Non-densifying sintering mechanisms Pg. 23
2.8.4 Lead loss Pg. 25
2.8.5 Sintering aids Pg. 25
2.9 Constrained sintering Pg. 27
2.9.1 Sintering restrictions Pg. 28
2.9.2 Origin of stress Pg. 28
2.9.3 Stress relaxations Pg. 29
2.9.4 Residual stress Pg. 31
2.10 Measurement of stress Pg. 32
2.10.1 The Stoney equation Pg. 33
2.10.2 X-Ray diffraction Pg. 34
2.10.3 Raman spectroscopy Pg. 35
2.11 Applications of piezoelectrics Pg. 36

CHAPTER 3: METHODOLOGY Pg. 43

3.1 Introduction Pg. 44
3.2 PZT fabrication processes Pg. 44
3.2.1 PZT sol Pg. 44

3.2.2 PZT slurry Pg. 45
3.3 Film deposition procedures Pg. 46
3.3.1 Electrohydrodynamic atomisation Pg. 46
3.3.2 Spin coating Pg. 49
3.4 PZT island fabrication Pg. 50
3.5 Sintering Pg. 52
3.5.1 Halogen bulb spot temperature Pg. 52
3.5.2 Spot sintering Pg. 53
3.5.3 Rastering sintering Pg. 53
3.6 Property-stress relationship Pg. 54
3.7 Electrical property characterisation Pg. 56
3.7.1 Dielectric testing Pg. 56
3.7.2 Poling and d_{33} measurements Pg. 56
3.8 Microstructural characterisation Pg. 57
3.8.1 FIB milled cross sections Pg. 57
3.8.2 SEM imaged cross sections Pg. 57
3.8.3 XRD stress analysis Pg. 57

CHAPTER 4: THICKNESS SHRINKAGE OF CONSTRAINED PZT THICK FILMS Pg. 59

4.1 Introduction Pg. 60
4.2 Calculation of shrinkage Pg. 60
4.3 Comparisons of shrinkage Pg. 65
4.4 Disparities in pyrolysation Pg. 68
4.5 Shrinkage due to sintering Pg. 69
4.5.1 Set 1 Pg. 69
4.5.2 Set 2 Pg. 71
4.5.3 Comparisons of set 1 and set 2 Pg. 74
4.6 Chapter conclusions Pg. 75

CHAPTER 5: DIELECTRIC AND PIEZOELECTRIC PROPERTIES OF CONSTRAINED PZT THICK FILMS Pg. 76

5.1 Introduction Pg. 77
5.2 Constrained sintering of EGS films Pg. 77
5.3 EGS films: Region 1 Pg. 78
5.3.1 Region 1: Densification Pg. 80
5.3.2 Region 1: Grain growth Pg. 83
5.3.3 Region 1: Residual stress Pg. 88
5.3.4 Region 1: Conclusions Pg. 91
5.4 Effect of liquid phase sintering Pg. 91
5.5 EGS films: Region 2 Pg. 96
5.6 EGS films: Region 3 Pg. 99
5.7 Constrained sintering of 2-ME films Pg. 99
5.7.1 2-ME films: Relative permittivity Pg. 101
5.7.2 2-ME films: d_{33} Pg. 104
5.8 Chapter conclusions Pg. 107

CHAPTER 6: RASTERING SINTERING OF CONSTRAINED PZT THICK FILMS Pg. 109

6.1 Introduction Pg. 110
6.2 Effect of stage speed on the electrical properties Pg. 110
6.2.1 Slow speeds Pg. 111
6.2.2 Mid speeds Pg. 113
6.2.3 Quick speeds Pg. 114
6.2.4 Conclusions Pg. 115
6.3 Comparison of spot and line scan sintering Pg. 115
6.4 Effect of rastering sintering on the electrical properties Pg. 119
6.4.1 Electrical properties Pg. 119
6.4.2 Sintering method analysis Pg. 122
6.4.3 Conclusions Pg. 128

6.5 Chapter conclusions Pg. 129

CHAPTER 7: STRESS INDUCED DOMAIN SWITCHING Pg. 130

7.1 Introduction Pg. 131
7.2 Effect of a compressive stress on dielectric properties Pg. 131
7.3 Domain switching Pg. 135
7.4 Effect of a compressive stress on piezoelectric properties Pg. 138
7.5 Conclusions Pg. 142

CHAPTER 8: CONCLUSIONS AND FUTURE WORK Pg. 144

8.1 Introduction Pg. 145
8.2 Evolution of PZT films under constrained sintering Pg. 145
8.2.1 Region 1 Pg. 145
8.2.2 Region 2 Pg. 146
8.2.3 Region 3 Pg. 147
8.3 Effect of constrained sintering on electrical properties Pg. 147
8.4 Conclusions Pg. 148
8.5 Future work Pg. 148

REFERENCES Pg. 151

List of Figures

Fig. 1. Vectors associated with piezoelectric coefficients.

Fig. 2. ABO_3 perovskite crystal unit cell.

Fig. 3. The domain orientations of an ideal single crystal.

Fig. 4. Single crystal with 180˚ and 90˚ orientated domains and boundaries.

Fig. 5. Hysteresis loop of a ferroelectric material, displaying polarisation of the material as a function of the applied electric field (Damjanovic, 1998).

Fig. 6. Phase diagram of PZT

Fig. 7. Illustration of possible domain formations within grains.

Fig. 8. Schematic of six differing sintering mechanisms at grain and pore intercepts in free sintering (Rahaman, 1995).

Fig. 9. Schematic of constrained sintering.

Fig. 10. Illustration of a piezoelectric material activated gas igniter.

Fig. 11. Schematic of an ultrasonic transducer activated by a piezoelectric material.

Fig. 12. A commercial cantilever bi-morph accelerometer (www.metrolog.net), and an illustration of an accelerometer used an airbag systems when decelerating.

Fig. 13. Schematic of energy harvester in the d_{33} mode (Jeon et al., 2005).

Fig. 14. Schematic of the EHDA deposition process.

Fig. 15. The measured surface profile of a pyrolysed single line of deposited EGS slurry, at a flow rate of 0.01ml/h and a stage speed of 5.0mm/s.

Fig. 16. Quality factors as a function of stage separation, at a flow rate of 0.01ml/h and a stage speed of 5.0mm/s.

Fig. 17. The schematic of PZT thick film deposition using the spin coating process.

Fig. 18. Schematic of the photoresist mould processing procedure**.**

Fig. 19. Variations in the temperature of the sintering spot as a function of the applied current.

Fig. 20. Schematic of the four point bend rig with a stress applied on the beam.

Fig. 21. Schematic of a stressed beam with mathematical notations.

Fig. 22. Surface profile of a pyrolysed, un-sintered PZT island.

Fig. 23. Surface profile of a developed photoresist mould.

Fig. 24. Surface profile of a PZT island, un-sintered then sintered for 5 minutes, with a polynomial curve fit.

Fig. 25. Surface profile of a PZT island, un-sintered then sintered for 5 minutes, with a linear fit.

Fig. 26. Variations in the thicknesses and the associated standard deviation of two sets of un-sintered PZT islands as a function of the time that a sintering temperature of 725ºC was to be applied for later.

Fig. 27. Variations in the shrinkage and the associated standard deviation of two sets of sintered PZT islands as a function of the time at a sintering temperature of 725ºC.

Fig. 28. Optical microscope images of the top surface of a PZT island pyrolysed at a) 300˚C, followed by at b) 400˚C.

Fig. 29. Variations in the thicknesses and the associated standard deviation of the un-sintered and sintered PZT islands set 1 as a function of the time at a sintering temperature of 725ºC.

Fig. 30. Variations in the thicknesses and the associated standard deviation of the un-sintered and sintered PZT islands set 2 as a function of the time at a sintering temperature of 725ºC.

Fig. 31. Surface profile of a PZT island in set 2 un-sintered and subsequently sintered for 1 minute at 725°C.

Fig. 32. Surface profile of a PZT island in set 2 un-sintered and subsequently sintered for 7.5 minutes at 725°C.

Fig. 33. SEM micrographs taken at a 45º angle of FIB cross sections of PZT islands sintered at 725˚C for a) 3 minutes, set 1, b) 3 minutes, set 2, c) 5 minutes, set 1, and d) 5 minutes, set 2, respectively.

Fig. 34. Variations in relative permittivity and the associated standard deviation of EGS films as a function of sintering time at a processing temperature of 725˚C.

Fig. 35. Variation in d_{33} and the associated standard deviation of EGS films as a function of sintering time at a processing temperature of 725ºC.

Fig. 36. SEM micrographs of FIB developed cross sections of EGS films sintered at 725˚C for a) 0 minutes, b) 0.75 minutes, c) 1 minute, and d) 2 minutes, respectively.

Fig. 37. Variations in dielectric loss and the associated standard deviation of the EGS films as a function of sintering time at a processing temperature of 725˚C.

Fig. 38. SEM images of cross sections of the EGS films sintered at 725˚C for a) 0 minutes, b) 0.75 minutes, c) 1 minute, and d) 2 minutes, respectively.

Fig. 39. Variations in the grain sizes and the associated standard deviation of the EGS films as a function of sintering time at a processing temperature of 725˚C.

Fig. 40. XRD determined 2θ peak position as a function of sample tilt for an EGS film sintered for 5 minutes.

Fig. 41. Variations in the XRD determined gradients, proportional to the residual stress of the EGS films, as a function of sintering time at a processing temperature of 725˚C.

Fig. 42. Variations in relative permittivity and the associated standard deviation of the NS films as a function of sintering time at a processing temperature of 725˚C.

Fig. 43. Variations in d_{33} and the associated standard deviation of the NS films as a function of sintering time at a processing temperature of 725ºC.

Fig. 44. SEM micrographs of FIB developed cross sections of the NS films sintered at 725˚C for a) 0 minutes, b) 1 minute, and c) 2 minutes, respectively.

Fig. 45. Variations in dielectric loss and the associated standard deviation of the NS films as a function of sintering time at a processing temperature of 725˚C.

Fig. 46. SEM micrographs of FIB developed cross sections of the EGS films sintered at 725˚C for a) 3 minutes, b) 7.5 minutes, c) 15 minutes, and d) 20 minutes, respectively.

Fig. 47. SEM micrographs of FIB developed cross sections of the NS films sintered at 725˚C for a) 10 minutes, and b) 20 minutes, respectively.

Fig. 48. SEM micrographs of FIB developed cross sections of the EGS films sintered at 725˚C for a) 30 minutes, and b) 60 minutes, respectively.

Fig. 49. Variations in relative permittivity and the associated standard deviation of the 2-ME films as a function of sintering time at a processing temperature of 725˚C.

Fig. 50. Variations in d_{33} and the associated standard deviation of the 2-Me films as a function of sintering time at a processing temperature of 725ºC.

Fig. 51. SEM micrographs of FIB developed cross sections of the 2-ME films sintered at 725˚C for a) 0 minutes, b) 0.75 minutes, c) 1 minute, and d) 2 minutes, respectively.

Fig. 52. SEM micrographs of FIB developed cross sections of the 2-ME films sintered at 725˚C for a) 5 minutes, b) 10 minutes, c) 25 minutes, and d) 30 minutes, respectively.

Fig. 53. Variations in the XRD determined gradients, proportional to the residual stress of the 2-ME films, as a function of sintering time at a processing temperature of 725˚C.

Fig. 54. Variations in relative permittivity and d_{33} and the associated standard deviation as a function of the applied stage speed at a processing temperature of 725ºC.

Fig. 55. SEM micrographs cross sections of films sintered at 725˚C at stage speeds of a) 0.01mm/s and b) 0.04mm/s, respectively.

Fig. 56. Variations in the grain size and the associated standard deviation as a function of stage speed at a processing temperature of 725˚C.

Fig. 57. SEM cross sections images of films sintered to 725˚C at stage speeds of a) 0.10mm/s, and b) 0.14mm/s, respectively.

Fig. 58. SEM cross sections images of films sintered to 725˚C at stage speeds of a) 0.20mm/s, and b) 0.30mm/s, respectively.

Fig. 59. Predicted sintering times determined through approximate spot size and comparisons with results in Chapter 5.

Fig. 60. Variations in relative permittivity and the associated standard deviation as a function of stage separation at a stage speed of 0.10mm/s and a processing temperature of 725˚C.

Fig. 61. Variations in d_{33} and the associated standard deviation as a function of stage separation at a stage speed of 0.10mm/s and a processing temperature of 725ºC.

Fig. 62. SEM micrographs cross sections of films sintered at 725˚C using separations of a) 1.0mm, b) 2.0mm, c) 5.0mm, and d) 7.0mm respectively.

Fig. 63. Variations in the grains sizes and the associated standard deviation as a function of separation at a stage speed of 0.10mm/s and a processing temperature of 725˚C.

Fig. 64. Schematic of a line scan sintered film, with evaluations of sintering times at different regions.

Fig. 65. Schematic of rastering sintering using a separation of a) 1.5mm, b) 2.0mm, c) 2.5mm, d) 5.0mm, and e) 7.0mm.

Fig. 66. Schematic used to determine sintering spot widths.

Fig. 67. Sintering time across a 5mm region using a stage speed of 0.10mm/s and a separation of 1.5mm.

Fig. 68. Sintering time across a 5.0mm region using a stage speed of 0.10mm/s and a separation of 2.0mm.

Fig. 69. Sintering time across a 5.0mm region using a stage speed of 0.10mm/s and a separation of 2.5mm.

Fig. 70. Sintering time across a 5.0mm region using a stage speed of 0.10mm/s and a separation of 3.5mm.

Fig. 71. Variations in relative permittivity of a 2-ME PZT thick film sintered for 7.5 minutes as a function of applied compressive stress.

Fig. 72. Variations in the gradient of the linear fit of relative permittivity of 2-ME PZT thick films as a function of sintering time.

Fig. 73. Variations in relative permittivity of 2-ME PZT thick films unstressed, at a compressive stress of 8GPa, and the difference at these states as a function of sintering time.

Fig. 74. Variations in the gradient of the linear fit of dielectric loss of 2-ME PZT thick films as a function of sintering time.

Fig. 75. Variations in dielectric loss of 2-ME PZT thick films unstressed, at a compressive stress of 8GPa, and the difference at these states as a function of sintering time.

Fig. 76. Illustration of possible 180° domain orientations in the A) x direction, and B) y direction; 90° domain orientations in the C) x-y directions, D) x-z directions and E) y-z directions; and F) 180° domain orientations in the z direction.

Fig. 77. Vibration, Δl, of a 90° domain boundary.

Fig. 78. Variations in the gradient of the linear fit of d_{33} of 2-ME PZT thick films as a function of sintering time.

Fig. 79. Variations in d_{33} of 2-ME PZT thick films unstressed, at a compressive stress of 8GPa, and the difference at these states as a function of sintering time.

Fig. 80. Illustration of ferroelastic and ferroelectric domains re-orientated during poling.

Fig. 81. Illustration of ferroelastic and ferroelectric domains re-orientated during poling and a compressive stress.

List of Equations

Equation 1:

$$C = \frac{\varepsilon_r \varepsilon_0 A}{l}$$

Equation 2:

$$tan\delta = \frac{1}{\omega C R_p} \qquad tan\delta = R_s \omega C$$

Equation 3:

$$\mathrm{P}_i = \mathrm{d}_{ijk} \sigma_{jk}$$

Equation 4:

$$\mathrm{S}_{jk} = \mathrm{d}_{ijk} \mathrm{E}_i$$

Equation 5:

$$\left(\frac{\partial x}{\partial E}\right)_{X,T} = d$$

$$\left(\frac{\partial x}{\partial D}\right)_{X,T} = g$$

$$-\left(\frac{\partial X}{\partial E}\right)_{x,T} = e$$

$$-\left(\frac{\partial X}{\partial D}\right)_{x,T} = h$$

Equation 6:

$$(d_{33})_{meas} = d_{33} - 2d_{31}\frac{s_{13}^{E}}{(s_{11}^{E} + s_{12}^{E})}$$

Equation 7:

$$\sigma = \left(\frac{\mathrm{E}}{1-\upsilon}\right)\frac{\mathrm{t_s^2}}{6_{\mathrm{tf}}}\left(\frac{1}{\mathrm{R}} - \frac{1}{\mathrm{R_0}}\right)$$

Equation 8:

$$\partial(sin^2\Psi) = -\frac{\frac{E}{2(1+\upsilon)}.cot\theta_0.\frac{\pi}{180}}{\sigma}.\partial(2\theta)$$

Equation 9:

$$\omega(\sigma) = \omega(0) - \frac{\partial\omega}{\partial\sigma}.\sigma$$

Equation 10:

$$Quality\ factor\ 1 = \frac{Full\ Width\ Half\ Maximum}{H_d}$$

Equation 11:

$$Quality\ factor\ 2 = greatest\ thickness - \ lowest\ thickness$$

Equation 12:

$$R = \frac{\delta_x}{2} + \left(\frac{z}{2}\right)^2 \left(\frac{1}{2\delta_x}\right)$$

Equation 13:

$$m = -\frac{\sigma}{\frac{E}{2(1+\upsilon)} . \cot\theta_0 . \frac{\pi}{180}}$$

Equation 14:

$$W_n = 2\ X \sqrt{(R_{ss}^2 - [s_n - x_n]^2)}$$

Chapter 1

Introduction

1.1 Background

Piezoelectric materials are widely used in products because of their capability to transform electrical energy into mechanical energy, and vice versa. The most widely used piezoelectric material is PZT. This is because it exhibits superior dielectric and piezoelectric properties, energy conversion efficiency and is of low relative cost. PZT products are generally manufactured from PZT powders and then formed into bulk structures through pressing, sintering and machining. However, transducer, capacitor, sensor and actuator applications integrated with circuits are required in the electronic industry. PZT devices can fulfil these roles, but miniaturisation of the devices is required. To produce devices of the required size, bulk ceramics can be diced or polished. However, material is wasted and the obtainable sizes may still be too large. So PZT films at the micrometer or sub-micrometer scale have been considerably researched. It is required that these films are deposited onto substrates. The material used for substrates is generally silicon, because of the simplicity of integrating the devices with silicon-based circuitry. PZT film devices have been used extensively in industry, a particular example is accelerometer applications in automobile air bag deployment. However, there are issues of concern during film processing that require extensive research in order to produce the next generation of industry applied PZT films. The most notable problem arises during the sintering of PZT films, which is conducted to densify the film and produce the required microstructure. In these cases sintering is conducted while the film is bonded to the rigid substrate. The rigidity of the substrate opposes the film sintering mechanisms, thus reducing the achievable density and resulting in the generation of tensile stresses within the film. Therefore, serious degradation of the film can arise during sintering, reducing the stability of the structure and the obtainable piezoelectric properties. To increase the functionality of PZT films and the potential market share, the effect of the substrate on the sintering mechanisms of PZT films requires closer inspection. It is hypothesised that by adjusting the sintering conditions, a state in which the required microstructure is reached while minimising stresses can be found.

1.2 Aims and objectives

The aim of this project is to develop an understanding of the evolution of the microstructure and the stress generated during the sintering of PZT films integrated with rigid silicon substrates. To achieve this aim PZT thick films were prepared that were sintered using near instantaneous ramp and cooling rates, so that the processed film could be examined mid-sintering. At various sintering times the microstructure development was analysed by measuring the film densities and grain sizes. Furthermore, the stress generated during sintering was monitored. Furthermore, the effects of microstructural evolution and stress on the functional properties were evaluated. Knowledge gained from these studies was then used to identify the optimum sintering conditions that resulted in the highest properties in order to process large areas of film.

1.3 Thesis structure

This thesis is divided into 8 Chapters. This introduction is the first chapter. This is followed by the literature review, where background information on dielectric, piezoelectric and ferroelectric materials is presented. Additionally, the chemical production, deposition, sintering and the stress of PZT films are discussed. Finally, the applications of PZT films in commercial products are outlined. In Chapter 3 the experimental procedures used in this project are summarised. In Chapters 4 to 7 the experimental results and discussions are presented. In Chapter 4 the shrinkage of PZT thick films are examined as a function of sintering time. In Chapter 5 the evolution of the dielectric and piezoelectric properties of PZT thick films as a function of sintering time are examined and the variations in the electrical properties analysed as a function of microstructural and stress development. In Chapter 6 the understandings of constrained sintering are further developed as large areas of PZT thick films were sintered. In Chapter 7 the effect of applied compressive stresses on the electrical properties of processed PZT thick films is studied to further understand the effect of stress. Finally, conclusions of the work conducted are presented in Chapter 8, along with ideas for further work.

Chapter 2

Literature review

2.1 Introduction

In this chapter background information that is pertinent to this thesis is presented. Firstly, there is an introductory explanation of dielectric, piezoelectric and ferroelectric materials. The focus then turns towards the background information of PZT. This is followed by the fabrication of PZT powders, bulk ceramics and films with the relevant processing routes examined. In the subsequent section free and constrained sintering is examined along with origin of stress within films and stress measurement methods. Finally, there is a broad discussion of the applications of PZT ceramics.

2.2 Dielectric materials

Dielectric materials have been comprehensively explained by Moulson and Herbert (1989). They exhibit insulating capabilities and thus are used within electrical circuits to separate conductive elements. Additionally, a dielectric also exhibits capacitor capabilities. The ability of a capacitor to store a charge in a given area is directly proportional to the materials relative permittivity, ε_r. For a parallel plate capacitor the capacitance C is given by equation 1.

$$C = \frac{\varepsilon_r \varepsilon_0 A}{l}$$ Equation 1

Where A is the area of the plates, l the separation between the plates, and ε_0 is the permittivity of free space. Furthermore, a dielectric can be defined as a material with a high electrical resistivity, whereby there is a high resistance to a d.c. current. Thus, a role in which dielectrics can fulfil is the decoupling of a.c. and d.c. signals. Ideally the a.c. electric field will not dissipate. However, in practice energy dissipation can occur due to electrode resistance, d.c. leakage resistance and the materials dielectric loss, tanδ. The dielectric loss is an inherent property of a material and is described by equation 2.

$$tan\delta = \frac{1}{\omega C R_p} \qquad tan\delta = R_s \omega C$$ Equation 2

Where R_p is resistance parallel and R_s is resistance in series to the capacitor, and ω is the angular frequency. The dielectric loss of a material increases when there are increases in defects at the domain wall, which can result in the 'pinning' of domains. As a result there is a reduction in the domain wall motion that contributes to the permittivity. Polarisation loss also occurs as the polarisation of ions with the application of an electric field does not occur instantaneously as there is an associated inertia. The ions can be considered to be bound to an equilibrium position by springs with a restoration force.

Another factor to consider is that of dielectric breakdown. This occurs as a dielectric is required to absorb large amounts of charge, but at a porous region the electric field is greater than at dense surrounding regions, this steadily increases until the electric field discharges which results in heat and phonons generated. Furthermore, charges can propagate over interconnecting porous sites or cracks resulting in a direct electrical connection through the material to the separated electrodes. To improve the efficiency of a dielectric material the ability to store a charge and to insulate between two conductive elements must be maximised. These are generally defined by relative permittivity, d.c. resistance and dielectric loss.

2.3 Piezoelectric materials

2.3.1 The piezoelectric effect

Piezoelectricity is a term to describe a crystal which is a subclass of dielectrics where the mechanical stress and strain is coupled with the electrical polarisation of the material. The accumulated charge is proportional to an applied stress and is known as the direct piezoelectric effect. The indirect effect is described by the development of a strain that is proportional to an applied electric field, thus the material will undergo a change in dimensions when polarised (Moulson and Herbert, 1989). The direct and indirect effects are described by equation 3 and 4, respectively.

$$P_1 = d_{123}\sigma_{23}$$ Equation 3

$$S_{23} = d_{123}E_{F1}$$ Equation 4

Where P is the induced polarisation of the material, d is piezoelectric tensor, σ is stress, S is the induced strain and E_F is applied electric field on the material (Damjanovic, 1998).

2.3.2 Crystal classes

A crystal cell of a material can be cubic, hexagonal, orthorhombic, monoclinic, tetragonal, triclinic or trigonal. These are divided into 32 crystal classes depending on the centre of symmetry. Of these 32, 11 are symmetrical and consequently are non-piezoelectric because an applied stress results in a symmetrically distributed charge. The 21 remaining classes are non-centrosymmetric and are therefore piezoelectric. 10 of these posses a unique polar axis, whereby a change in temperature results in a change in polarisation, this is called pyroelectricity (Moulson and Herbert, 1989).

2.3.3 Piezoelectric equations

The direct and indirect piezoelectric capability of a material is described by equation 5.

$$\left(\frac{\partial x}{\partial E_F}\right)_{X,T} = d$$

$$\left(\frac{\partial x}{\partial D}\right)_{X,T} = g$$

$$-\left(\frac{\partial X}{\partial E_F}\right)_{x,T} = e$$

$$-\left(\frac{\partial X}{\partial D}\right)_{x,T} = h$$

Equation 5

Where D is the dielectric displacement, X is the applied stress, E_F is the applied electric field, x is strain and T is temperature, which is constant (Moulson and Herbert, 1989).

To organise these coefficients qualitatively: the d coefficient describes a mechanical strain which occurs as a result of an applied electric field; g describes the open circuit electric field which occurs as a result of an applied mechanical stress; e describes the mechanical stress that occurs with an applied electric field; and h describes the open circuit electric field which occurs as a result of an applied mechanical strain. The directional vectors 1, 2 and 3, and the spin vectors 4, 5 and 6 are considered when using the coefficients, displayed in Fig. 1. In this thesis only the d coefficient was considered. This is a third rank tensor which reduces to three non-zero constituents, d_{31}, d_{33} and d_{15}. The d_{31} coefficient is measured perpendicular to the applied field and is called the transverse coefficient. The d_{33} is measured parallel to the applied field, and is called the longitudinal coefficient. The d_{15} is the shear coefficient (Damjanovic, 1998).

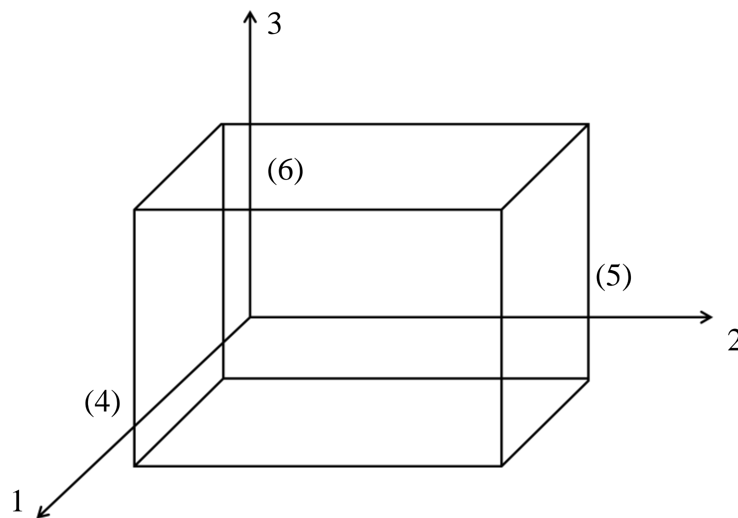

Fig. 1. Vectors associated with piezoelectric coefficients.

2.4 Ferroelectric materials

A ferroelectric material is a subset of piezoelectrics which exhibits a spontaneous polarisation that can be altered by the application of an external electric field.

2.4.1 Perovskite crystal structure

A perovskite crystal structure is pertinent to this thesis as PZT exhibits this structure. This is displayed in Fig. 2 using the ABO_3 structure of Barium titanate ($BaTiO_3$) as an

example. The A corner sharing regions are occupied by Ba^{2+} ions; O^{2-} ions occupy the interstices which share electrons with neighbouring cells; and Ti^{4+} ions occupy the B central position. In this figure the central ion is not displaced, thus there is no dipole direction in the cubic phase being exhibited.

Upon the transition below the Curie temperature the crystal undergoes a phase shift from the paraelectric phase, where are no permanent dipoles, to the ferroelectric phase. This is when there is the formation of an electric dipole as the central ions displace with respect to the Ba^{2+} ions. In the tetragonal phase there are 6 possible dipoles as the central ion shifts up, down, left, right or in and out of the page. In the rhombohedral phase the central ion is displaced along the diagonal towards any of the corner ions, resulting in 8 possible dipole directions. With the displacement of the central ions the shape of the entire cell deforms. For example, when a tetragonal structure is formed as a result of the central ion displacing upwards, the resulting unit cell is tall and narrow. As a consequence of a dipole forming in a unit cell neighbouring unit cells are displaced in the same direction, resulting in a knock on effect forming a region that is similar in dipole orientations, known as a domain (Moulson and Herbert, 1989).

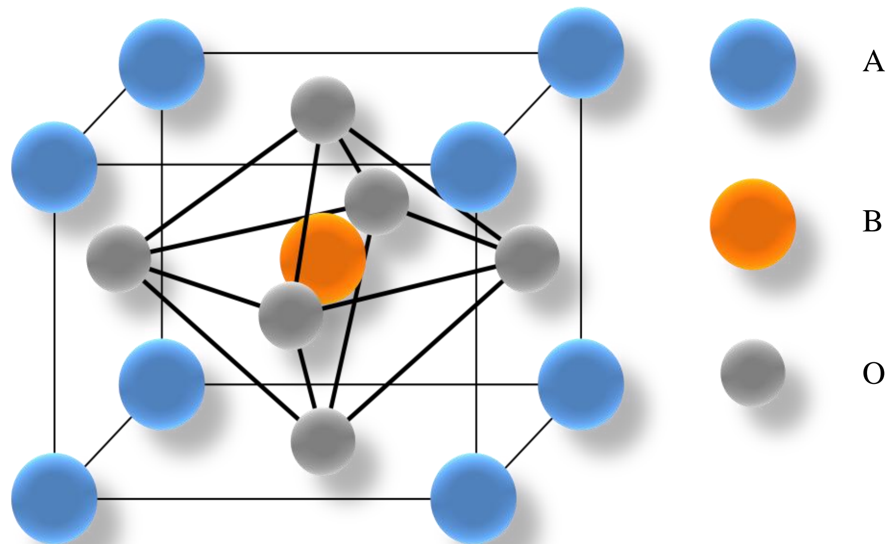

Fig. 2. ABO_3 perovskite crystal unit cell.

2.4.2 Domain formation

Neighbouring domains spontaneously form in opposite directions as the surface electrostatic energies of the material is minimised, consequently the material exhibits zero net charge. To explain domain formation, an ideal $BaTiO_3$ single crystal is taken as an example. The material comprises of two possible domain orientations, which are oppositely orientated and result in a zero net charge, displayed in Fig. 3. The boundaries between each domain, which has certain amount of energy associated with them, are at an 180˚ angle. These boundaries differ only in orientation of the displaced atoms and are called ferroelectric domain walls (Moulson and Herbert, 1989).

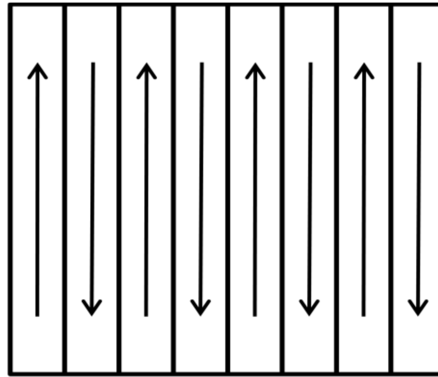

Fig. 3. The domain orientations of an ideal single crystal.

In a non-idealised crystal more complex domain orientations exist. As the domains form, neighbouring material is deformed. For example, when 180º neighbouring domains form in the up tetragonal phase, there are elastic strains between the domains as a consequence. This strain can be relieved by the orientation of a neighbouring domain switching 90º. These 90º domain boundaries differ in both the domain direction and strain, and are known as ferroelastic domain boundaries (Damjanovic, 1998). A structure where the surface electrostatic and elastic energies are minimised, which results in 90˚ and 180˚ domain boundaries, is displayed in Fig. 4.

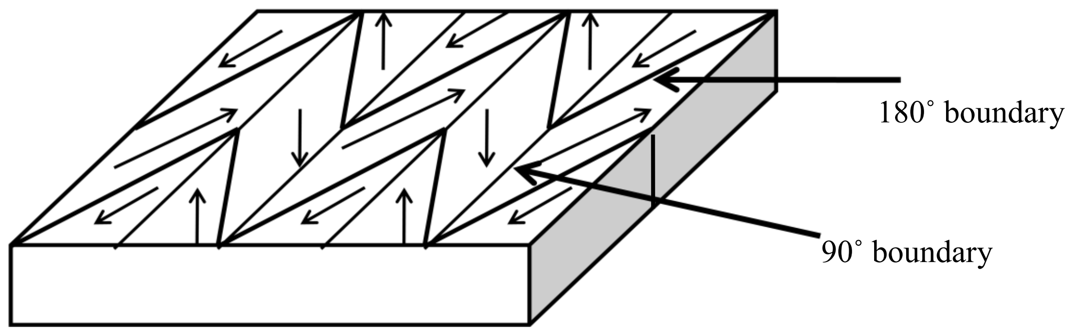

Fig. 4. Single crystal with 180˚ and 90˚ orientated domains and boundaries.

2.4.3 Poling

In order to produce a material with a net polarisation and hence piezoelectric properties, domains need to be aligned. This can be achieved through the application of an electric field (several MV per metre), resulting in the domains aligning with the field. This is conducted alongside gentle heating so that domain re-orientation occurs more readily. Finally, the electric field and heat is steadily removed resulting in the domains becoming 'frozen' in the new aligned positions. This process is called 'poling'.
The polarisation of a material after the poling field is removed is called the remnant polarisation, P_R. The maximum polarisation achievable during poling is restricted by the available domain states, and is defined as a function of spontaneous polarisation, P_s. In a tetragonal polycrystalline ferroelectric with 6 domain states the maximum P_R achievable is $0.83P_S$. In a rhombohedral polycrystalline ferroelectric with 8 domain states the maximum P_R achievable is $0.87P_S$ (Damjanovic, 1998). In practice the achievable polarisation will be lower due to complex domain boundary and stress states.

2.4.4 Doping

Acceptor or donor dopants that penetrate the crystal cell can be added chemically. Dopants can replace the A and B sites in the cell. Dopants that replace the B site central ion will be taken as an example. Acceptor dopants form a 'hard doped' material, which is when an ion of a lower charge replaces the central ion and the resultant charge difference is compensated for by an oxygen vacancy in the unit cell. This generally results in a higher exhibited dielectric constant. However, domains are fixed in position and are difficult to re-orientate. As a result of donor dopants the central ion is replaced by a higher charged ion, forming a 'soft doped' material. Consequently there is the

occurrence of electron vacancies in the unit cell, which can result in higher dielectric losses and lower coercive fields; however, domain re-orientation occurs more readily during poling (Moulson and Herbert, 1989; Damjanovic, 1998; Dorey and Whatmore, 2004b).

2.4.5 Hysteresis loops

All ferroelectric materials exhibit the characteristic of domain polarisation reversal with the application of an electric field. Also a consequence of the domain switching is a non-linear hysteretic loop; an example is presented in Fig. 5. At small electric fields (Fig. 5 A) the polarisation increases linearly, which occurs because the field is not large enough to result in the switching of domains with oppositely directed polarisation. As the electric field increases (Fig. 5 B) oppositely orientated domains start to switch towards the electric field. At larger applied electric fields (Fig. 5 C) the polarisation saturates as opposite polarised domains switch in the direction of the field until a maximum polarisation, known as the spontaneous polarisation, P_s, is reached. As the electric field is reduced hysteresis is observed. At a zero electric field there is a non-zero polarisation, this is known as the remnant polarisation, P_r. To de-polarise the material a negative electric field must be applied, whereby the polarisation exhibited can be reversed up until saturation is reached (Fig. 5 D). The electric field required to cause zero polarisation is known as the coercive field, E_c. The P_r, P_s, E_c and shape of the hysteresis loop is affected by lattice defects, residual stress, mechanical strains and thickness of the material (Moulson and Herbert, 1989; Damjanovic, 1998).

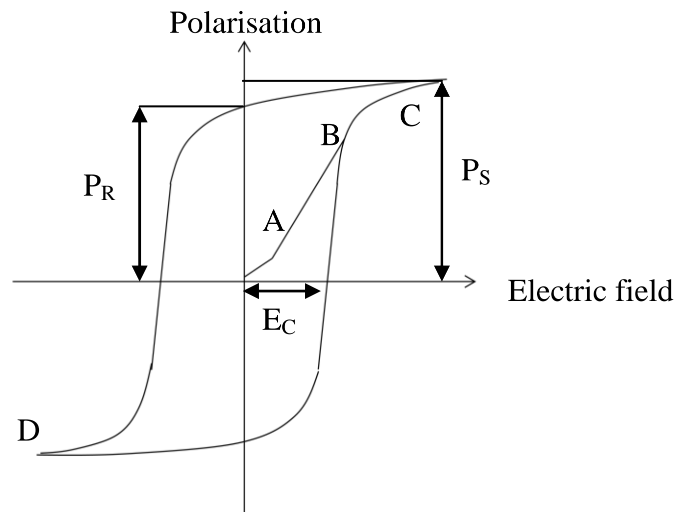

Fig. 5. Hysteresis loop of a ferroelectric material, displaying polarisation of the material as a function of the applied electric field (Damjanovic, 1998).

2.5 An introduction to PZT

2.5.1 Introduction

Barium titanate, developed in the 1940s was the first successful custom man-made piezoelectric material integrated into electrical circuits. The piezoelectric effect of these materials was higher than that found in naturally occurring materials, and the properties could be tailored to specific applications. This then led onto the development of PZT in the 1950s, which was found to have a higher piezoelectric coefficient and energy conversions than barium titanate. Consequently, PZT is the most widespread piezoelectric ceramic used in industry today. PZT ceramics exhibit dielectric, piezoelectric and ferroelectric capabilities. Therefore, the previous discussions are expanded upon to explain how PZT ceramics function (Moulson and Herbert, 1989).

2.5.2 Crystal structure

PZT has a similar perovskite ABO_3 crystal unit cell to that of barium titanate. At the A sites Pb^{2+} ions exist, and at the B sites Ti^{4+}/Zr^{4+} ions exist. The crystal phase of a PZT crystal unit cell is dependent on the ratio of Zr to Ti, and the temperature. The phase diagram of PZT is displayed in Fig. 6. At high temperatures a paraelectric cubic phase exists. During cooling through the Curie temperature of the material dipoles develop

given rise to the ferroelectric phase. At Zr-rich compositions a rhombohedral crystal structure is exhibited, and at Ti-rich compositions a tetragonal crystal structure is exhibited. At room temperature the boundary between phase transitions occurs when there is 52:48 ratio of Zr:Ti. This is called the morphotropic phase boundary (MPB), and materials of this composition have been shown to exhibit a peak in piezoelectric and dielectric properties. One reason for this is that at the MPB 14 polarisation directions are possible; 8 polarisation directions associated with the rhombohedral phase and 6 with the tetragonal phase. PZT crystallised at the MPB therefore may exhibit 14 directions along which the domains may be re-orientated during poling, resulting in a large polarisation (Damjanovic, 1998).

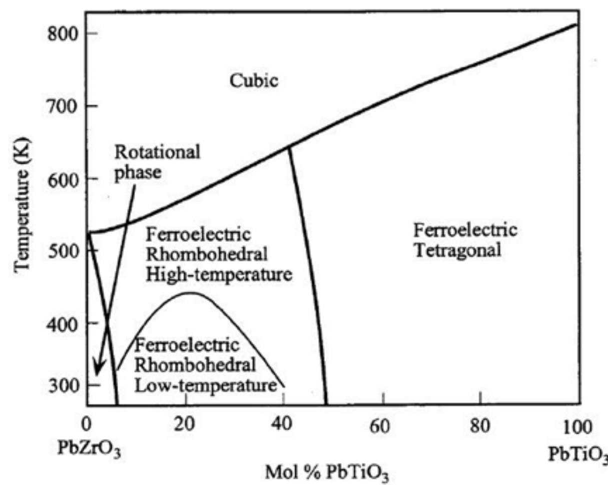

Fig. 6. Phase diagram of PZT (www.doitpoms.ac.uk).

2.5.3 Domain formation in PZT

In PZT the domains exist within the grains, and the width of a domain is proportional to the root of the size of the grain (Moulson and Herbert, 1989; Arlt, 1990). This parabolic relationship between grain and domain sizes suggests that sub-micrometer grains would accommodate a maximum of one domain. However, Randall *et al.* (1998) suggested that domain densities continued to increase with grain sizes under 1μm in bulk materials. Closer examinations of the domain formation in thin PZT films integrated with substrates were conducted by Tuttle *et al.* (1995). It was observed that there were no domain boundaries in grains of sizes lower than 0.2μm, signifying single domain accommodation. At grain sizes of 0.2-1.0μm they observed a 90˚ domain boundary,

thus two domains existing per grain with a ferroelastic domain boundary. Furthermore, at grain sizes greater that 1μm increases in domain accommodation was seen. These domain formations are illustrated in Fig. 7.

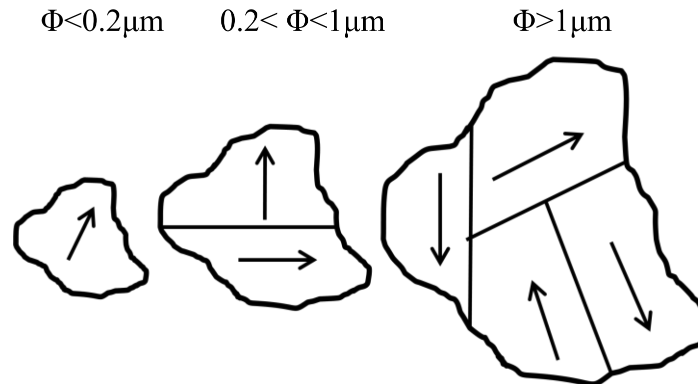

Fig. 7. Illustration of possible domain formations within grains.

The number of domains accommodated in a grain has an effect on the orientation of the domains. It was discussed earlier that ferroelectric and ferroelastic domain boundaries develop to minimise electrostatic and elastic energies. However, this only occurs when there are neighbouring domains. So, in small grains where only a single domain may be accommodated, these boundary effects are not exhibited. This may result in unrelieved domain boundary strains. Additionally, the domain boundary is coupled to the grain wall, resulting in a reduction in the effect of poling. When two domains exist within a grain there is a reduction in the domain boundary strains as a consequence of a ferroelastic domain boundary (Tuttle B.A. et al., 1995). In addition there is a reduction in grain-domain wall coupling, resulting in a greater probability of re-orientation during poling. When multiple domains exist within a grain more complex ferroelectric and ferroelastic domain boundaries develop. This can result in increasingly effective domain re-orientation during poling due to a reduction in inter-domain strains as a consequence of ferroelastic boundaries, and also a reduction in grain-domain wall coupling.

In order to produce PZT ceramics with high piezoelectric capabilities, domain re-orientation during the application of a poling field is required. The efficiency of this is reduced when domain ‘pinning’ occurs. It has already been explained that this can arise

due to grain-domain wall coupling. In addition to this 'pinning' occurs in PZT films as a consequence of an integrated substrate. This is examined more closely in section 2.9.4.

2.6 Processing PZT

There are three main processing routes to manufacture PZT. Firstly, there is the production of PZT powders, which can be formed into bulk materials. Secondly, there is sol-gel, which is a wet chemical solution and can be used to produce films. Finally, sol-gel and powder combinations are used to form a composite material, which has also been used to produce films. These productions routes are discussed in the following section.

2.6.1 Solid state synthesis

The first stage of processing PZT powders is the mixing of stoichiometric amounts of metal oxides. Powders are generally calcined at an intermediate temperature to induce partial ion interdiffusion, followed by sintering at a much higher temperature, typically at 1200-1400˚C to produce full crystallisation (Rahaman, 1995). However, prior to sintering the removal of agglomerates and the reduction of the particle size of the powder can result in higher sintering rates later. This has been done by using ball-milling, which is the motion of inert zirconia milling media through the powder, resulting in a shearing and crushing action. However, the milling media are abraded by a charge and may contaminate the powder, one way around this is wet-ball milling in such materials as ethanol (Bardaine et al., 2008). This separates the milling media from the charge, although the liquid has to be removed after milling (Moulson and Herbert, 1989).

2.6.2 Chemical synthesis

An alternative route of producing powders used by Banerjee and Bose (2004) was through a wet citrate nitrate chemical route. During sintering there was a reaction of the citric acid and nitrates that resulted in the decomposition of the nitrates. This released oxygen, which burnt the carbon in the citric acid causing an exothermic reaction. The

rise in temperature at the micro level resulted in a reduction of the particle sizes to 70-110nm. An alternative approach in particle size reduction using PZT sol was used by Bortolani *et al.* (2009). An electrospray deposition method was used to spray the sol through an electric field, whereby particles were repulsed and agglomeration was reduced. The jet of liquid was then calcined mid-air, and resultant particle sizes were 100-300nm.

Bulk materials are made from powders, and are generally formed using pressing techniques. Dry and isostatic pressing involves a high pressure compression of powder in a cavity, and hot pressing combines this with high temperatures. An alternative approach is using slip-casting, whereby the PZT powder is suspended in a high viscosity liquid that is poured into a porous mould. The liquid permeates through the mould and the dried powder is left on the mould wall. Following the formation of the bulk shape, the materials are sintered at 1200-1400˚C in order to develop the crystal structure and microstructure (Moulson and Herbert, 1989; Rahaman, 1995).

2.6.3 Sol-gel processing

The suspension of metal organic networks in a colloidal liquid is known as a sol-gel. The starting materials consist of a solution of metal alkoxides in a solvent alcohol which is stirred together. Upon heating the viscosity increases forming a polymeric network as the metal ions are joined together by surface forces (Rahaman, 1995). In an alternative sol-gel process chelating agents are used to create a stable rigid polymeric solution where metal ions are immobilised (Pechini, 1967). The chelating agents bond to the metal cations when mixed with a polyhydroxylic alcohol, and upon heating the chelate transforms into a polymer while the cations are homogeneously distributed throughout the solution (Zaghete et al., 1999; Abreu Jr. et al., 2005). A typical Pechini process has been developed by Qiu *et al.* (2009). The lead, zirconium and titanium constituents were mixed with ethylene glycol and citric acid, which are both chelating agents as electron pairs are donated to the metal ions. This resulted in the immobilization of the metal ions that were dispersed throughout the ethylene glycol, which also acted as the solvent. This was followed by heating at 140˚C to promote

polymerisation and reduce liquid content. The advantage of this process is that it gives a high control over stoichiometry of a complex system.

Sol-gels can be used with casting techniques in order to produce bulk materials. They can also be deposited onto substrates to form films. The deposition techniques generally used are spin coating, dip coating and spraying (Rahaman, 1995; Xie et al., 2006; Xie et al., 2006; He et al., 2003). These will be discussed in more detail in section 2.7. The advantage of using sol-gel is that the processed bodies contain small grains which exhibit high surface free energies and thus high sintering rates can be achieved. This has been shown by Dong *et al.* (2007) where annealing temperatures as low as 600˚C was used. However, a consequence of the high liquid content of sols there are high levels of film shrinkage that can result in cracking of the film and interfacial stresses with the substrate (Xie et al., 2006). Chen *et al.* (2003) found that the amount of cracking reduced when the rate of shrinkage was managed. This was achieved by increasing the viscosity of the deposited sol-gel, followed by low drying rates. As a consequence of these issues sol-gel film production is generally restricted to thicknesses below 1μm.

2.6.4 Composite production

One route in which thicker films can be processed is by combining PZT powder and sol-gel. This is because there are lower amounts of film shrinkage exhibited during the heating processes (Barrow et al., 1995). The powder and sol-gel are mixed together during ball milling for an extended period of time until the powder is homogenously distributed throughout the sol, this results in a viscous slurry (Wang et al., 2003). The increase in the achievable film thicknesses has been demonstrated by Dauchy *et al.* (2007a), whereby 42μm thick crack free PZT films integrated with a silicon substrate were processed; however, it was found that further increases in thickness resulted in cracking. Another advantage of using composites is that low sintering temperatures can be used, and thus the probability of cracking and damage at the film-substrate reduces. This has been demonstrated by Corker *et al.* (2002), as a sintering temperature of 710˚C was successfully applied. The low temperatures were also achieved due to higher sintering rates obtained through liquid phase sintering due to the melting of sintering

aids that were added during slurry production. Other routes that have resulted in the enhancement of composites include the reduction of the powder particle size. Bardaine *et al.* (2008) processed two sets of composite thick films; one with a powder that was crushed and had a mean particle size of 1µm, and the second was subjected to attrition milling in ethanol and had a mean particle size of 200nm. It was observed that the density of the film increased as the particle sizes decreased, which was a result of greater homogeneity of the particles throughout the slurry. An alternative approach to increase relative densities is by using sol infiltrations. This is done by depositing a layer of composite slurry onto a substrate which forms a thin porous film. This is followed by the deposition of compatible sol that seeps through the structure into the porous regions. Upon heating the sol crystallises at the porous regions and results in the porosity being effectively reduced (Xie et al., 2006; Kholkin et al., 2001). Dorey *et al.* (2002) used this technique and it was observed that the dielectric properties of the film were similar to that found with bulk materials. This suggests that this processing route is highly effective. Although, due to domain pinning issues the piezoelectric capabilities were lower than that found in bulk materials.

2.7 PZT film fabrication

Thin and thick PZT films are produced by depositing sol or slurry onto substrates. Generally silicon wafers are used for integration with electrical circuits and MicroElectroMechanical systems (MEMS). Therefore, commonly used deposition techniques that have been described in literature are discussed in the following section, including dip coating, spin coating and electrohydrodynamic atomisation (EHDA) (Rahaman, 1995; Dorey et al., 2002; Jeon et al., 2000; Kozuka and Takenaka, 2002; Muralt, 1997; Wang et al., 2008).

2.7.1 Dip coating

Dip coating is the process of submerging a substrate into a pool of liquid, whereby particles bond to both sides of the substrate due to surface tension forces. The first stage of dip coating is vertical immersion of the substrate into a pool of sol or slurry. The substrate stays submerged for a period of time. This is followed by vertical

removal of the substrate, where the surface tension and viscous drag of the liquid results in deposition of the liquid onto the substrate. As the substrate is removed excess liquid is removed as a consequence of gravitational forces and evaporation. The film is then subjected to heat treatment. Layers can be deposited at various thicknesses depending on the substrate removal velocity (Guillon et al., 2007). It is also possible to fabricate more complex multiple layers of slurry, along with sol infiltrations of a porous green body via dip coating (Bardaine et al., 2008).

2.7.2 Spin coating

Spin coating is the process of depositing a liquid onto a substrate followed by spinning at a high angular velocity in order to produce a uniform film. Spin coating is categorised into four stages; deposition, spin-up, spin-off and evaporation.
Firstly a liquid is deposited onto the centre of a stationary substrate. The substrate is then spun at high angular velocities, generally 1000-3000rpm for 30-60 seconds (Bardaine et al., 2008; Guillon et al., 2007). At the spin-up stage centrifugal forces result in the drive of the liquid radially outward. Following this, excess liquid flows to the perimeter of the substrate and evaporates in the spin-off stage. As the viscosity of the liquid increases the effect of the centrifugal forces decreases, this results in a decrease in spin-off rates. In the final stage of spin coating evaporation of excess liquid becomes prominent. This results in a reduction of the thickness of the deposited film. As a result of the equilibrium of the forces of the outward flow of the liquid due the rotating forces, and viscosity increases of the liquid, uniformity of the film increases. Evaporation also tends to occur uniformly across the film assuming the film distribution is initially uniform (Rahaman, 1995). Spin coating has been used to produce thin and thick films using sol-gel and composites, respectively. As discussed earlier, spin coating has also been used to deposit slurry, followed by sol infiltrations in the processing of highly dense thick films (Xie et al., 2006; Kholkin et al., 2001; Dorey et al., 2002).

2.7.3 Electrohydrodynamic atomisation

Electrohydrodynamic atomisation (EHDA) is the process of spraying a liquid through an electric field in order to obtain a uniform spray with low particle sizes. This process

has been used to spray PZT slurry by Wang *et al.* (2008). In process a low viscosity slurry is pumped through a nozzle directed downwards toward an aluminium plate. The nozzle and aluminium plate are connected to a high voltage power supply. The applied electric field between the nozzle and aluminium plate is at several kilovolts, which results in the atomisation of the pumped slurry (Jayasinghe and Edirisinghe, 2002). Depending on the strength of the field different spray modes can be obtained such as the dripping mode at a low voltage, cone-jet mode at a medium voltage and multi-jet mode at high voltages. The cone-jet mode is most useful and most used mode. It is the formation of an upside down cone with a spray meniscus forming at its tip. The jet of liquid is comprised of sub-micrometer particles if the Rayleigh limit of the liquid is exceeded. This is obtained when the electrostatic pressure of the jet approaches the capillary pressure of the liquid. The jet of liquid follows the electric field vectors causing an acceleration of the jet towards the ground electrode (Cloupeau and Prunet-Foch, 1994). The cone-jet mode was used by Wang *et al.* (2008), which was found at a voltages of 5-7.5kV, and resulted in a continuous stream of homogeneously distributed sub-micrometer particles. The substrate that the sprayed slurry was required to be deposited onto was placed on top of the aluminium plate. Furthermore, the aluminium plate was connected to a motorised stage so that the substrate could travel through the stationary spray, in order to coat the entire substrate.

In this project spin coating and EHDA has been used to fabricate PZT thick films. Spin coating was chosen because it is commonly used in research. Furthermore, the advantages over dip coating are increased film uniformity, and only one side of a substrate is coated during deposition. Additionally, sol infiltrations of slurry layers can be used. EHDA was chosen because the film thicknesses and uniformity are independent of liquid viscosity. Although, the viscosity of the liquid is required to be sufficiently low so that it can be pumped. Furthermore, uniform films can be obtained using EHDA as a consequence of low particle sizes in the spray.

2.8 Free sintering

Sintering is the irreversible process of lowering the free energy of a material (Rahaman, 1995). This occurs with the application of high temperatures and/or pressure. During sintering of PZT the microstructure develops as the relative density and grain size increases. Furthermore, a crystallographic change is also induced. There are two main types of sintering that are discussed. Firstly, free sintering, whereby a material is unconstrained from outside forces. Secondly, constrained sintering is where the sintered material is integrated with a material that exhibits differing sintering kinetics and thermal expansions, which may result in adverse sintering mechanisms exhibited. For discussions on constrained sintering the reader is directed to section 2.9.

2.8.1 Preparation prior to sintering

Prior to sintering pyrolysation is conducted at a mid temperature that results in the development of a porous microstructure as the excess organic matter is burnt off. The organic matter decomposes into water vapour and carbon dioxide gas, which when escaping results in pockets of porosity. A study by Qiu *et al.* (2009) produced bulk disks from powders that were heated at different temperatures to obtain decreasing organic residue. A 94% dense disk was produced after sintering when the organic residue of the starting powders was 2.4%; whereas a 98% dense disk was produced when the organic residue of the starting powders was 0.95%. Therefore, it is vital that all organic residues are burnt off during the pyrolysing stage in gain high densities.

2.8.2 Densifying sintering mechanisms

The driving force of sintering arises from the curvature of the particle surfaces (Rahaman, 1995). At curved surfaces there are high amounts of free energy. This lowers during sintering as the diffusion of matter occurs from regions of high surface free energy, which is also a region of low chemical potential, to a region of low surface free energy or high chemical potential. This is essentially matter flowing from regions of high density to low density, which also results in a reduction of the curvature of particle surfaces and a lowering of the free energy of the material.

There are six mechanisms of sintering that all lead to the growth of necks between particles, and thus results in the reduction of the curvature of particles. The first three mechanisms result in the densification of a material as porosity reduces; these are 1. Grain boundary diffusion, 2. Lattice diffusion and 3. Plastic flow (Fig. 8). The first two mechanisms are matter diffusion along a grain-grain intercept towards a pore that leads to a reduction in porosity and neck or grain growth. Plastic flow occurs through a dislocation motion from dense regions within a grain towards the neck. The rates of these mechanisms are greatest when grains are small and are surrounded by pores because there is a shorter distance for the matter to travel towards a pore.

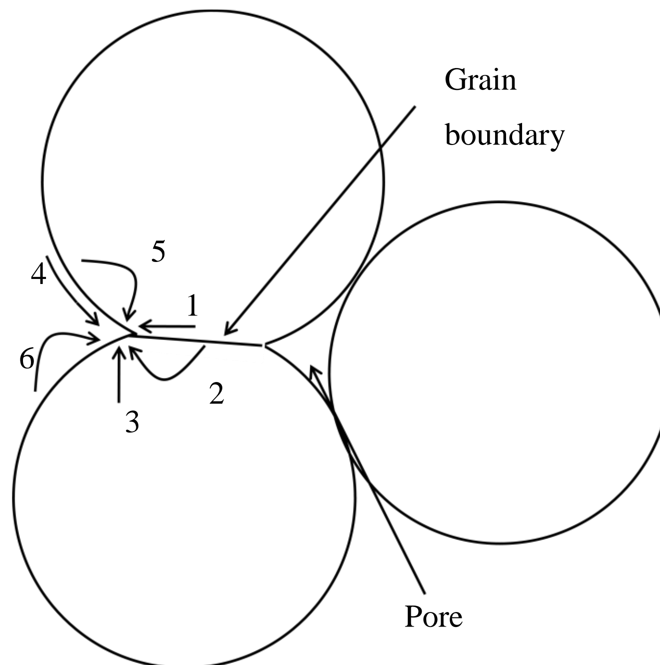

Fig. 8. Schematic of six differing sintering mechanisms at grain and pore intercepts in free sintering (Rahaman, 1995).

2.8.3 Non-densifying sintering mechanisms

There are also three non-densifying sintering mechanisms. These are 4. Surface diffusion, 5. Lattice diffusion and 6. Vapour transport (Fig. 8). This describes the matter flow from the convex to the concave surface of a grain, which results in grain growth and bond stiffening. However, as matter flows from a grain-pore intercept from one grain to a likewise grain-pore intercept of another grain there is no net decrease in porosity. Grain growth may also transpire through coalescence, which occurs as a

consequence of increases in the area of grain-grain boundaries, followed by the envelopment of smaller grains by larger grains. This can occur in solid state sintering as a consequence of the migration of the grain boundary through the smaller grain, until only one, larger grain exists. This mechanism occurs by a reduction in grain interfacial energies. Coalescence may also occur during liquid phase sintering as a result of the liquid phase partially penetrating a grain-grain boundary, and subsequently migration of the liquid phase boundary position in a similar fashion to grain boundary migration. However, this only occurs when there are large amounts of the liquid phase and when there is a low wetting dihedral angle. Additionally, solution precipitation results in coalescence through the gradual flow of matter through the liquid phase from a small grain bonded to a larger grain (Rahaman, 1995).

As grain growth occurs there is a decrease in densifying rates as the distance for densifying matter flow to travel increases (Rahaman, 1995). However, grain growth is necessary as domains exist within grains. Therefore in practice, a balance between densification and grain growth must be obtained. Gupta (1972) has studied this and found that for freely sintered ceramics that the sizes of grains and the relative densities increased linearly up to relative densities of 85-90%. Subsequently, at higher relative densities it was found that grain growth rates increased and densification rates decreased. Therefore, the resultant densities will be affected by these late sintering mechanisms, and tighter control over grain growth must be obtained. One route of doing this has been shown by Sangsubun *et al.* (2009), whereby the sintering temperature was increased from 900˚C to 1150˚C and it was found that there was an increase in the relative densities from 80% to 97%, but the grains did not significantly increase in size. However, at a temperature change of 1200˚C to 1300˚C, grains grew from 3μm in size to 13μm, and relative densities decreased. This work demonstrates that it is possible to obtain the required densities at a particular sintering temperature, followed by finishing the sintering process at a higher temperature to obtain greater grain sizes. However, in film processing the use of these high temperatures is not practical, but an alternative control of grain growth has been demonstrated by Chao *et al.* (2009) by adjusting sintering aid content. They found with the application of 0.10wt% of $LiSbO_3$ sintering aids, that densifying rates were promoted. However,

when more than 0.10wt% was used the grain sizes increased at the expense of densification rates. This occurred because excess sintering aid separated at the grain boundary causing transient liquid to bring the grains in closer contact resulting in an increase in grain growth rates.

2.8.4 Lead loss

The simplest way to increase sintering rates is to increase the sintering temperature. However, when sintering PZT ceramics the volatility of lead has to be considered, which has been reported to occur at temperatures over 850˚C (Van Werde et al., 2007). This leads to lead evaporation that results in decreases in densification rates, reductions in active piezoelectric material, increases in ion vacancies, and also results in unwanted film compositions (Banerjee and Bose, 2004).

There are a number of ways that the effect of lead volatility can be overcome. Firstly, the evaporated lead can be replaced. This has been achieved by sintering PZT ceramics in a lead rich atmosphere (Wu et al., 1998; Yang et al., 2010). However, the high toxicity of lead means that sintering has to be closely monitored. An alternative approach is to add excess lead to the system prior to sintering. However, the amount of lead that will be lost due to sintering has to be predicted, and has varied across literature. The amount of excess lead added by Corker *et al.* (2002) was 5mol% when sintering at 710˚C; whereas Wu *et al.* (2009) used 20mol% at 750˚C. The disparity between excess lead shows that it is difficult to accurately measure and replace evaporated lead.

2.8.5 Sintering aids

An alternative approach to reduce the volatility of lead is by reducing sintering temperatures. However, sintering rate reductions are not wanted, so sintering aids have been used. As a result a liquid phase is produced during sintering that provides a low resistant diffusion path at the grain boundaries for migrating matter during sintering, and consequently sintering rates increase so that temperatures can be lowered. Sintering aids have been used with composite materials, and are added during the ball-milling stage. The advantage of adding sintering aids at this stage is that they are

uniformly distributed throughout the slurry and hence the deposited film if there is uniform deposition. Sintering aids are activated with the application of heat, for instance the sintering aids PbO/Cu_2O used by Corker *et al.* (2002) melted at 680˚C. Upon melting these sintering aids formed a eutectic liquid that clung to the grain boundaries. Initially the liquid has a low viscosity and rapidly flows outwards forming a uniform grain boundary coating. The migrating particles then partially dissolve in the liquid with the smaller particles dissolving before the larger particles. Sintering matter flow is then rapid as a consequence of a low resistance path and a large capillary compressive force that is exerted on the dissolved particles. As sintering continues an increasing amount of particles dissolve in the liquid and as a result the viscosity of the liquid increases. Consequently, the rate of the matter flow decreases. As particle rearrangement slows, grain growth rates increase through the aforementioned solution precipitation and coalescence mechanisms (Rahaman, 1995).

In PZT thick films processed by Corker *et al.* (2002), it was estimated that the higher densities obtained by using sintering aids resulted in an increase in relative permittivity from 450 to 700. However, there have been some reported degrading effects with the use of sintering aids. One issue is that the solubility of TiO_2 is higher than that of ZrO_2 in a liquid phase formed from PbO. Therefore, the composition can shift towards the Ti-rich state, thus resulting in a lack of control over the final composition (Banerjee and Bose, 2004). Further degrading effects have been observed to occur with vigorous ball milling of sintering aids (Corker et al., 2002). This led to a shift of the PbO from the orthorhombic to the tetragonal phase, and thus the non-required crystal structure. Furthermore, care has to be taken in the amount of sintering aids added. It has been shown that with an increase in the amount of the sintering aid CuO, it can be incorporated into the crystal lattice (Tsai et al., 2009). This occurred because the Cu^{2+} ions replace the B site ions in the PZT unit cell resulting in a change in the phase from the tetragonal to the rhombohedral. However, Dorey *et al.* (2002) used up to 0.7wt% of CuO_2 without observing copper incorporated into the crystal structure. Therefore, there are issues surrounding sintering aid addition, but these have mostly been overcome in research.

2.9 Constrained sintering

For many applications ceramics must be integrated with substrates, in which sintering then becomes more complicated. This is because sintering in the x-y directions (Fig. 9) is restricted. The level of the restriction is dependent on the nature of the substrate. A non-rigid substrate may not result in total sintering constraint. However, the substrate will deform as the ceramic shrinks in the x-y directions, which may result in a body which would be difficult to integrate into an electrical circuit. One route which has been developed to reduce sintering constraints is to use a substrate of a similar density to that of the integrated ceramic. As a consequence the materials sinter at similar rates, resulting in mostly unrestricted sintering along with limited deformation of either material (Wright and Yeomans, 2008). However, one drawback is that a silicon substrate cannot be used in this method, which is a requisite in the production of MEMS. Silicon substrates that are integrated with PZT films is considered to be rigid because it is much greater in size in the z direction than the PZT film, and is thus considered to be non-deformable during the sintering process.

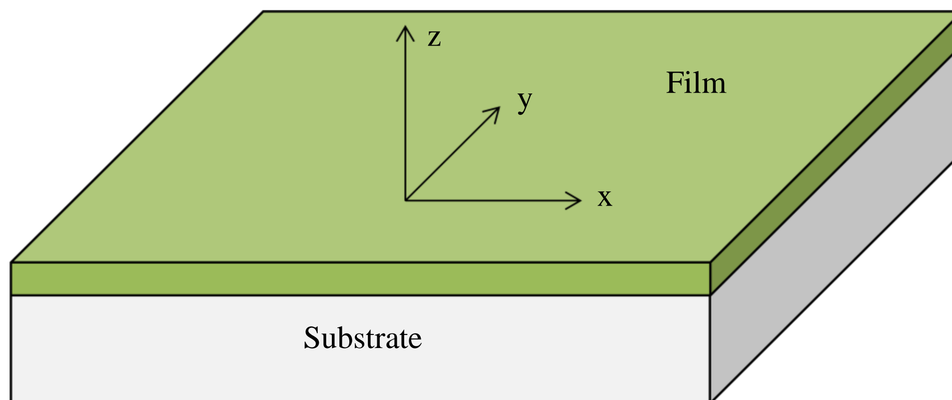

Fig. 9. Schematic of constrained sintering.

There are two main mechanisms that effect the sintering of constrained PZT films. Firstly, sintering of the film is fully restricted in the x-y directions as the rigidity of the substrate opposes the drive for sintering (Dorey and Whatmore, 2004b). This can result in the densities that are achievable through sintering being greatly reduced. However, sintering in the z direction is considered to be unrestricted (Cipitria et al., 2009). Secondly, as sintering takes place at high temperatures there is an added effect of the

thermal expansion of the materials. This can result in interfacial tension between the integrated materials as they expand at differing rates. These constrained sintering effects can have an extremely detrimental effect on PZT films. So these are more closely examined in the following sections.

2.9.1 Sintering restrictions

Garino and Bowen (1987) studied the effect of restricted sintering of ZnO films bonded to a rigid substrate and compared it to freely sintered ZnO films. Free sintering resulted in film shrinkage of 23%, compared to film shrinkage of 13% during of constrained sintering. However, in another study Cipitria *et al.* (2009) found that a consequence of the sintering restrictions in the x-y directions was an increase in the densification rates in the z direction. This was found by comparing the shrinkage of free and constrained YSZ coatings. The constrained coatings comparably shrunk more in the z direction as a consequence of grain boundary diffusion reversal that occurred perpendicular to the substrate. This resulted in smaller grains in the z direction compared to freely sintered coatings and thus greater shrinkage.

2.9.2 Origin of stress

Tensile stresses in the film are generated in the x-y directions as a consequence of film shrinkage and thermal expansion mismatches between the substrate and the film. This may first arise when the temperature of the integrated bodies is raised during drying and pyrolysing. This is a consequence of film shrinkage that occurs as liquid and organics are removed. However, stress is generally relieved due to matter rearrangement that is facilitated by residual liquid (Dorey and Whatmore, 2004b). Following this, sintering is conducted in a furnace, where a ramp rate is applied until the required temperature is reached. These ramp rates can be rapid, for instance Wang *et al.* (2008) produced crack free PZT thick films using a ramp rate of 60˚C/min. The coefficient of thermal expansion (CTE) of the pyrolysed PZT film, and the pyrochlore PZT film that develops at 450-500ºC, is lower than that of the thin film of platinum and well matched with the silicon substrate below a temperature of 500ºC (Corkovic et al., 2008; Garino and Harrington, 1992). Therefore, the substrate and electrodes expand at a greater rate than the PZT film, resulting in tensile stresses before sintering is initiated. As the

temperature increases there is a crystallographic change of the PZT to a perovskite structure, and at temperatures greater than 500ºC the CTE of PZT is greater than the silicon substrate. However, it has been shown by Corkovic *et al.* (2008) that this crystallographic change results in stress relaxations. This can occur due to a number of factors, including lattice matching at the interface as a consequence of an intermetallic Pt_3Pb phase if the platinum film and lead reacts, this results in a reduction in shear stress. It was also found that a much larger stress value occurred when perovskite crystallisation was incomplete. During sintering the film shrinks in all planes. However, the action of sintering in-plane with the substrate is restricted, thus the opposition of this action results in tensile stresses in the film. After sintering is complete cooling of the bodies then occurs, which can result in further stresses in the film. If the bonding does not fail during sintering or cooling, residual tensile stress develops in the x-y directions in the film. It has been stated that the generation of stresses predominantly occurs during the cooling stage (Hsueh et al., 2006). It has been shown by Cai *et al.* (1997) that residual tensile stresses can be reduced when there are gradual decreases in temperature in the cooling stage. Furthermore, it has been found that residual tensile stresses can be independent of film thickness (Corkovic et al., 2008). In this examination the film was built up one layer after another. As the first layer was deposited and subsequently crystallised, stresses were induced in the film. With the deposition of the next layer it crystallised upon the first layer, whereby there was no mismatch between these layers, and thus there was no further stress induced.

2.9.3 Stress relaxations

Increases in stresses that arise during constrained sintering can result in stress relaxations. These can be put into three main categories; creep, cracking and delamination. Coble creep occurs when atoms flow from an area of tensile stress that has low chemical potential to an area which has a higher chemical potential. This results in the reversal of the grain boundary diffusion and consequently the pores increase in size in-plane with the tensile stress. Nabarro-Herring creep is another form of creep, which occurs by lattice diffusion whereby matter transport occurs via a dislocation method (Rahaman, 1995). Examinations of the effect of creep on stress have been conducted by Dean *et al.* (2011). This was done by applying a tensile stress

on copper foil integrated with a titanium substrate, as creep occurred it was found that there were reductions in stress from 250MPa to 174MPa. This also resulted in reductions in the probability of cracking occurring. This however does not show the effect of creep during constrained sintering, which has been examined by Cipirtia *et al.* (2009) in real-time during heating. Initially tensile stress increased in the body with a lower CTE as a consequence of thermal expansion mismatches in the heating up stage. Subsequently, reductions in stress occurred due to coble creep and microcracks forming and as a consequence the restrictions on the drive for sintering reduced, resulting in an increase in sintering rates. Therefore, to reduce potential damage to constrained films and to increase the sintering rates creep may be a desirable mechanism.

When higher stresses occur in a body that is not relieved by creep, microcracking may occur. An extensive study into the occurrence of cracking in co-sintered Al_2O_3/ZrO_2 bilayers has been done by Cai *et al.* (1997). There were two types of cracks found that occurred in the body under biaxial tension. The more commonly found crack formed as a consequence of stress concentrated at a porous region during sintering, resulting in a neighbouring region to open up into a pore. This resulted in interlinking pores perpendicular to the direction that the tensile stress was in. Secondly, during cooling as a result of thermal expansion mismatches brittle uniform cracks with well defined edges occurred. These also formed perpendicular to the stress. The occurrences of these cracks were reduced by the use of a slow cooling rate. From this work it can be concluded that the thermal expansion mismatches during cooling are a challenging issue, but this has to be overcome in order to produce well sintered films that are under a constraint.

Finally, delamination is a relaxing mechanism that occurs when the interfacial shear stresses reach a threshold point. This does not often occur in constrained PZT films, Haigh *et al.* (2009) however found that delamination did occur when there was lead diffusion into the platinum bottom electrode during sintering. This resulted in a degradation of the PbO to Pb resulting in glassy regions of PtPb and Pt_3Pb. As a consequence there was swelling of the back electrode and partial delamination was seen. This was similar to that found by Corkovic *et al.* (2008), whereby the

intermetallic interfacial phase also resulted in stress relaxations. In further experiments this was prevented by depositing a barrier layer between the PZT film and the Pt bottom electrode.

2.9.4 Residual stress

Relaxations do not result in completely relieved stresses, thus there is residual stress. This can have an unwanted effect on domain orientations as domains tend to align parallel with a tensile stress as boundary strains are minimised. Therefore, in constrained films the tensile stresses that arise in the x-y directions result in domains orientated parallel to the substrate. It is noted that the induced domain orientations will not have an effect on the dielectric constant as it is reliant on the microstructural formation (Muralt, 1997). However, this will result in an increase in the piezoelectric coefficient d_{31} and a decrease in d_{33}. The direction of the domains can be re-orientated during poling, but there are some issues that affect the efficiency of this process. For instance it was found by Jones *et al.* (Jones et al., 2007), using high energy x-ray diffraction that surrounding a large induced crack in bulk, that PZT domains switched perpendicular to the direction of the crack. At a close proximity to the crack the orientations of the domains were non-reversible, but at greater distances from the crack re-orientation was possible. As cracks form perpendicular to tensile stresses and thus perpendicular to the substrate in constrained films, these findings suggest that domains close to a crack will be non-reversibly orientated in the x-y directions. This means that cracking can have an increased detrimental effect on the d_{33} coefficient.

Another effect that works against poling is the clamping nature of the substrate integrated with PZT films, which has been studied by Dorey *et al.* (2002; 2007). First it was confirmed using XRD analysis that the domains were orientated parallel to the substrate. Poling at a temperature of 135˚C was then conducted, and through XRD analysis it was shown that there was an increase in the number of domains orientated perpendicular to the substrate. However, some domains were still orientated in the x-y directions. This occurred because tensile stresses increased as domains re-orientated towards the z direction, and as a consequence when the poling field was removed these stresses were relieved as the domains reverted back to the original x-y orientation. By

maintaining the electric field during cooling the orientation of the domains was 'frozen' in the z direction more effectively. This work demonstrates that it is extremely difficult to obtain high d_{33} responses. However, there are different approaches to induce domain re-orientations, such as applying a compressive stress. This has the opposite effect of a tensile stress, thus inducing domains to orientate perpendicular to the substrate. Jones *et al.* (2008) found that with bulk PZT the application of a compressive stress perpendicular to the electrodes during poling resulted in non-180˚ domain switching. This contributed to a 40% increase in d_{33} compared to PZT that was poled without an applied stress. Similar effects have been found with the application of a compressive stress during the annealing of PZT films by Lee *et al.* (2007). As a consequence of the stress the film exhibited a larger remnant polarisation compared to films under a tensile stress because more domains were orientated perpendicular to the substrate.
More effective poling has been shown to enhance the piezoelectric effect of PZT films. However, the d_{33} of a PZT film can never be as great as that found in bulk materials. This is because the d_{33} increases due to the dynamic domain wall motion during the measurement stage, but this is restricted as a consequence of the clamping effect of an integrated substrate. The maximum d_{33} that can be achieved is described in equation 6, assuming that full clamping occurs in the x-y (1, 2) directions, and that the film is poled in the free z (3) direction.

$$(d_{33})_{meas} = d_{33} - 2d_{31}\frac{s_{13}^{E}}{(s_{11}^{E}+s_{12}^{E})} \qquad \text{Equation 6}$$

Where s^{E} is the elastic compliance of the material (Damjanovic, 1998).

2.10 Measurement of stress

Stress that develops during constrained sintering has been discussed to have a large effect on the final microstructure and dielectric and piezoelectric properties. Therefore, to examine and reduce these affects the stress of a film must be understood. There have been several methods developed to measure stress. First there is the Stoney approach (Stoney, 1909), whereby the bending of a beam relates to the amount of stress that the

beam is under (Stoney, 1909). Additionally, there are non-destructive methods that have been used to measure residual stress, such as X-ray diffraction and Raman spectroscopy.

2.10.1 The Stoney equation

Stoney discovered that there was a linear relationship between bending of metallic bilayers and the stress, σ, inducing it (Stoney, 1909). The Stoney equation has since been modified and used many times in research, shown in equation 7 (Corkovic et al., 2008; Láng and Seo, 2000; Ong et al., 2005a; Zhao et al., 1999).

$$\sigma = \left(\frac{E}{1-\upsilon}\right)\frac{t_s^2}{6_{tf}}\left(\frac{1}{R}-\frac{1}{R_0}\right)$$ Equation 7

Where E, υ, t_s, and t_f are the Young's modulus of the substrate, the Poisson's ratio of the substrate, the thickness of the substrate, and the thickness of the film. R_0 is the initial radius of curvature of the beam, which is zero if there is no stress exhibited. Finally, R is the final radius of curvature of the beam, which indicates a stress present.

This equation has been used many times in the examinations of the deflection of PZT films integrated with a substrate in order to examine the stress of PZT films (Corkovic et al., 2008; Ong et al., 2005a; Ong et al., 2005b). The advantage of using this technique is that the stress that develops during sintering and cooling can be continually monitored, so that the processes that results in stress generation can be identified. The disadvantage is that the measurements are an average and macroscopic in nature, meaning that regions of non-uniform stress are difficult to identify (Zhang and Zhao, 2006). Other issues have been found when identifying the stress of bending beams, as deflection only occurs along the longitudinal, so that stress across the width of the beam cannot be identified (Evans and Craig, 2006). However, it has been found the stress in the width direction is negligible when the aspect ratio of the beam was >4 (Sader, 2001).

There has been an extensive review of the Stoney equation used with PZT films by Corkovic *et al.* (2008). It was compared to the Townsend equation (Townsend et al.,

1987) which was a model that was derived to analyse the residual stress in multi-layered PZT films from curvature data, and so can be used to predict the stress in the silicon substrate, electrodes and multiple layers of deposited PZT. However, this model cannot always be used, for instance if the elastic properties of the film are unknown and if there are plastic deformations in the substrate. The Townsend equation was used as a benchmark because of a proven reliability in predicting the residual stresses of thick films. For films thicker than 2μm similar predictions of residual stresses were determined using both equations, but for films thinner than 2μm there was a disparity. It was concluded that the Stoney equation was overly sensitive to low film to substrate thickness ratios. Therefore, there are certain issues using the Stoney equation when accurate localised measurements are required. However, less information about the integrated material is required, and if an average, macroscopic stress measurement is required then this method can result in accurate measurements.

2.10.2 X-Ray diffraction

X-ray diffraction (XRD) is a non-destructive testing method that can be used to examine the lattice spacing and orientation of a crystal structure. The crystal lattice is affected by stresses. For instance a tensile stress parallel to the substrate will result in a stretching of the lattice and consequently the distance between parallel lattices reduces. The distances between the lattices can be examined using XRD, and subsequently the stress the film is under can be determined. This technique has been used by Ohno *et al.* (2008) for PTO films, whereby X-rays were focussed upon a certain Bragg peak. The sample was then tilted to various angles, with the Bragg peak re-measured. A shift in the peak position with respect to sample tilt indicated a residual stress. When graphed as peak position vs. sample tilt there was a linear relationship, where a negative slope related to a compressive stress and a positive slope related to a tensile stress (Ohno et al., 2008; Li et al., 2002; Zheng et al., 2004). The residual stress was determined using equation 8.

$$\partial(sin^2\Psi) = -\frac{\frac{E}{2(1+\upsilon)}.\cot\theta_0.\frac{\pi}{180}}{\sigma}.\partial(2\theta) \qquad \text{Equation 8}$$

Where Ψ is the sample tilt, E is the Young's modulus of the film, υ is Poisson's ratio of the film, θ_0 is the Bragg angle position of an unstressed sample, σ is stress and 2θ is Bragg angle position of a stressed sample. The elastic properties of the PTO films were well known. However, the elastic properties of composite PZT thick films are not well known. This is partially because the Young's modulus of the material changes with different compositions, heat treatment and microstructure development. This issue was also found by Li *et al.* (2002), as stress was determined using XRD at the (002) peak. It was found that the Young's modulus of the material was nonlinear as a consequence of domain switching.

A combination of the aforementioned stress analysis using the Stoney and XRD method was used by Yu *et al.* (2008) for PZT thin films. The tilted XRD method was used at the two different known points at a distance of x and –x from the centre of the substrate of an unstressed system, and thereby the initial curvature, R_0, of the substrate was determined. A PZT film was deposited and the same tilting XRD method was used again, thus the final curvature of the substrate, R, was determined. In this way the curvature of the substrate was accurately determined and the elastic properties of the film were not required.

2.10.3 Raman spectroscopy

Raman spectroscopy relies on inelastic scattering of monochromatic light with phonons in order to study the vibrational mode of a material via shifting in the received light. In the analysis of an unstressed material there is a characteristic peak in intensity at a given phonon frequency. When the material is then under a stress there is an increase in the phonon frequency peak position with a tensile stress and a decrease in phonon frequency peal position with a compressive stress. The shift in the peak positions can relate to the stress of the film. This method has been used by Ohno *et al.* (2008) to measure residual stresses of PTO thin films, using equation 9.

$$\omega(\sigma) = \omega(0) - \frac{\partial \omega}{\partial \sigma} . \sigma \qquad \text{Equation 9}$$

Where $\omega(\sigma)$ is the stressed phonon mode, $\omega(0)$ is the stress free phonon mode, $\partial\omega/\partial\sigma$ is a constant for PTO films at $89.0cm^{-1}$, and σ is residual stress.

This technique has been compared to the XRD technique by Ohno *et al.* (2008) and Rodrigues *et al.* (2010). It was found in both instances that identical stresses were measured. It was concluded by the authors that there were similar high levels of accuracy in the two methods.

2.11 Applications of piezoelectrics

The use of piezoelectric technology, in particularly PZT, is part of a large world-wide industry. Moreover, film technology is an ever increasing corner of the market. A few examples of the prominence of PZT in commercial products will be discussed.

Bulk PZT has been used commercially for decades in applications such as actuators, sensors and frequency controllers. More specifically in products such as gas igniters, transformers, bi-morphs, autofocusing in digital cameras, pressure sensors, ultrasonic transducers and acoustic emission sensors (Moulson and Herbert, 1989; Whatmore, 1999).

A gas igniter is presented, because it is an example of a PZT product which is widely used. A schematic of a gas igniter is displayed in Fig. 10, which works on the principal of creating a spark from a piezoelectric material that ignites a gas. Two bulk cylinders of piezoelectric material are adjacently positioned with a gap in the middle, called the spark gap. A swift force is applied to the outside end of both cylinders resulting in a deformation. As a consequence a potential difference between the outside to the inside end of the cylinders results in an electric field formed that travels through the material towards the spark gap. If the force is large enough the induced electric field will surpass the breakdown voltage threshold resulting in an electric spark. There is flammable gas at the spark gap area, which ignites with the introduction of the spark (Moulson and Herbert, 1989).

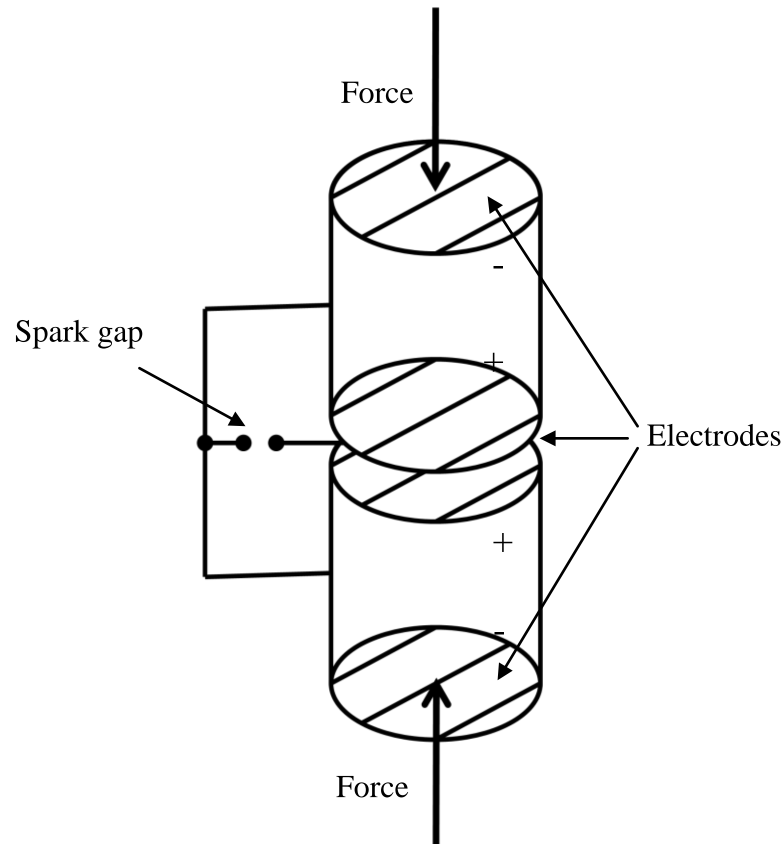

Fig. 10. Illustration of a piezoelectric material activated gas igniter.

Transducer applications are another prominent use of PZT. Specifically, ultrasonic transducers can be formed from bulk or thick film technology. These are used in various non-destructive testing techniques such as medical imaging. The basic principle is that a piezoelectric material is subjected to an a.c. voltage, as a consequence of the converse piezoelectric effect the material resonates and high frequency ultrasound pulses are produced. As these pulses hit the target they are reflected as an echo. This is then received by the piezoelectric material which also acts as the ultrasound sensor utilising the direct piezoelectric effect. The distance, shape and movement of the target can be interpreted from the velocity, wavelength and wave shape of the received echo. A schematic of an ultrasonic transducer is displayed in Fig. 11. It is manufactured by layering a dense material, followed by piezoelectric element, then a matching layer and finally a protective layer. The transmitted ultrasound waves are focussed in the required direction by the dense material. The PZT film is attached to electrodes connected to a processing computer chip. The acoustic index of the transmitted ultrasound waves are required to be matched to that of the medium in order to optimise energy conversion,

therefore a matching layer is needed which will have a varying acoustic index depending on the medium targeted. Finally a protective layer is required to protect users from the toxic PZT and to reduce potential environmental damage to the transducer.

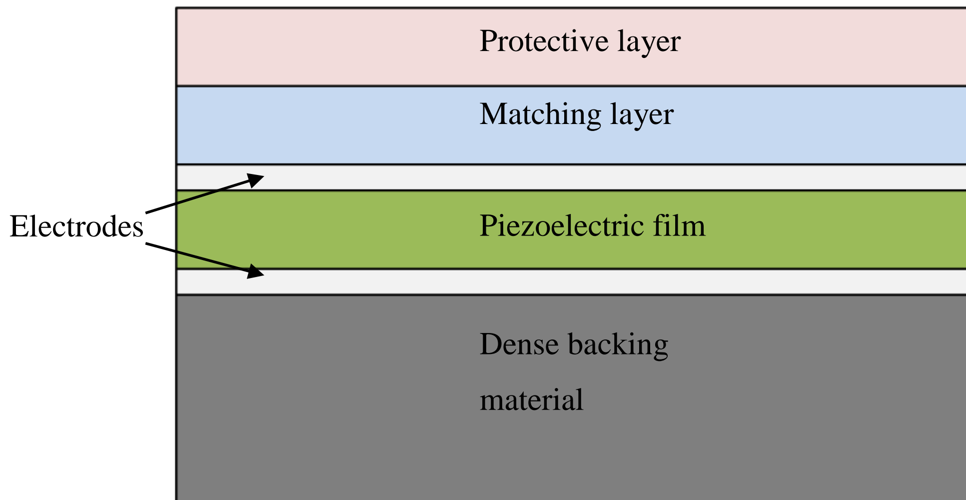

Fig. 11. Schematic of an ultrasonic transducer activated by a piezoelectric material.

In medical applications PZT is widely used as the active material in conventional ultrasound transducers in the frequency range of 30-60MHz (Moulson and Herbert, 1989). In recent research PZT thick films have been successfully used in ultrasound transducer applications by using the thickness mode of excitation to obtain the required resonant frequency. In order to obtain a transmitted 50MHz signal a film thickness of 35µm is required. Such thicknesses have previously been challenging to obtain using film technology, however, Dauchy *et al.* (2007; 2007b) produced a series of papers demonstrating fabrication of up to 42µm crack free thick films using composite technology. Ultrasonic transducers were fabricated and successfully used in the thickness mode to transmit high frequency ultrasound pulses.

The following discussions focus upon the use of PZT films in industry, particularly the integration with MEMS. The use of MEMS is ever increasing due to the increasing need for miniaturisation in computer chip based products and the reduction in cost of micro-silicon based products. PZT is used prominently in actuating roles in MEMS used in such applications as inkjet printing to create a pressure to accurately deposit ink,

acoustic emission sensors and wireless energy harvesting. A commercially successful application of PZT in MEMS is the use in accelerometers which are used to measure forces. These are widely used in airbag deployment systems for automobiles as they are cheaper, more accurate and smaller than previous accelerometer designs. A schematic of such an accelerometer is displayed in Fig. 12. There is a cantilever bi-morph displayed made up of a silicon substrate with an integrated PZT film and electrodes, and a known weight. When the automobile decelerates the block of weight also decelerates, so the cantilever bends forwards. This results in an induced stress upon the integrated PZT film and hence an electric field develops. This information is then sent to an attached computer chip. The voltage is compared to known voltage-deceleration data to determine the deceleration of the vehicle. When a pre-determined threshold point is reached the airbag will be deployed. Piezoelectric MEMS accelerometers are also used in the application of the rotation of the screen in smart phones, and machinery to monitor movement or rotation of moving parts.

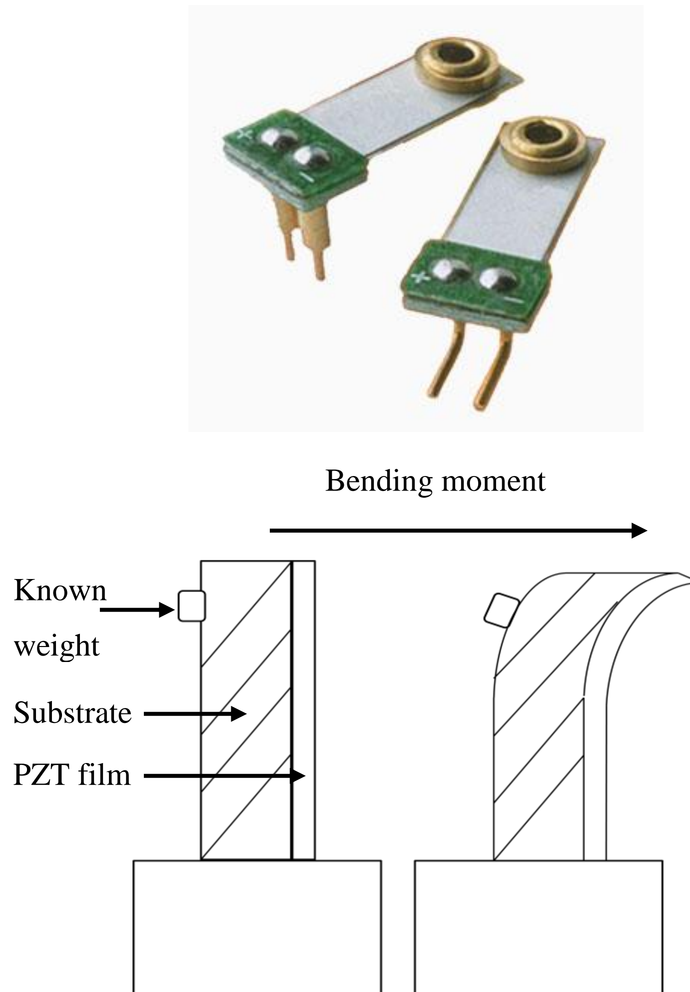

Fig. 12. A commercial cantilever bi-morph accelerometer (www.metrolog.net), and an illustration of an accelerometer used an airbag systems when decelerating.

Another use of Piezoelectric MEMS is in energy harvesting applications, where the direct piezoelectric effect and the ambient motion or vibrations results in wireless, free continuous energy. These are increasingly important in the modern world as the energy needs in mobile devices has outgrown the battery industry. One such application is in tyre pressure monitoring systems in automobiles. Currently it is common for these to be powered by batteries, but the labour costs in replacing these vastly outweigh the price of the battery. Therefore, there is a shift towards using energy harvesting MEMS for this application. Energy is harvested through the angular momentum and the heat generated during the motion of a tyre, using the direct piezoelectric and pyroelectric effect. This energy is then fed into the tyre pressure system. Energy harvested from mechanical vibrations has been successfully manufactured by Jeon *et al.* (2005) by using a

cantilever design. The schematic of this is displayed in Fig. 13. The vibration of the cantilever resulted in the PZT film being under alternating compressive and tensile stresses. This resulted in the generation of an a.c. voltage using the d_{33} and d_{31} coefficients of the film. To harvest the produced energy a rectifying circuit and capacitor to store the charge were integrated with the film. A continuous electrical power of 1µW was produced at 2.4V and a 5.2MΩ resistive load. The output power of these technologies are currently low, however, there are many low power applications needed, and current research is looking to improve efficiency of these devices.

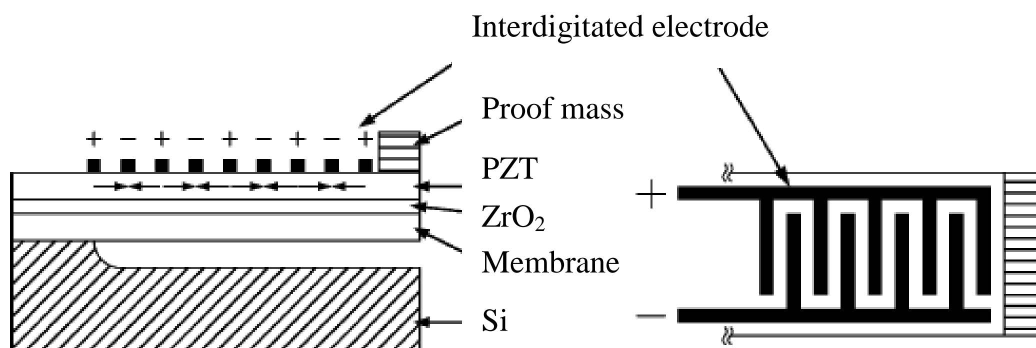

Fig. 13. Schematic of energy harvester in the d_{33} mode (Jeon et al., 2005).

MicroStrain, Inc. (www.microstrain.com) has produced powered health monitoring and operational load sensors used in rotating components in military helicopters powered by energy harvesting MEMS. A PZT element which was integrated with a sensor, conditioner, processor, data storage, and data transmission components was placed at the pitch link which connects the rotary blade to the main body of the helicopter. In order to power the sensor 0.98 milliwatts at a frequency of 4.3Hz was required. The energy harvested from the PZT element ranged 1.0-5.5 milliwatts depending on the strain of the rotary blade. Therefore a concise, perpetually powered device was manufactured using piezoelectric MEMS technology.

The wide use of silicon computer chips and the need for miniaturisation requires integration of sensors, actuators and transducers. For these applications piezoelectric MEMS are highly desirable because of high electromechanical coupling factors,

flexibility in device sizes and low costs. Therefore the drive for improvements in PZT thick films is an important area of research so that this technology can continue to compete in the market share.

Chapter 3

Methodology

3.1 Introduction

In this chapter a detailed description of the experimental procedures used during this project is presented. The aim was to fabricate PZT thick films integrated with silicon substrates followed by characterisation of the material. The first part of this chapter details the initial chemical processes used to create PZT sol and slurry. This is followed by descriptions of the methods used for deposition of the PZT slurry onto silicon substrates to form PZT thick films, along with electrode depositions. After deposition the PZT thick films were sintered to high temperatures. Finally, the characterisation of the processed PZT thick films is explained.

3.2 PZT fabrication processes

3.2.1 PZT sol

The PZT sol processing was conducted in a clean room environment under a fume hood. There were two different PZT sol processing routes used, so that different PZT thick film systems could be compared. The first process was based on using an ethylene glycol solvent; this was known as the PZT EG sol [$Pb_{1.1}Zr_{0.52}Ti_{0.48}O_3$]. This process was similar to that used by Pechini (1967) and Qiu *et al.* (2009). All mixing of chemicals was conducted under refluxing conditions, where heating and stirring was applied simultaneously. A condensing column was used to reclaim evaporated liquid, therefore conserving all constituent parts of the PZT sol. The PZT sol was produced from two separate solutions. In the first solution 3.763g of zirconium (IV) oxynitrate hydrate was mixed with 30.2ml of distilled water, and held at 60˚C for 30 minutes until dissolution was complete. In a separate solution 60.134g of citric acid was mixed with 69.8ml of ethylene glycol and held at 60˚C for 30 minutes. This was then followed by the addition of 5.113g of titanium (IV) butoxide which was highly moisture sensitive and hence kept in a nitrogen atmosphere. Upon addition a precipitate formed which dissolved within 1 hour. Both solutions were then cooled and mixed together. Finally 10.918g of lead (II) nitrate salts were added to the mixed solution and held at 60˚C for 30 minutes. Once all reagents dissolved a colourless clear solution was formed. This was then heated for 1 hour at 110˚C to promote polymerisation, which was indicated by

a colour change to a clear deep yellow. A final concentration of 0.31M of 100ml solution was achieved.

The second PZT sol produced was based on 2–methoxyethanol as the solvent; this was known as the PZT 2-ME sol $Pb_{1.1}$ $[Zr_{0.481}Ti_{0.472}Nb_{0.015}Sb_{0.015}Mn_{0.015}]$ O_3 (Corker et al., 2002; Dorey et al., 2002). All chemicals were mixed under refluxing conditions. Furthermore, the sol preparation process was highly moisture sensitive so refluxing conditions were conducted under a nitrogen atmosphere. Two separate solutions were produced; the lead acetate solution and the 2-methoxyethanol solution. The lead acetate solution was prepared by mixing 52.5g of lead (II) acetate trihydrate with 30ml of glacial acetic acid. This was refluxed for 3 hours, followed by complete dehydration of the solution using vacuum distillation at 102-104˚C until 20ml of distillate was gathered. The 2-methoxyethanol solution was prepared by mixing 17.685g, 27.328g, 0.629g, 0.508g, 0.342g and 50ml of titanium (IV) isopropoxide, zirconium (IV) propoxide, niobium (V) ethoxide, antimony (III) ethoxide, manganese (III) acetate and the solvent 2–methoxyethanol anhydrous, respectively. This was refluxed for 3 hours. Following refluxing, the two solutions were mixed together with further refluxing. The solution at this stage had a cloudy appearance. Vacuum distillation was then conducted at 84-90˚C to remove excess water until a clear yellow solution was obtained. The amount of distillate removed was replaced by additional 2–methoxyethanol to obtain a sol concentration of 1.1M, this was followed by the addition of 5g of ethylene glycol to stabilise the sol.

3.2.2 PZT slurry

PZT thick films were manufactured using PZT slurrys that were a mixture of the aforementioned PZT sols and hard doped PZT powder (PZ26, Ferroperm, Denmark) with a mean particle size of 0.6µm. Firstly, 14.2ml of the PZT sol was mixed with the addition of 10g of PZT powder. This was followed by the addition of 4.7wt. % sintering aids, which was 0.069g and 0.428g of Cu_2O and PbO, respectively. Finally 0.2g of KR55 dispersant (Ken-React Lica 38 , KenRich) was added to stabilize the slurry. Additionally, 100g of inert zirconia ball milling media were added; the mixture was then ball-milled for 24 hours to fully mix all constituents, and for a further 3 hours

before the slurry was used. These PZT slurrys were known as the EGS, and 2-ME slurry. Another PZT slurry was manufactured using the EG sol with no sintering aids added, this was known as the NS slurry.

3.3 Film deposition procedures

Prior to PZT deposition, 8nm of titanium followed by 100nm of platinum was deposited onto silicon substrates via sputtering (Nordiko Ltd sputtering system) to form bottom electrodes. Following this, PZT slurry was deposited onto the Ti/Pt silicon wafer. Two deposition techniques were used.

3.3.1 Electrohydrodynamic Atomisation

Electrohydrodynamic Atomisation (EHDA) was used to deposit EGS and NS slurrys, the schematic of this procedure is displayed in Fig. 14. The slurry was held in a syringe and all air bubbles were removed. The syringe was placed in a mechanical syringe pump (KD Scientific Inc., MA, USA) so that there was control over the flow rate of the pumped slurry. The syringe was connected via a silicone rubber tube to a nozzle. The nozzle was fabricated from a 0.85mm diameter needle suspended in an epoxy resin. This was held in position 10mm directly above the target. A high voltage power supply (Glassman High Voltage Inc., NJ, USA) was connected to the needle top electrode and the aluminium plate bottom electrode, onto which the silicon wafer was placed. The pumped slurry was atomised into a fine particulate spray by the electric field. The cone-jet mode was required to create a uniform depositions, which was found when a voltage of 5.5-6.5kV was used. The stability of the cone-jet was continually monitored using a USB digital microscope. The slurry was deposited over the entire substrate by passing the substrate through the spray in parallel runs in the x-y directions, controlled using a computer controlled motorised stage (Standa 8MT175-100-400mA). There were several variables that were adjusted to obtain varying thicknesses and film uniformity. These were slurry flow rate, voltage of applied electric field, speed of the movement stage, and the separation between each parallel spray. In order to obtain uniform films, these effects of these variables were investigated.

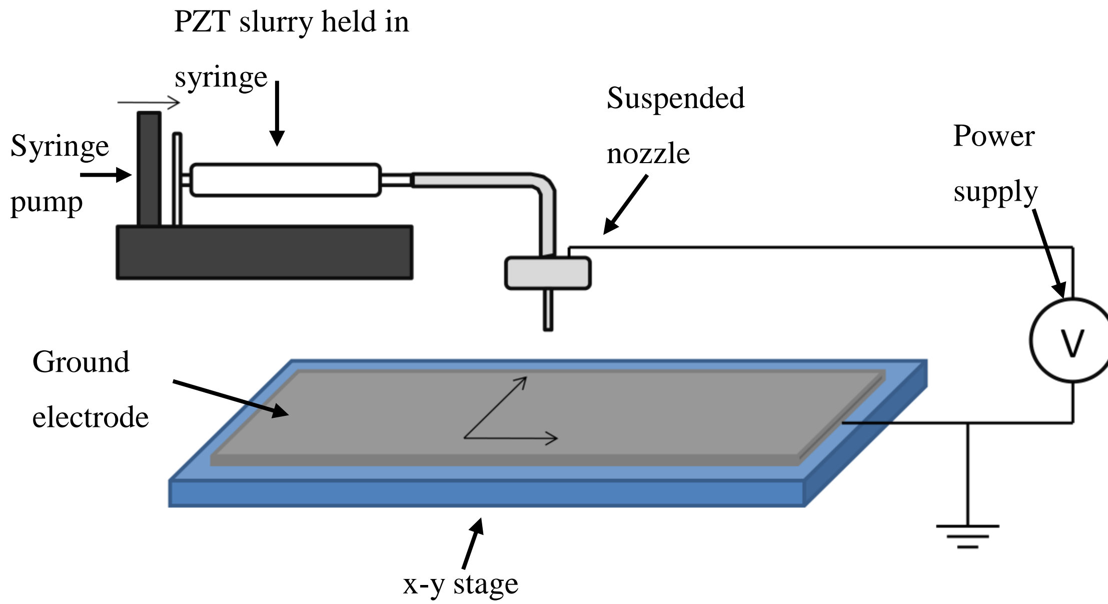

Fig. 14. Schematic of the EHDA deposition process.

Firstly, the flow rate and stage speed variants were examined by depositing single lines of EGS slurry onto glass slides. The flow rates used were 0.01, 0.02, 0.03 or 0.05ml/h; the stage speeds used were 5.0, 4.0, 3.5, 2.5 or 2.0mm/s. The lines of deposited slurry were dried at 150˚C, and pyrolysed at 350˚C on a hot plate. The profiles of the deposits were then measured using a surface profiler (Veeco Instruments Incorporation, UK), which was scanned across the deposit, with a z accuracy of 10nm. A profile of a line of deposit is displayed in Fig. 15, and it can be seen that a Gaussian distribution profile was exhibited.

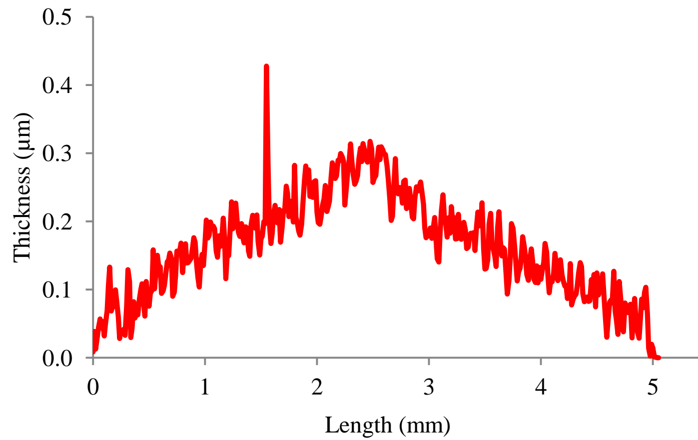

Fig. 15. The measured surface profile of a pyrolysed single line of deposited EGS slurry, at a flow rate of 0.01ml/h and a stage speed of 5.0mm/s.

Multiple parallel single lines of EGS slurry were then deposited onto glass slides using separations of 2.0, 2.5, 3.0, 4.0 or 5.0mm. The deposited slurry was dried, pyrolysed, and the profiles measured. The optimum profiles were defined by two quality factors (equation 10 and 11). Though using this the surface flatness and wall shape was quantified.

$$Quality\ factor\ 1 = \frac{Full\ Width\ Half\ Maximum}{H_d}$$

Equation 10

$$Quality\ factor\ 2 = greatest\ thickness - \ lowest\ thickness$$

Equation 11

Quality factor 1 was established by measuring the thickness of the deposited film at the full width half maximum and at the greatest thickness measured, H_d. The optimum shape of the films, which was a flat cubic structure, was determined when quality factor 1 tended to infinity. The flatness of the slurry deposits increased when Quality factor 2 tended to zero. The quality factors as a function of stage separation are displayed in Fig. 16. It can be seen that the best combination of quality factors were found when the separation between single lines of deposit was 2mm.

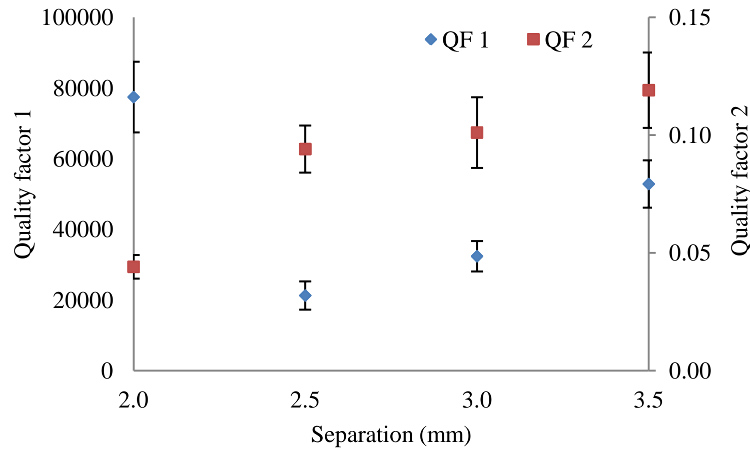

Fig. 16. Quality factors as a function of stage separation, at a flow rate of 0.01ml/h and a stage speed of 5.0mm/s.

The optimum film shape was found when a flow rate, stage speed and separation of 0.01ml/h, 5.0mm/s and 2.0mm were used, respectively. Furthermore, an electric field voltage and nozzle to electrode separation of 5.5-6.5kV and 10mm was used, respectively. During thick film depositions, parallel lines of deposited slurry in the x direction followed by deposition in the y direction were considered to be one layer. After each layer the film was dried at 150˚C followed by pyrolysation at 350˚C. One layer was found to be 0.6µm thick. In this project 8 layers were always used, which produced a 5µm thick film.

3.3.2 Spin coating

The 2-ME slurry was deposited on Ti/Pt coated silicon wafers using spin coating (Cookson electronics equipment SCS G3-8 spin coater); this process is displayed in Fig. 17. The wafer was held in place on a chuck using a vacuum. When stationary, the 2-ME slurry was deposited using a syringe onto the centre of the wafer. The wafer was then spun at 3000 rpm for 30 seconds. The film was dried at 200˚C for 60 seconds, and then pyrolysed at 450˚C for 30 seconds. After a slurry layer was deposited, the porous regions were infiltrated using 2-ME sol. This was conducted by placing the wafer back onto the spin coater and covering the pyrolysed layer with 2-ME sol. This was then spun at 3000 rpm for 30 seconds. After each sol infiltration the same drying and pyrolysing conditions were applied. For each slurry layer, four sol infiltrations were

deposited. This process was conducted three times in total, which produced a dense 5μm thick PZT film.

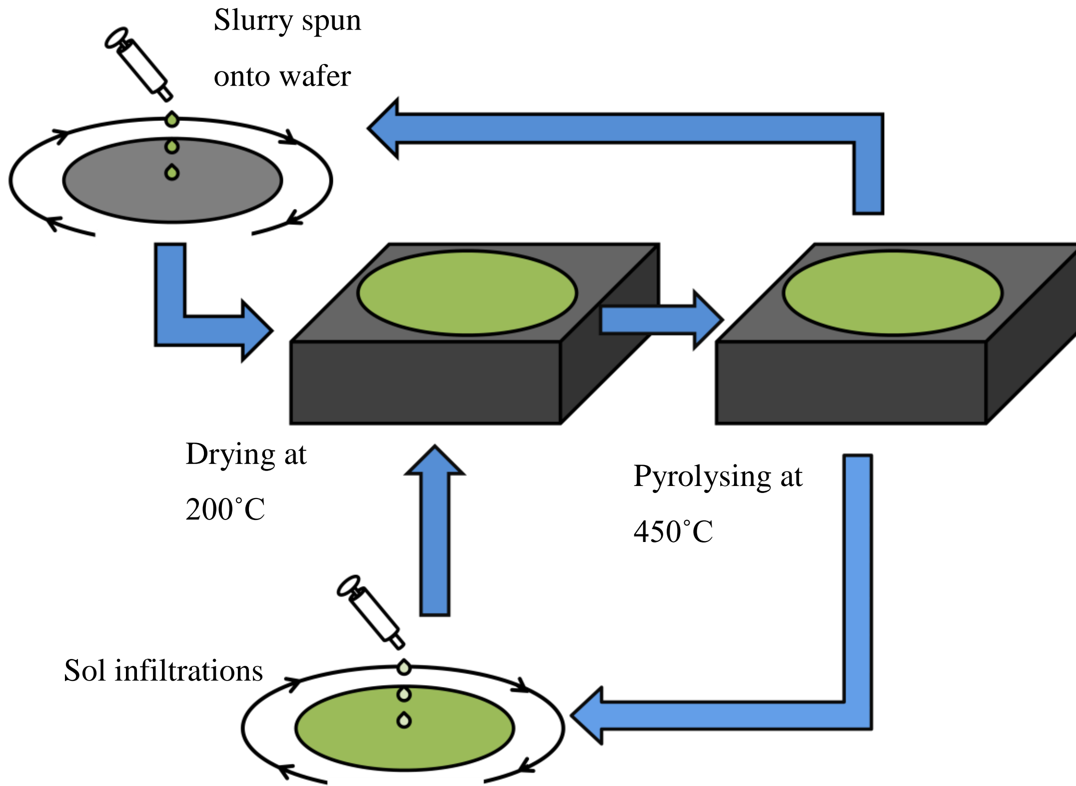

Fig. 17. The schematic of PZT thick film deposition using the spin coating process.

3.4 PZT island fabrication

Stand alone 5mm x 5mm areas of 5μm thick PZT films were produced on silicon substrates using the EGS slurry and EHDA. These were known as PZT islands, and have been analysed in Chapter 4. A schematic of this process is displayed in Fig. 18. PZT island shapes were produced by first depositing photoresist (AZ9260, Chestech UK) moulds on a silicon substrate. One layer of photoresist was deposited onto a silicon wafer by spin coating (EMS spin coater) at 4000rpm for 60 seconds (Fig. 18 A). The photoresist mould was then dried at 90˚C for 8 minutes. An acetate sheet mask was then placed on the mould which exhibited a pattern of selected areas of 5mm x 5mm at a distance of 10mm centre to centre (Fig. 18 B). The exposed regions were then subjected to UV light using a mask aligner (Karl Suss MA56) at an intensity of 6000Wm^{-2} for 90 seconds (Fig. 18 C). These regions of the coating were then removed

when bathed in 1:4 developer (AZ351B) and distilled water for 5 minutes (Fig. 18 D). This was followed by cleaning with distilled water and drying for 8 minutes at 90˚C. This process produced a 6-7μm thick photoresist film with mould cavities of 5mm x 5mm.

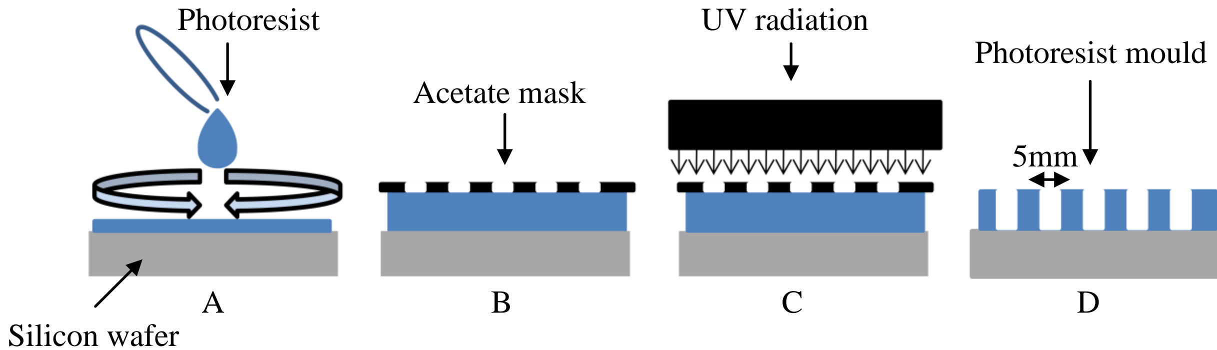

Fig. 18. Schematic of the photoresist mould processing procedure.

The EGS slurry was then deposited over the photoresist mould using the normal EHDA deposition process. After deposition of each layer of slurry, the excess slurry that built up on top of the photoresist mould was removed using a cotton bud. The slurry was dried at 125˚C for 5 minutes between each layer. After slurry deposition was complete, the film was finally dried at 165˚C for 10 minutes. These temperatures were carefully chosen in order to fully dry the PZT film without damaging the photoresist film. The film was then submerged in an acetone bath so that the photoresist film could be removed. The PZT islands were dried again at 165˚C for 2 minutes and finally pyrolysed at 350˚C for 2 minutes. The surface profiles of the PZT islands were then measured at multiple points in the x and y directions using a surface profiler to obtain representative dimension prior to sintering. This was followed by sintering each PZT island at a temperature of 725˚C for varying times between 0-60 minutes. The surface profiles of the PZT islands were then re-measured in order to compare pre and post-sintered profiles.

3.5 Sintering

3.5.1 Halogen bulb spot temperature

Normally sintering of PZT thick films is conducted in a furnace. However, for this project a different sintering technique was used which resulted in rapid heating and cooling rates so that the microstructural evolution during sintering could be essentially 'frozen'. This was conducted by using a focused halogen bulb (OSRAM halogen optic lamp) that resulted in a spot of localised high temperatures. The focal distance of the light from the halogen bulb on the sintering target was found at a distance of 16mm. This distance was kept constant throughout all experiments. The diameter of the focal spot was measured at approximately 5mm. The temperature of the spot was adjusted by varying the current supplied to the halogen bulb. The temperature was determined as a function of the applied current. This relationship was found by producing a thermal resistor by sputtering a strip of 15nm thick platinum onto a silicon substrate. Each end of the platinum strip was connected to a Wayne Kerr precision component analyser 6425 at 1kHz, in order to measure resistance. Firstly, the relationship between a known temperature and the resultant resistance was found by heating the substrate on a hot plate at known temperatures. This experiment was conducted 3 times to gather averages. The halogen bulb spot was then focused on the back of the silicon substrate at the location of the Pt resistor. The applied current was gradually increased while measuring the resistance of the Pt element. The experiment was conducted 3 times. This resulted in a relationship between known temperatures and the current of the bulb, which is displayed in Fig. 19. In this thesis a constant current of 9.4A was applied, which related to a temperature of 725˚C. This temperature was reached in less than 10 seconds from the point at which a current was applied to the bulb, thus exhibiting a rapid ramp rate.

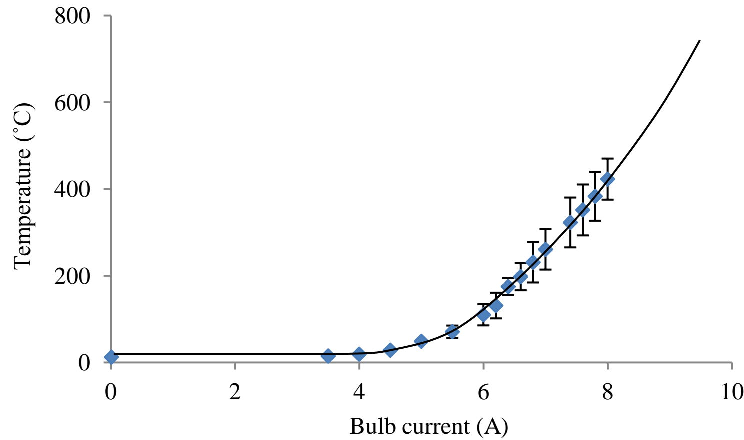

Fig. 19. Variations in the temperature of the sintering spot as a function of the applied current.

3.5.2 Spot sintering

There were two processes used to sinter PZT thick films. The first process was known as spot sintering, and was used to sinter the PZT films which have been analysed in Chapters 4, 5, and 7. The PZT film was held in a stationary position suspended at each corners by alumina crucibles. The halogen bulb was also fixed in position 16mm above the PZT film and the spot was directed to a specific area of the PZT film. In this process only the region which was directly exposed to the sintering spot was sintered. Other regions were subsequently sintered by turning off the halogen bulb, moving the sample, and illuminating the new area with the bulb. The sintering temperature was kept constant throughout all experiments with a ramp rate of less than 10 seconds, but the times of exposure were varied from 0-60 minutes.

3.5.3 Rastering sintering

A second process was used to sinter larger areas of PZT thick films, which is discussed in Chapter 6. This was conducted by holding the halogen bulb in position 16mm above the PZT film target. The PZT film was suspended at each corner using an alumina crucible, which was placed upon a motorised stage. The PZT film was passed through the stationary sintering spot in a rastering pattern. There were two experiments conducted. Firstly, PZT films were cut into 4mm by 45mm beams and were sintered in a single line scan through the sintering spot. The stage speeds were varied from 0.01mm/s to 0.50mm/s. The second process was conducted on PZT films cut into

40mm by 40mm areas. Multiple parallel line scans were employed to sinter the entire area. Stage speeds of 0.10mm/s were used, with the separations between each run of 1 to 7mm.

Following sintering of an area, top electrodes were deposited by evaporating (Edwards coater) 2mm and 1mm diameter circular electrodes of 15nm thick chrome followed by 50nm thick gold.

3.6 Property-stress relationship

The effects of an induced stress on PZT thick film properties were examined in Chapter 7. The PZT films were manufactured using the 2-ME slurry deposited using spin coating. These were then mechanically cut into beams of 4mm by 50mm. The central region in the length direction was sintered at 725˚C for times from 0 to 60 minutes and an electrode was deposited at this region. A stress was applied to the beam by applying a bending moment using a custom built four point bend rig, the schematic is displayed in Fig. 20. Two rods were positioned on the underside of the substrate and two rods were positioned on top of the PZT film. With the application of a compressive force to the two sets of rollers produced a uniformly distributed compressive stress across the centre of the PZT film between the top two rollers. Dielectric properties were measured at different stress levels. The PZT film was poled while under a stress at room temperature. This was followed by removal of the stress and then the d_{33} of the films were measured.

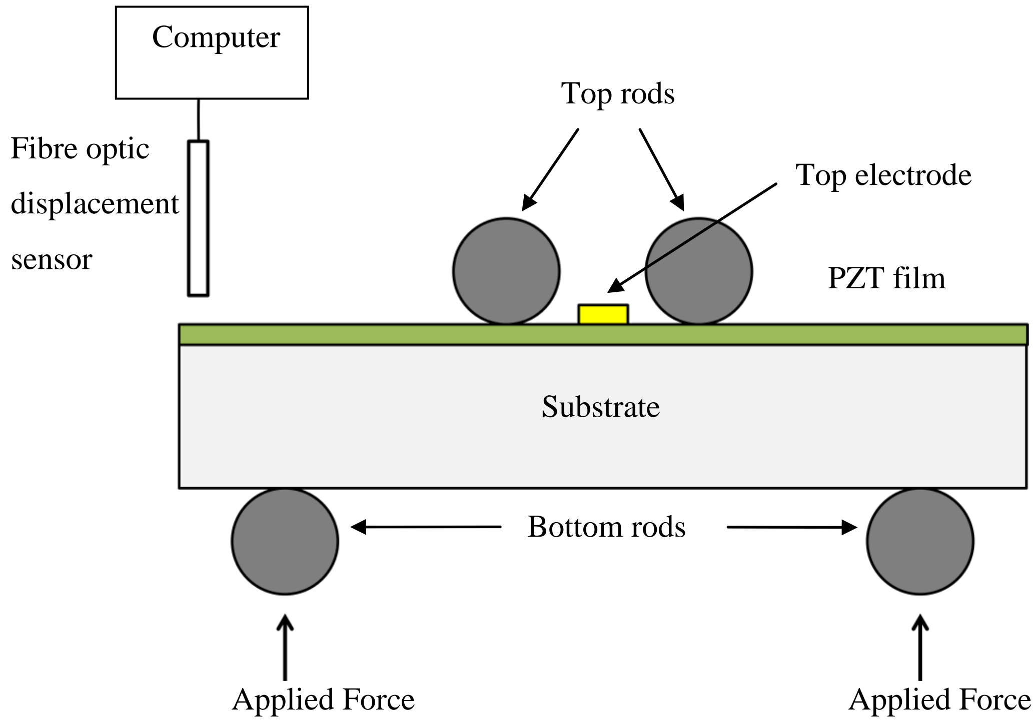

Fig. 20. Schematic of the four point bend rig with a stress applied on the beam.

In order to determine the magnitude of the stress applied, firstly the radius of curvature, R, of the beam was calculated using equation 12.

$$R = \frac{\delta_x}{2} + \left(\frac{z}{2}\right)^2 \left(\frac{1}{2\delta_x}\right) \qquad \text{Equation 12}$$

Where, δ_x is the measured displacement of the beam. This was measured using a fibre optic displacement sensor (Philtec muDMS RC 748) at the edge of the beam. Also, z is the distance between the edges of the beam. A schematic of the bending of the beam is shown in Fig. 21. The radius of curvature was then used in the Stoney's equation (Equation 7) to calculate the magnitude of the compressive stress.

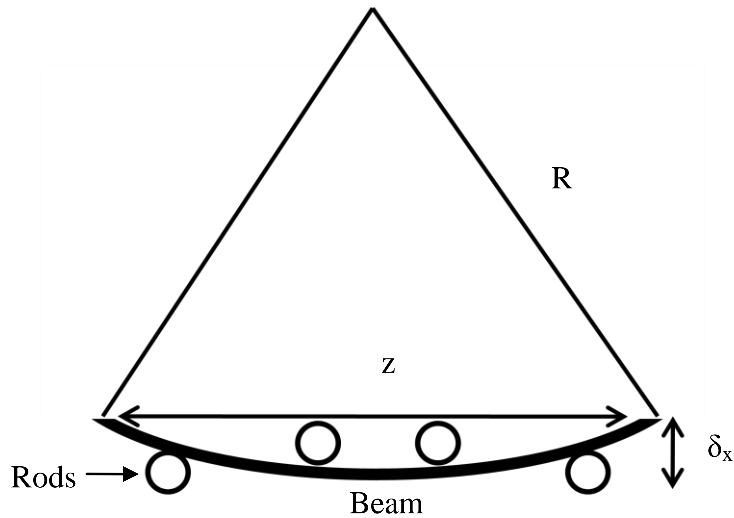

Fig. 21. Schematic of a stressed beam with mathematical notations.

3.7 Electrical properties characterisation

3.7.1 Dielectric testing

Measurements of capacitance, resistance and dielectric loss were measured using a Wayne Kerr precision component analyser 6425 at 1kHz. Measurements were taken 4 times per electrode to obtain an average. The relative permittivity was calculated from capacitance, thickness of the film and the radius of the electrode.

3.7.2 Poling and d_{33} measurements

Prior to piezoelectric measurements, the PZT films were contact poled. This was done by connecting the top and bottom electrodes to a DC voltage power supply while the film was held at a temperature of 135˚C. The voltage was gradually increased to 8V/µm, which related to 40V for the 5µm thick films. This was maintained for 10 minutes, followed by a temperature reduction to 70˚C and then the electric field was removed. The d_{33} coefficient of the film was measured using the Berlincourt Piezometer (Takecontrol Piezometer system PM 25).

3.8 Microstructural characterisation

3.8.1 FIB milled cross sections

A Focused Ion Beam (FEI FIB 200) of a Ga^{2+} ion source was used to mill areas of the PZT thick films to expose cross sections. Firstly, a trench was milled at a current of 6600nA. This was 10μm by 20μm, and 6μm deep and exposed the PZT film cross section. This was followed by more precise milling at the cross section to produce a clean cut. The cross section was then imaged using a SEM.

3.8.2 SEM imaged cross sections

The resolutions of the images of the FIB milled cross sections were limited. So, a higher resolution SEM (Phillips XL30-SFEG) was employed. Firstly, the cross sections were exposed. This was conducted by producing a defect at the under-side of the substrate with a diamond tipped scribe. This formed into a crack that propagated through the entire substrate and PZT film. The fracture will generally propagate through the weakest points in the film, which are porous areas and can result in an un-representative cross section. However, by initiating a fracture at the under-side of the substrate the fracture velocity can be high enough not to be significantly affected by the structure of the film. The cross sections were then imaged using a 5kV electron beam.

3.8.3 XRD stress analysis

XRD (Siemens D-5005 diffractometer) was used to estimate residual stress of the processed PZT thick films and PZT powder. This process was explained in the literature review section 2.10. The PZT thick film was placed in the XRD machine, whereby the Bragg angle of 43.0-46.5˚ was investigated. The (002) peak was determined, hence the crystal plane parallel to the substrate was analysed. Firstly, the (002) peak was measured when the PZT sample was positioned horizontally. This was considered the 0˚ sample tilt. The (002) peak was re-measured when the PZT samples were tilted at various angles from 5 to 25˚. The 2θ position at the (002) peak was determined for each sample tilt. These results were graphed as 2θ peak position vs. sample tilt and a linear relationship was determined where the gradient of the curve was proportional to the residual stress of the PZT film (Ohno et al., 2008). However, the

gradient was also proportional to the Young's modulus and the Poisson's ratio of the sample. These properties of the PZT thick films were not possible to measure so absolute values of stress could not be calculated, but it was assumed that the Young's modulus and the Poisson's ration of the PZT films did not vary significantly as a function of sintering. Therefore, the gradient value that was proportional to residual stress was used in this thesis to estimate the relative residual stresses.

Chapter 4

Thickness shrinkage of constrained PZT thick films

4.1 Introduction

The evolution of dielectric and piezoelectric properties of PZT thick films is dependent on the microstructure that develops during sintering. However, constrained sintering occurs as a consequence of the presence of an integrated rigid substrate. This results in the constraint in film shrinkage in the x-y directions during sintering. Along with this there are thermal expansion mismatches between the substrate and the film, which results in the generation of film tensile stresses and as a consequence reductions in the driving force for sintering. Moreover, de-sintering and film cracking can arise during the cooling stages.

Maximum relative densities of PZT films were required in this project. So, in this chapter the aim was to further the understanding of the evolution of density during constrained sintering. This was conducted by monitoring the macroscopic thickness shrinkage of PZT thick films at various sintering times. This work can lead to the development of a sintering schedule in which film densities can be optimised. Current techniques used to measure film shrinkage are real-time dilatometry and post sintering cross section analysis. However, the use of dilatometry was not practical with lead based ceramics because of potential lead evaporation and consequent damage to the equipment. Furthermore, only localised density changes can be identified using cross section images and errors can arise as a consequence of non-flat cross sections. Therefore, a novel technique based on monitoring the through thickness shrinkage of stand alone 5mm x 5mm areas (islands) of PZT thick films was developed.

4.2 Calculation of film shrinkage

A typical surface profile of a pyrolysed, but un-sintered PZT island is shown in Fig. 22. It can be seen that there are regions of non-uniformity. Firstly, the width of the PZT island is greater than 6mm, but a 5mm wide mask was believed to be processed. The width of the PZT islands were a function of the dimensions of the mask, therefore it is proposed that these dimensions were greater than previously believed.

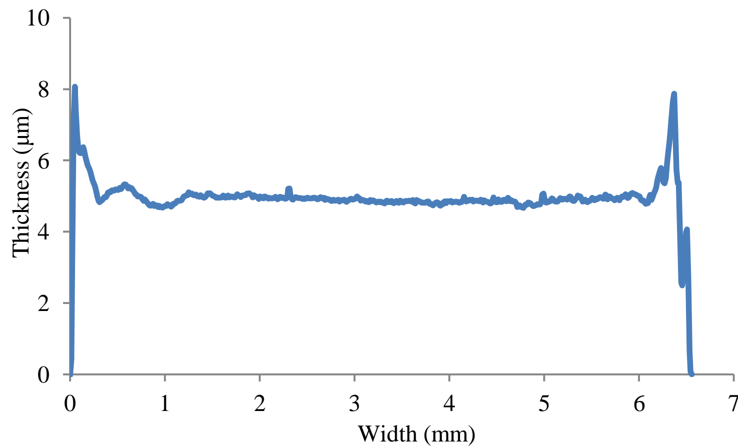

Fig. 22. Surface profile of a pyrolysed, un-sintered PZT island.

To examine this theory, the surface profile of a processed photoresist mould is displayed in Fig. 23. The width of this particular mould is 5.6mm, and thus was greater than was designed, which suggests that the other multiple moulds produced were of a similar size. To explain this, the photoresist mould fabrication and removal procedure is examined, which is described in section 3.4. After the photoresist coating was processed an acetate mask was positioned between the photoresist mould and a UV radiation source. The acetate mask was processed so that multiple regions 5mm x 5mm in size were exposed to the UV radiation. Following this the exposed regions were removed when the mould was submerged in a mixture of developer and distilled water, leaving multiple identical mould cavities. It is most probable that the apparent errors in processing the mould occurred during the development stage. It is also likely that a consequence of these processing inaccuracies was inconsistent mould sizes, meaning that the widths of the PZT islands were not constant.

It can also be seen in Fig. 22 that there are peaks in the thickness at the edges of the PZT islands. This occurred as the shape of the islands mirrored that of the photoresist mould, whereby there are also thicker regions at the edges exhibited (Fig. 23). However, the edges of the PZT islands were at an angle that was towards the centre of the island, whereas the edges of the mould were at an angle in the opposite direction. The angle of the edges of the islands may have developed during the acetone wash stage that was used to remove the photoresist mould. This could have occurred if the edge of the PZT island that was bonded to the edge of the mould was also removed during the

wash. However, experiments were conducted to find the optimum processing temperatures prior to photoresist removal in order to produce a stable PZT island without degrading the photoresist so that the photoresist was not strongly bonded to the substrate and could be removed easily. Prior to the acetone wash the sample was heated to 140˚C, but this resulted in a weak PZT film and some of the deposited slurry was removed with the photoresist during the acetone wash. At temperatures around 180˚C the photoresist coating cracked and was difficult to remove. At a processing temperature of 165˚C the PZT film was not visibly damaged during the acetone wash. The photoresist mould could be removed, but at the regions near the PZT islands there was some difficulty in fully removing the photoresist. This temperature was chosen as the processing temperature as it resulted in the best balance of the outlined requisites, but the edge effects that have been seen are likely to be a function of either damage to the edges of the PZT islands or non-complete photoresist removal.

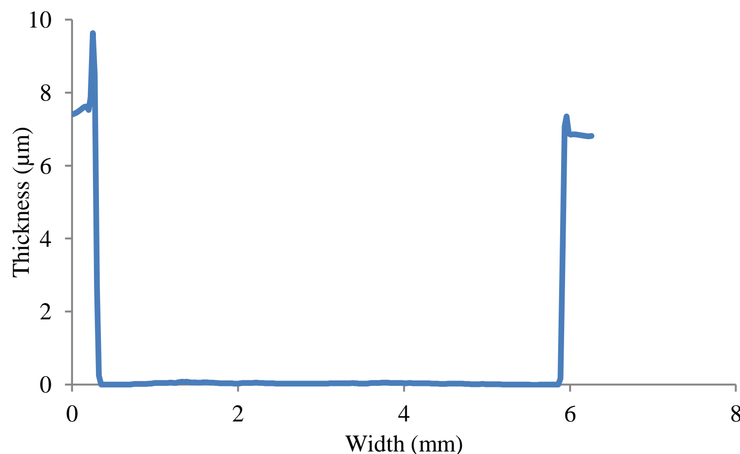

Fig. 23. Surface profile of a developed photoresist mould.

Similar edge effects including peaks in thicknesses, receding walls and low wall angles are commonly seen when films are processed using masks (Wang et al., 2009). Therefore it is not unique to this work. Furthermore, the edge profiles were not representative of the profiles of the PZT islands. Therefore, the edges of the profiles of the PZT islands were ignored in the profile analysis, and thus not considered during shrinkage results.

In order to determine the average thickness after pyrolysation and sintering of a PZT island only the central region was considered. However, there were still surface defects seen. These were grouped into two categories. Firstly, abnormal deposition resulted in large splats on the surface of the films. This occurred when the stability of the cone-jet of the sprayed slurry momentarily reduced. Secondly, cracking was seen that resulted in crevices and peaks in the profiles, which almost exclusively occurred during the pyrolysation stage. The film cracking that occurred was visible when observed without the need for magnification. Typically, cracking occurs as a consequence of high levels of liquid removal during pyrolysation. However, the pyrolysation temperature of 350˚C has not been reported to result in cracking in PZT thick films (Wang et al., 2008). It was observed during the drying experiments that visible damage to the PZT islands occurred during the acetone wash when lower processing temperatures were applied. This suggests that non-observed damage could have occurred when the processing temperature of 165˚C was used, followed by the propagation of cracks during pyrolysation. This signifies that cracking was an inherent problem when using acetone wash stages during mask removal, but is unlikely to occur when acetone washes are not used. However if the cracks were to occur in functional ceramics an effect would be a degradation in the electrical properties. Furthermore if the cracks occurred through the thickness of the film there could a shorting of the top and bottom electrodes.

To determine the average shrinkage quantitatively, the surface profiles of the un-sintered and the sintered PZT islands were characterised using a line of best fit. Different lines of best fit were considered so that the curve that represented the surface profiles most accurately was used. A 2nd order polynomial fit and a linear fit were used, displayed in Fig. 24 and Fig. 25, respectively. The fits were applied to a profile of an un-sintered PZT island which was subsequently sintered for 5 minutes. Prior to the application of the lines of best fit the start of the profiles were positioned at zero on the x axis. This was done so that the same region on the curve for the un-sintered and sintered profiles could be directly compared. There was a bow observed in the un-sintered island as the central position of the island was less thick than the edges. There were also two defects seen on the surface. These were not cracks, as neighbouring crevices were not seen. Therefore, these were assumed to be splats of deposited slurry.

The sintered island shrunk in the through thickness direction and the surface also became flatter. The bowed surface that was typically seen was more accurately represented by the polynomial fit. It can also be seen that the effect of the defects on the polynomial curve was not significant.

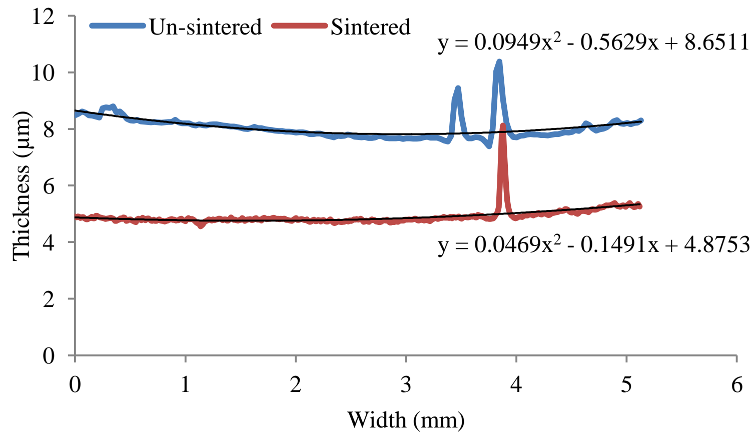

Fig. 24. Surface profile of a PZT island, un-sintered then sintered for 5 minutes, with a polynomial curve fit.

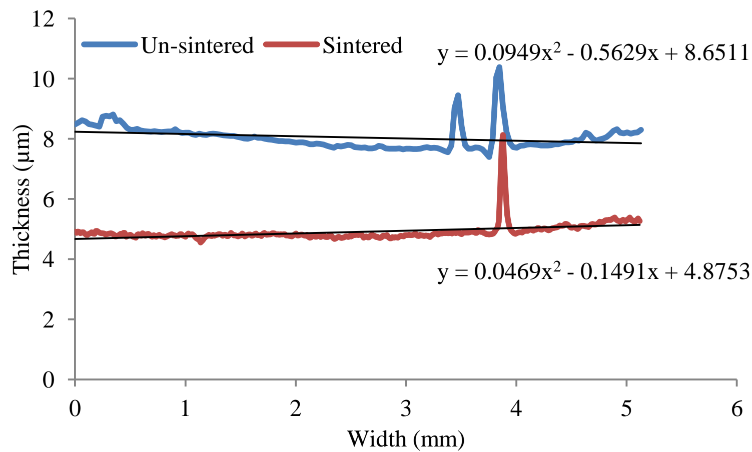

Fig. 25. Surface profile of a PZT island, un-sintered then sintered for 5 minutes, with a linear fit.

The polynomial equations were then used to determine the shrinkage of the films with sintering. The y value, or thickness, was calculated at a given x point in the range of 0-5mm using an increment of 0.05mm. In this way the thickness at each x point of the un-sintered and sintered film could be directly compared. Consequently a percentage

difference of the thickness and thus shrinkage at each x point was calculated. The shrinkages were then averaged, and a standard deviation error was determined.

4.3 Comparisons of shrinkage

To determine the shrinkage of the islands the profiles of an un-sintered island was determined, then sintered, then the profile determined again. So the profile of a specific island could be compared prior to and post sintering. So firstly, to put the shrinkage results into context, the average thicknesses of the un-sintered PZT islands are displayed in Fig. 26. This is displayed as a function of the sintering time that was to be applied to these un-sintered films so that these results can be compared to shrinkage results as a function of sintering time later in this section.

Comparisons of the two sets of islands were not appropriate because identical and uniform deposition would have to be assumed, although identical thicknesses across all samples were wanted. There were identical EHDA deposition parameters thus the deposition thicknesses should be similar, but the accuracy of thickness repeatability in this context should not be assumed. It can be seen that similar thicknesses were generally obtained for set 1. However, the islands that were to be sintered for 7.5 and 10 minutes exhibit greater thicknesses. This must be considered when analysing the shrinkage results of these islands. Ignoring these points, the average thicknesses of the islands are at a range from 6.38 to 7.79μm. So any variations in the thicknesses of these islands after sintering must be a consequence of sintering. It is also noted that there was no cracking observed for set 1. For set 2, the islands that were to be sintered for short times exhibit greater average thicknesses. There are similar thicknesses of the remaining islands, which is between 6.42 to 7.05 μm. However, it can be seen that the error bars associated with these results are large, which may affect the accuracy of the shrinkage results. The large errors were a consequence of multiple cracks in the islands that occurred during pyrolysation.

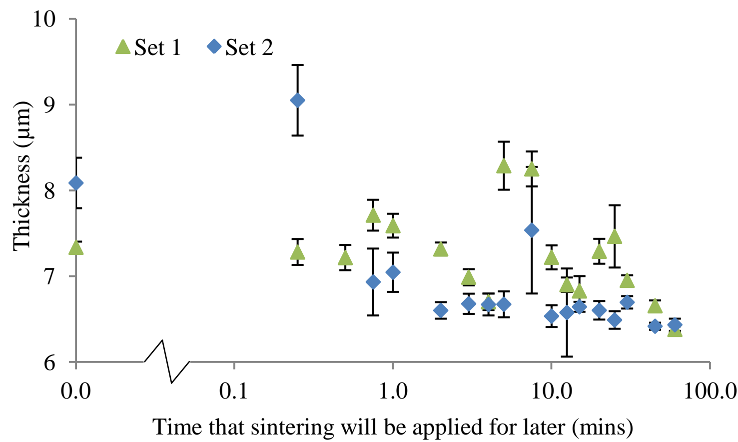

Fig. 26. Variations in the thicknesses and the associated standard deviation of two sets of un-sintered PZT islands as a function of the time that a sintering temperature of 725ºC was to be applied for later.

The shrinkages of the PZT islands, which were determined from the thicknesses of the un-sintered and sintered islands, are displayed in Fig. 27. Positive results of shrinkage means that the thickness of a sintered PZT island was lower than that of the un-sintered PZT island, indicating that densification due to sintering occurred. However, it can be seen that apparent shrinkage occurred at 0 minutes in set 1, but heating was not applied. This result was not an artefact of inaccuracies in the experiments as there was a high precision of the surface profiler and low levels of surface defects observed.

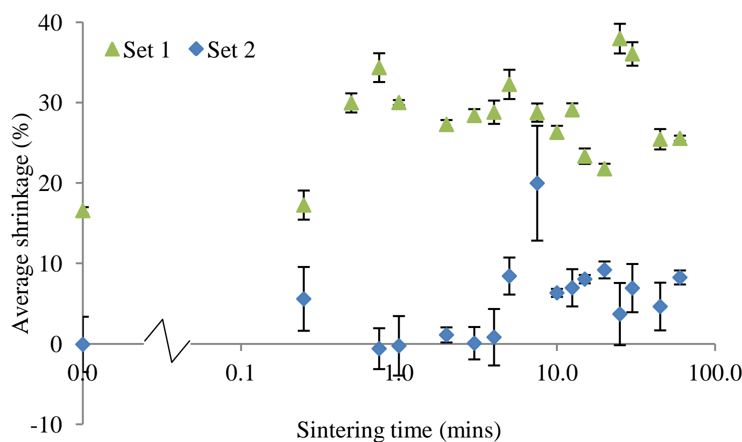

Fig. 27. Variations in the shrinkage and the associated standard deviation of two sets of sintered PZT islands as a function of the time at a sintering temperature of 725ºC.

In order to explain the apparent shrinkage of the PZT island when a temperature of 725ºC was not applied, the heating process was analysed. The PZT islands were processed on the same silicon wafer. Firstly, the profiles of the un-sintered islands were determined using a surface profiler. Following this the islands were sintered individually. From the centre of a PZT island the adjacent island was positioned 10mm across the wafer. Therefore, the PZT island that was not sintered was at a distance of 10mm across the wafer from a temperature of 725˚C. The thermal conductivity of the silicon wafer was 131-160$Wm^{-1}k^{-1}$ (Sōmiya et al., 2003) (http://www.novawafers.com). It is clear that the PZT island that was not heated at 725ºC was also heated during the sintering process. However, it is not believed that this additional heating resulted in sintering, because it is believed that to sinter a PZT island a temperature of at least 680˚C was required. At this temperature the sintering aids that were added in the slurry are activated and consequently a liquid phase is produced and as a result sintering matter flow is promoted (Corker et al., 2002). The absolute value of the temperature that the un-sintered island was subjected to was unknown, but a temperature as high as 680˚C was unlikely. Therefore, it is assumed that shrinkage must have occurred without sintering, and it is postulated that it occurred due to further pyrolysation.

Prior to pyrolysation the PZT islands were dried in order to remove liquid and initiate shrinkage of the film. Following this, the temperature applied to initiate pyrolysation was 350˚C. The solvent used, ethylene glycol, had a boiling point of 196-198˚C (Sigma Aldrich), so it is assumed that any residual liquid was removed at this stage. Pyrolysation is conducted to remove organic compounds. These degrade into water vapour and carbon dioxide upon heating, as a result porous regions open up when these escape the microstructure (Qiu et al., 2009). Therefore, all organic compounds are required to be removed before sintering is conducted. The temperature of the un-sintered PZT island when an adjacent island was sintered was likely to have surpassed 350˚C as a result of additional heating due to substrate heat transfer. Thus, any residual organic compounds in the island would have been removed, resulting in a decrease of the volume of the island. Therefore, it is believed that the shrinkage of the un-sintered PZT island occurred as a result of incomplete pyrolysation followed by full pyrolysation during the sintering process.

4.4 Disparities in pyrolysation

As stated there was shrinkage seen at 0 minutes in set 1. The shrinkage measured at 0 to 0.25 minutes is considered to be a result of the completion of pyrolysation with further shrinkage beyond this point considered to be due to sintering. However, there was no shrinkage of set 2 in the same period of time. So there must have been larger levels of residual organics present in set 1. A similar conclusion can be drawn from the results of the thicknesses (Fig. 26), whereby set 2 was of lower thickness than set 1 after pyrolysation. However, as discussed, care must be taken when comparing the thickness results. It is postulated that set 2 was subjected to more complete pyrolysation. For this to have occurred the islands must have been subjected to different temperatures; potentially due to temperature variations and fluctuations of the hot plate used.

The disparities in the pyrolysing conditions were likely to have had an effect on the shrinkage results. To examine this, PZT islands were heated at a temperature of 300˚C and surface profiles were determined. In this way it can be assumed that there were residual organics present. Following this, a temperature of 400˚C was applied and it was assumed that all organics were removed without sintering occurring. The surface profiles were then re-measured. The average shrinkage was determined to be 27.01%±8.49. In comparison, when a temperature of 350ºC was applied followed by full pyrolysation a shrinkage of 16.55%±0.43 was seen (Fig. 27). Therefore, this indicates that significant shrinkage can occur as a consequence of organic removal.

To further examine the effects of the pyrolysing temperature images of a PZT island pyrolysed at 300˚C and 400˚C, respectively, are displayed in Fig. 28. It can be seen that at this magnification there appeared to be a uniform surface of the island pyrolysed at 300˚C. However, as a result of the increases in shrinkage initiated during the higher pyrolysing temperature cracking occurred. In Fig. 26 and Fig. 27 it can be seen that the error bars associated with the results of set 2 were much greater than with set 1. This was as a result of more frequent cracking of set 2 during the pyrolysation stage, which is assumed to occur as a result of greater shrinkage of the islands. However, cracking of set 1 did not occur during the sintering stage when the residual organics were removed.

It is hypothesised that essentially a two step pyrolysis occurred, whereby initial partial pyrolysis resulted in a level of shrinkage which did not result in cracking. Following this, there could have been a rearrangement within the material resulting in lower stresses, so when the residual organics were removed the shrinkage again did not result in cracking. It must also be considered that the organics were most likely removed when an adjacent island was sintered as a result of thermal conductivity across the substrate. Therefore, as the film uniformity of set 1 was greater, it appears that using the lower pyrolysing temperature is advantageous.

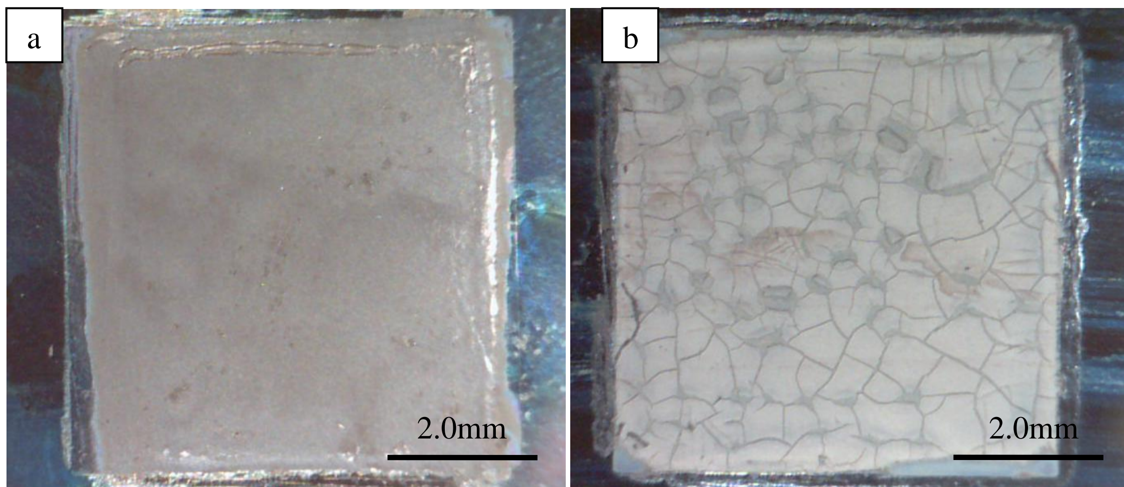

Fig. 28. Optical microscope images of the top surface of a PZT island pyrolysed at a) 300˚C, followed by at b) 400˚C.

4.5 Shrinkage due to sintering

Thicknesses of the sintered films of set 1 and set 2 are displayed in Fig. 29 and Fig. 30, respectively.

4.5.1 Set 1

For set 1 the shrinkage measured at 0 minutes was 17%, with further shrinkage considered to be due to densification during sintering. It is seen that for short sintering times, less than 1 minute, there is shrinkage of the films. These results represent an increase in relative density in the z direction. This was assumed to be a result of the activation of the added sintering aids in the film, whereby the resultant liquid phase

adhered to the grain boundaries producing a low resistant diffusion path for sintering matter. It has previously been observed that during constrained sintering, shrinkage in the x-y direction is inhibited, but shrinkage in the z direction is unrestricted (Cipitria et al., 2009). Therefore, it is possible that the shrinkage observed occurred as a result of essentially free sintering in this direction. Following this, the is at a plateau shrinkage for the remainder of the sintering schedule, which means that there was no further densification in the z direction. This is unlikely to be an effect of the substrate as densifying matter flow in this direction is thought to be unconstrained (Cipitria et al., 2009). It is more probable that densification stops because maximum achievable densities in the z direction are obtained within 1 minute of sintering. There is also a plateau in the thicknesses of the sintered islands at this stage (Fig. 29). This plateau is seen even though there were some variations in the thicknesses of the un-sintered islands, in particular the islands that were subsequently sintered for 5 and 7.5 minutes, whereby the thicknesses of the un-sintered islands are high. Subsequently, after sintering the shrinkage of these islands is also high, but the final thicknesses are similar to that of the other islands suggesting that similar levels of sintering occurred. Thus, this variation in shrinkage, and the variation in the thicknesses of the un-sintered islands is assumed to be a result of the differences in the level of pyrolysis. It is also postulated, as similar thicknesses were found after sintering, that there was an initial uniform deposition thickness of the PZT slurry. This was also believed because during deposition it was observed that there was a uniform cone-jet spray and slight momentary variations in spray should be evened out due to the multi layer deposition used to build up the films. So it assumed that the variations in the thicknesses of the islands prior to pyrolysation were low.

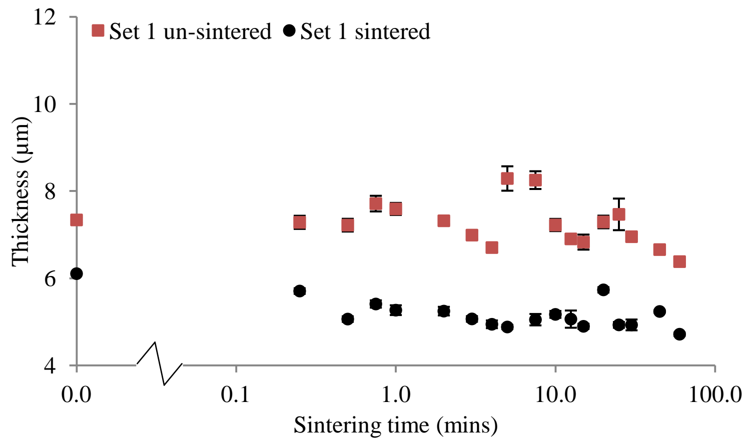

Fig. 29. Variations in the thicknesses and the associated standard deviation of the un-sintered and sintered PZT islands set 1 as a function of the time at a sintering temperature of 725ºC.

4.5.2 Set 2

It can be seen that there was almost no shrinkage at 0 minutes, so it can be assumed that there was no, or only small amounts of organics present after pyrolysation. With sintering initially there is no shrinkage seen, indicating that densification did not occur. It can be seen in Fig. 30 that the thicknesses are larger at short times, which may indicate towards a disparity in the pyrolysed films within set 2, which was likely to have affected the sintering of these islands. At longer sintering times there is gradual shrinkage seen. The difference between the un-sintered and sintered thicknesses however is small, and at a plateau.

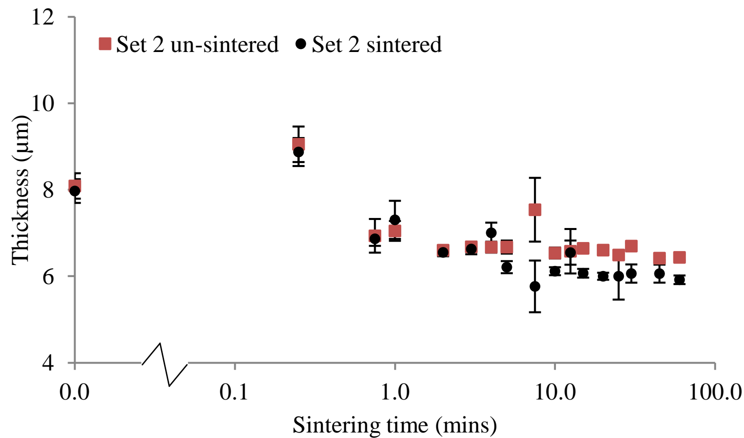

Fig. 30. Variations in the thicknesses and the associated standard deviation of the un-sintered and sintered PZT islands set 2 as a function of the time at a sintering temperature of 725ºC.

To explain these occurrences, there are three hypothesise presented. If it assumed that uniform deposition occurred so that there were similar volumes of the pre-pyrolysed islands, then there were disparities in the level of pyrolysation each island was subjected to. This may also mean that due to the gradual decrease in the sintered thicknesses that densification did occur at short sintering times. Alternatively, if densification did not occur until mid-sintering times as suggested from the shrinkage results, then the initial heating and sintering aid activation, which is assumed to result in matter diffusion, must have not resulted in densification until later in the sintering schedule. This however would be a strange phenomenon, and different to that seen in set 1. Finally, due to the cracking of the islands, it may not be possible to accurately conclude what occurred.

Investigations of these theories were conducted by examining the profiles more closely. Firstly, the profile of the island sintered for 1 minute is displayed in Fig. 31. There are peaks in thickness seen across the centre of the island, which is a result of cracking that occurred during pyrolysation. As a consequence there were errors in the determination of the thicknesses and shrinkage. It can also be seen that the thicknesses of the profiles determined before and after sintering are very similar, which resulted in the calculation of low shrinkage. Therefore, it appears unlikely that errors occurred in the processing of these results, meaning that it was likely that densification did not occur with 1 minute of sintering.

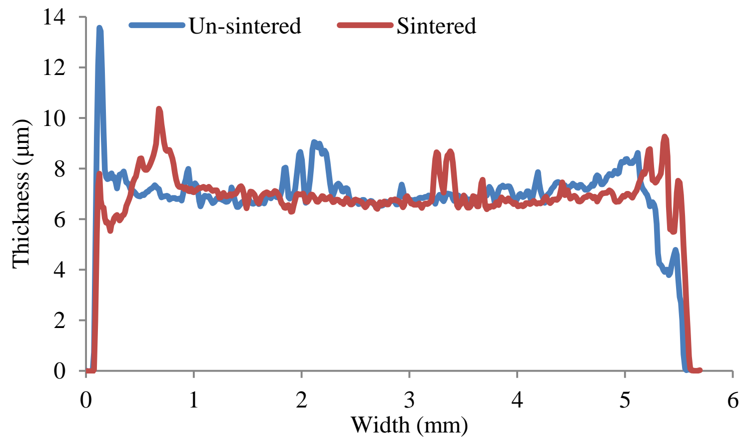

Fig. 31. Surface profile of a PZT island in set 2 un-sintered and subsequently sintered for 1 minute at 725°C.

This is in comparison with the profile of the island sintered for 7.5 minutes is displayed in Fig. 32. Predominant cracking can be seen in the profile of the un-sintered island, and there does not appear to be any changes in the degree of cracking with sintering. As a result of the cracking the errors associated with the shrinkage and thickness results were high. The profile is less thick in the z direction after sintering, thus it appears that densification occurred with 7.5 minutes of sintering. However, as the profiles were not measured at the same points, and the island is clearly non-uniform, it is possible different shrinkage may be determined if a different region of this island is examined. This means that these results are not entirely reliable.

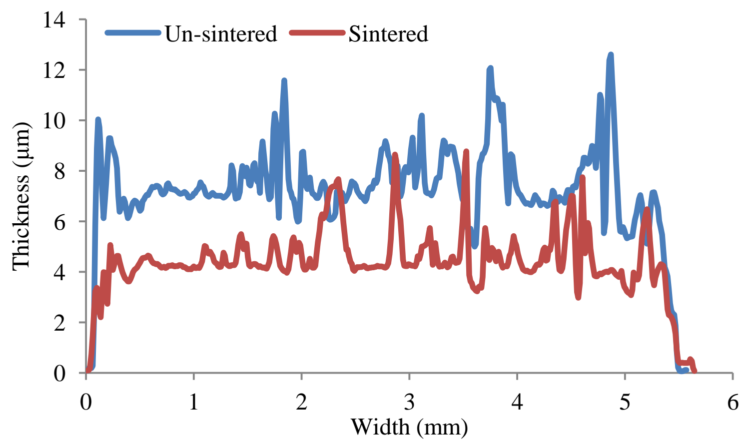

Fig. 32. Surface profile of a PZT island in set 2 un-sintered and subsequently sintered for 7.5 minutes at 725°C.

It has been shown that the errors associated with the shrinkage results correlate with the amount of cracking that occurred. Therefore, it can be seen that there is a disparity in the amount of cracking that occurred across the samples in set 2. If the amount of cracking can be considered a function of the degree of pyrolysation, this would also mean that there was a difference in the amount of pyrolysation that occurred. However, cracking was assumed to initiate because of weak films, which developed during the acetone wash stage. Thus, the amount of cracking is not entirely proportional to the degree of pyrolysation, but does indicate towards it. Furthermore, a consequence of cracking was unreliable shrinkage results. Therefore, it appears that that there was a disparity in the level of pyrolysation within set 2. This then led onto large errors of shrinkage so that it is difficult to conclude accurately the densification profile with sintering. However, it appears that likely that sintering may have occurred later in the sintering schedule compared to set 1, but the level of film shrinkage was low.

4.5.3 Comparisons of set 1 and set 2

In order to directly compare the final films of set 1 and set 2 micrographs are displayed in Fig. 33. In this way the errors that arose in the pyrolysis procedure do not have an effect. It appears that the densities of set 1 are greater than set 2, but the differences do not appear significant. Therefore, it is possible that similar rates of densification occurred up to this stage, or that significant densification did not occur in either set.
It was also postulated in the previous section that densities in the z direction may be maximised. This is difficult to identify as these images were taken at a 45° angle so the low amounts of porosity seen in the z direction are likely to be an artefact of this. It is also noted that there is no cracking observed in the microstructures of set 2. Thus, the surface cracks observed did not propagate throughout the film.

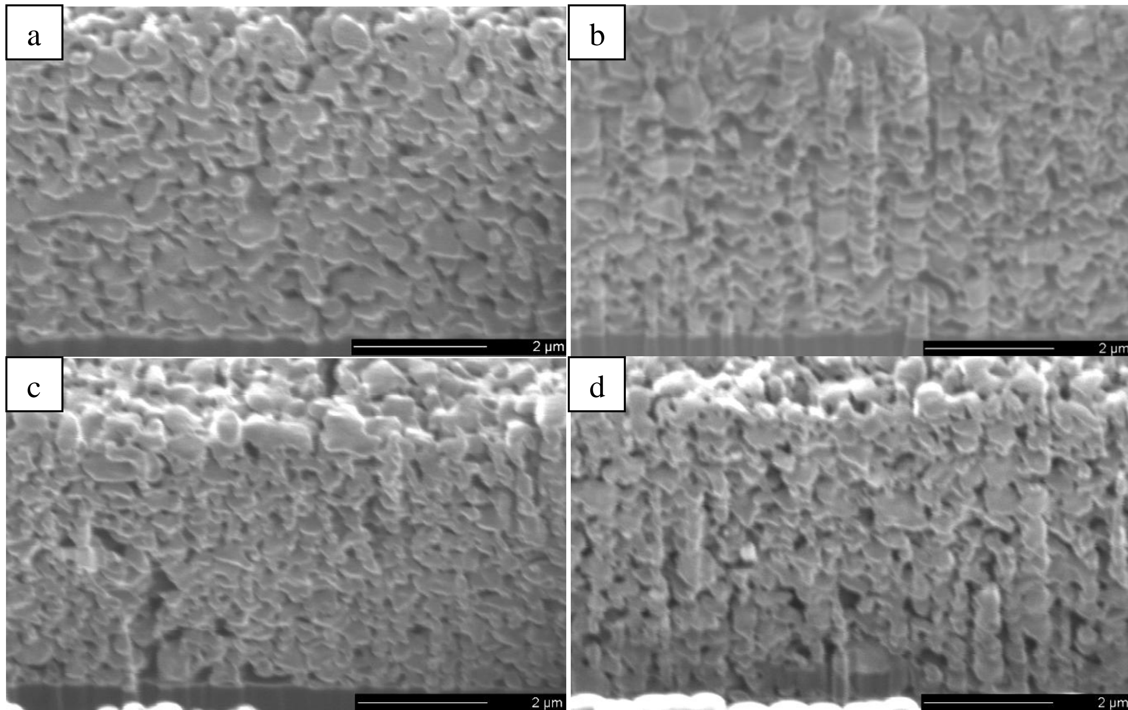

Fig. 33. SEM micrographs taken at a 45º angle of FIB cross sections of PZT islands sintered at 725˚C for a) 3 minutes, set 1, b) 3 minutes, set 2, c) 5 minutes, set 1, and d) 5 minutes, set 2, respectively.

4.6 Chapter conclusions

In this chapter the aim to further the understanding of densification due to sintering was addressed by measuring shrinkage of films as a function of sintering time. One issue that arose during these experiments was the variations in the pyrolysation conditions. As a consequence the results that have been presented are not fully confirmed. Nonetheless, it is indicated that densification occurs during the early stages of sintering when a rapid ramp rate and sintering aids are used. This indicates towards the use of a sintering schedule of only a few minutes, as there appears to be no further gains to be achieved with longer sintering times. Further findings of significant heat transfer across the silicon wafer were presented in this chapter. Heat transfer resulted in a temperature greater than 350˚C at a distance of 10mm away from the sintering zone. This means that for sintering using the halogen bulb heat transfer has to be considered.

Chapter 5

Dielectric and piezoelectric properties of constrained PZT thick films.

5.1 Introduction

The aim of this chapter was to expand on the understanding of the evolution of PZT thick films under constrained sintering conditions. This was done by examining the changes in dielectric and piezoelectric properties as a function of sintering time. To explain the changes in the properties, the microstructural and stress development was investigated. The analysis was conducted on films produced using an ethylene glycol based slurry (EGS). Following this, a second set of films were processed without sintering aids (NS) to identify the effect of liquid phase sintering; and a final set of films were produced using a 2-ME solvent based slurry to compare the effects of constrained sintering. These films were all processed at a temperature of 725˚C for sintering times between 0 to 60 minutes. This was followed by electrical property characterisation, cross section imagery, density, grain size and residual tensile stress measurements.

5.2 Constrained sintering of EGS films

The relative permittivity of the EGS PZT thick films, repeated 5 times per result and averaged with errors, is displayed in Fig. 34. Relative permittivity can be used as an indication of how well sintered the films were. These results can be split into three regions. Firstly, it can be seen that within the first 2 minutes of sintering that there is a rapid increase in the relative permittivity culminating in a transitory peak in properties, followed by an immediate decrease. In the second region there is a plateau in relative permittivity between 2 to 30 minutes of sintering. This plateau could be due to constrained sintering effects. Finally, with sintering times longer than 30 minutes there is a decrease in the relative permittivity, suggesting film degradation. The d_{33} results, repeated 5 times per result, are displayed in Fig. 35. The reader is reminded that the d_{33} is the piezoelectric coefficient of the material where an electric field is applied perpendicular to the substrate, and the volume change of the film is measured parallel to the electric field. There is further information on the piezoelectric coefficients in section 2.3. Care must be taken in interpreting the d_{33} results as the piezoelectric properties can also be affected by other mechanisms such as residual stress and domain pinning. It can be seen that the d_{33} exhibits similar trends to the relative permittivity. In

the first region there is a rapid increase culminating in a transitory peak at 1 minute of sintering, followed by a decrease. In the second region there is a broad plateau in d_{33}, followed by decreases in the third region. These regions outlined will be discussed along with microstructure analysis and residual stress estimations.

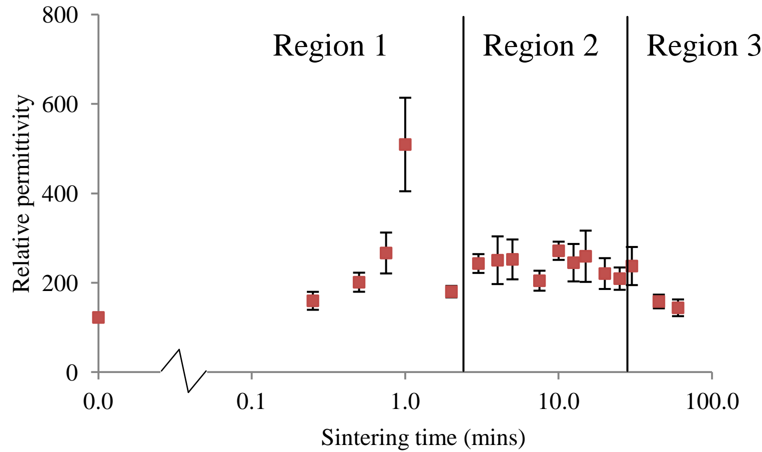

Fig. 34. Variations in relative permittivity and the associated standard deviation of EGS films as a function of sintering time at a processing temperature of 725˚C.

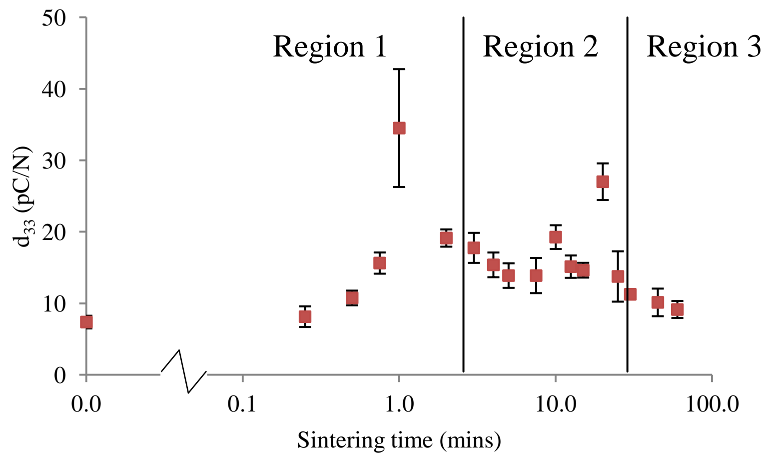

Fig. 35. Variations in d_{33} and the associated standard deviation of EGS films as a function of sintering time at a processing temperature of 725˚C.

5.3 EGS films: Region 1

To examine why the electrical properties in region 1 increased rapidly, and subsequently decreased, first micrographs are displayed Fig. 36. There is no observable

development of the microstructure during the early stages of sintering, with small grains and frequent small pores observed. This may have occurred because of low levels, or possibly no matter rearrangement during sintering. However, it is difficult to identify changes in porosity, but it was indicated in Chapter 4 that there was an increase in film density at these sintering times. Following this, significant changes in the microstructure are seen at 1 minute of sintering. The sizes of the pores are greater but they are less numerous than seen in the previous images. In relation with the results in Chapter 4, it is likely that there is an increase in film density at this sintering time. Grain boundaries are difficult to identify, possibly because of a result of grain growth; or because the resolution of the image was not high enough to resolve grain boundaries, which could mean that there were unseen multiple grains at these regions. This microstructural rearrangement coincided with the peak in electrical properties. This could mean that the physical properties of this microstructure facilitated the development of the electrical properties. In subsequent images small grains and small pores are observed and the microstructure appears very similar to the microstructure observed between 0 to 0.75 minutes of sintering. Therefore, further microstructural rearrangement occurred between 1 to 2 minutes of sintering. It is postulated that the electrical properties are a function of the microstructural development. This is because throughout region 1, except at 1 minute of sintering, there were similar electrical properties and microstructures seen. Whereas, at 1 minute of sintering there was a transitory peak in properties and a unique microstructure observed. The physical properties that can affect the electrical properties are relative density, grain size and residual stress. These are investigated in the following section. This is followed by the discussions of the reason for the microstructural rearrangements.

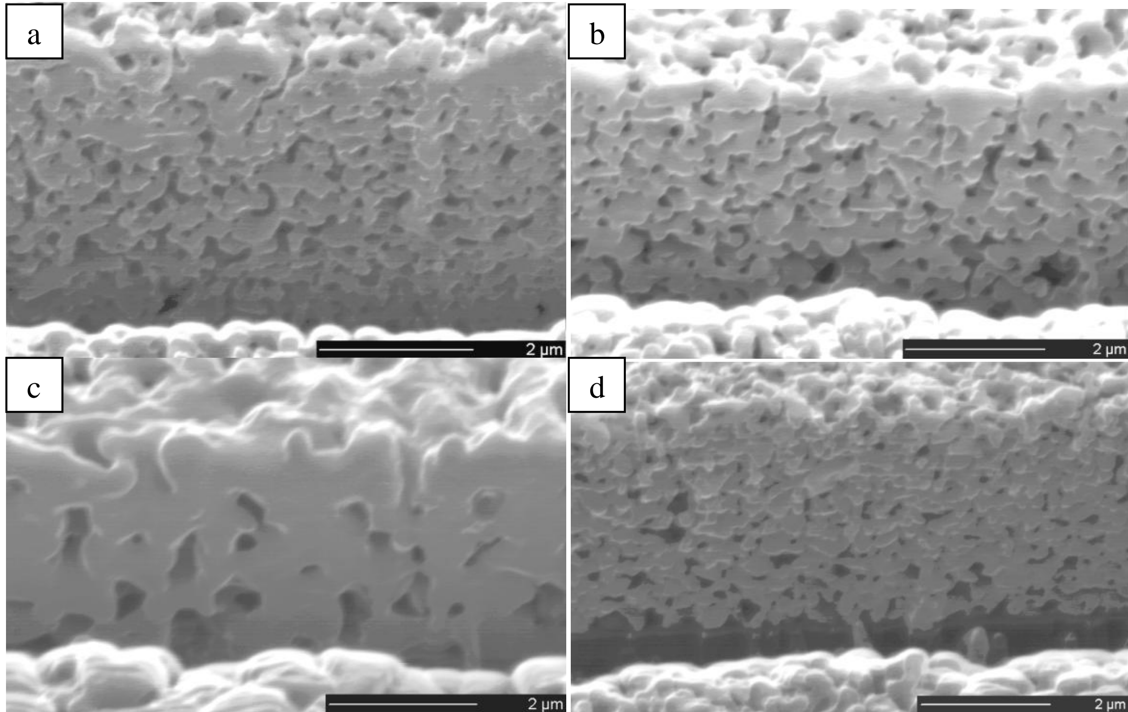

Fig. 36. SEM micrographs of FIB developed cross sections of EGS films sintered at 725˚C for a) 0 minutes, b) 0.75 minutes, c) 1 minute, and d) 2 minutes, respectively.

5.3.1 Region 1: Densification

It has been reported that during the early stages of sintering that the microstructure undergoes changes via surface diffusion of matter from areas of high surface free energies to low. To result in densification this requires mass transport from within grains to pores (Moulson and Herbert, 1989). Densification results in increases in the relative permittivity exhibited by a material because there is more dielectric material for a given volume to store charge. Furthermore, increases in densities can result in increases in piezoelectric properties. A consequence of higher densities is that with the application of an electric field there is a greater volume change of the film, thus the d_{33} exhibited by the film increases (Dorey et al., 2002).

A hypothesis for the reason of the transitory peak is that there were significant changes in the relative density of the films in region 1. However, due to limited resolution and uncertainties in the accuracy of the cross sections representing the non-imaged microstructures, the identification of porosity through imaging was not practical. In order to identify porosity as a function of sintering time, macroscopic film shrinkage

data taken from Chapter 4 was used. Additionally, electrical measurements of dielectric loss were used to indicate porosity levels.

It was suggested in Chapter 4 that densification occurred gradually in the thickness direction at up to 1 minute of sintering, but then there was no change in density from 1 to 2 minutes. However, there were uncertainties over the accuracy of these results due to inconsistent processing of the PZT islands. Additionally, these results only indicated shrinkage in the z direction, although it has previously been shown that shrinkage in the x-y directions will not occur in constrained sintering (Dorey and Whatmore, 2004b). To support these results, the dielectric loss is displayed in Fig. 37. There is a gradual decrease in loss followed by levelling off towards the end of region 1. Dielectric loss is affected by numerous mechanisms, notably a lag in polarisation as domains are not polarised instantaneously with the application of an electric field, and crystal and domain wall defects also reduce the dielectric capabilities of a material. However, it has been shown that when added porosity has been introduced in a PZT body that the associated loss dramatically increases (Kumar et al., 2006). This occurs because there is a reduction in the effects of an applied electric field inducing domain wall motion at these regions, which results in higher losses. Furthermore, losses may increase with porosity due to the accumulation of space charges at the grain boundary and due to conductivity increases (Praveenkumar et al., 2006). Therefore, the decrease in loss in the early stages of region 1 may be due to decreases in porosity, which would agree with the shrinkage results. This would also mean that with longer sintering times there were constant porosities in the films. However, there was higher relative permittivity at 1 minute of sintering, but similar losses were exhibited at 1 minute of sintering and at longer sintering times. Thus, it appears unlikely that the level of porosity in the film affected the relative permittivity, so the higher relative permittivity at 1 minute of sintering may be explained by the apparent larger grains, rather than the effect on domain wall motion at the grain-pore boundaries.

It was postulated in Chapter 4 that densification occurred early in the sintering schedule as a consequence of liquid phase sintering that occurred at temperatures higher than 680ºC (Corker et al., 2002) resulting in rapid densifying matter flow, before maximum

obtainable densities in the z direction were achieved. The discussions presented in Chapter 4 can now be built upon because of extra information in the form of cross section images. During the early stages of region 1 matter flow resulted in increases in density in the z direction, but it appears that no grain growth occurred. At 0.75 to 1 minute it appeared that the rates of the densification reduced, alongside this there was significant microstructural rearrangement and apparent grain size increases. The apparent grain growth may have been a consequence of the microstructural rearrangement, with the densification rates decreasing as a result (Gupta, 1972). Between 1 to 2 minutes of sintering it again appeared that the densification rates reduced. There was more microstructural rearrangement seen and possibly reductions in the sizes of the grains which may have been a consequence of the rearrangement.

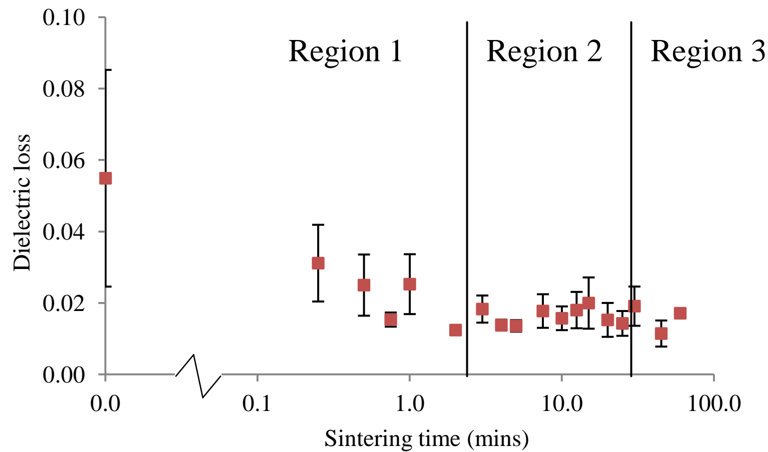

Fig. 37. Variations in dielectric loss and the associated standard deviation of the EGS films as a function of sintering time at a processing temperature of 725˚C.

It can be seen that the relationship of the densification and the electrical properties with sintering time differed. During the early stages of region 1 there were small increases in electrical properties, and also increases in densities. The increase in the electrical properties may have been a function of density increases, but this would mean that either the effect of density increases on electrical properties was small, or that the increases in densities were not significant. During the latter stages of region 1 there were significant changes in the electrical properties, but only small, possibly negligible changes in density. Therefore, it is concluded that the transitory peak in electrical properties was not a consequence of changes in the relative density of the films.

5.3.2 Region 1: Grain growth

It has been proposed that the unique microstructure observed at 1 minute of sintering exhibited larger grains. However, this cannot be conclusively proven from the FIB SEM images. So cross sections were exposed by fracturing the substrate and film, and imaged using a high resolution SEM. These micrographs are displayed in Fig. 38. Firstly, comparisons between the images of FIB and fracture developed cross sections are discussed. It can be seen that at 0 and 0.75 minutes of sintering that there are small grains with inter-dispersed small pores, similar to that seen in the FIB developed images. At 1 minute of sintering a similar structure to that seen in the FIB developed image can be seen. There are regions of tightly packed grains where there are coarsened grains and no pores present, but there are also some very small grains present. This related to the regions seen in the FIB developed images where it appeared that large grains existed. This confirms that this was actually regions of large tightly packed grains, and that some of the smaller grains were not visible. At 2 minutes of sintering it can be seen that there were large dark regions. This structure greatly differs to that seen in FIB developed images. So it is likely that this is a consequence of a non-uniform fracture, and thus not useful in these examinations.

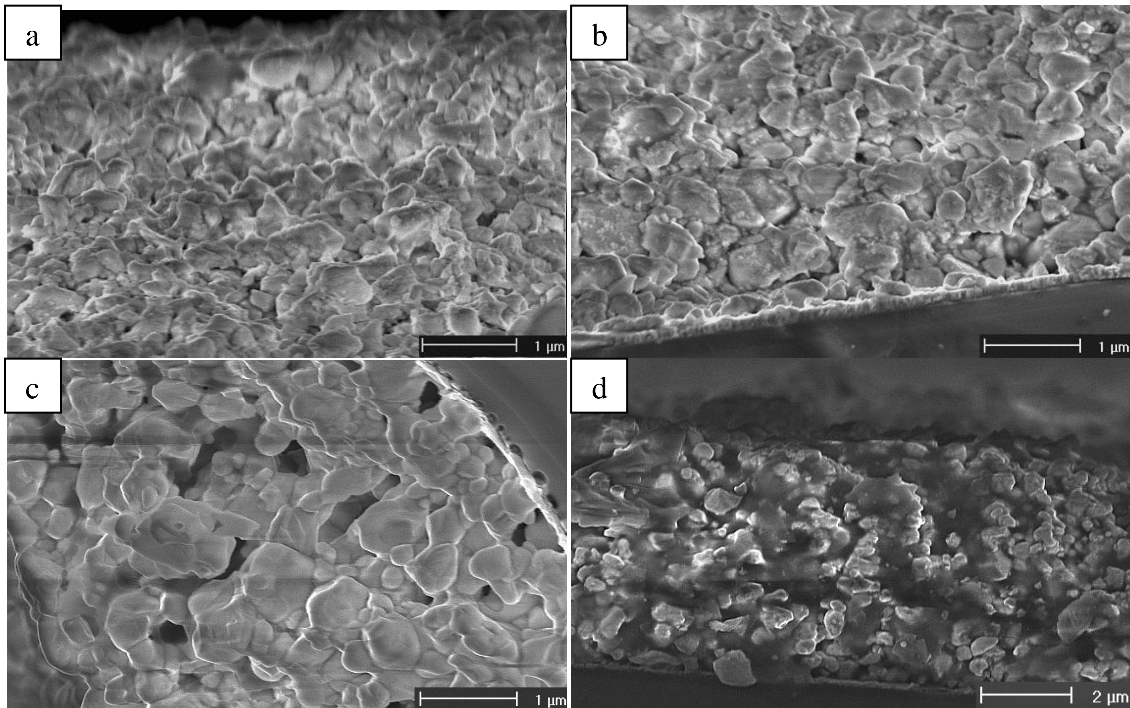

Fig. 38. SEM images of cross sections of the EGS films sintered at 725˚C for a) 0 minutes, b) 0.75 minutes, c) 1 minute, and d) 2 minutes, respectively.

The sizes of the grains that were determined over multiple images per result is displayed in Fig. 39. The sizes of the grains were determined using the linear intercept technique (Wurst and Nelson, 1972); however this method was modified by the author. In the early stages of region 1 it can be seen that the grain sizes gradually increase. This is followed by a peak at 1 minute of sintering, which is also associated with a large standard deviation. Towards the end of region 1 the grain sizes decrease.

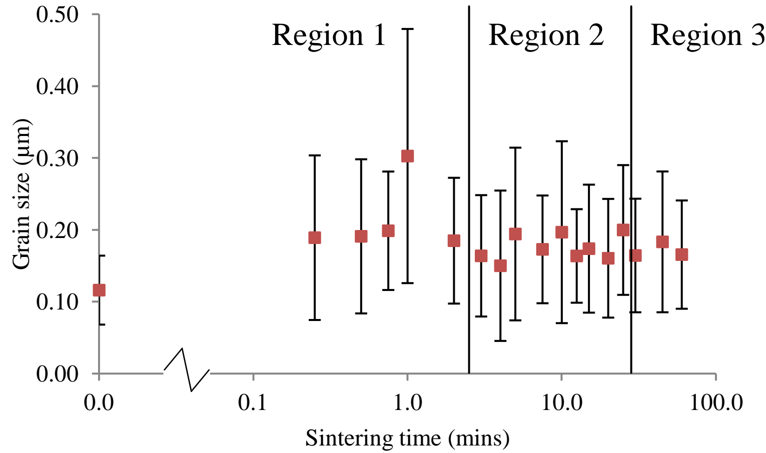

Fig. 39. Variations in the grain sizes and the associated standard deviation of the EGS films as a function of sintering time at a processing temperature of 725˚C.

The increase in grain sizes during the early stages of region 1 occurred due to grain growth. This is a consequence of normal liquid phase sintering, whereby densifying and non-densifying matter rearrangement results in grain neck growth (Rahaman, 1995). This grain growth coincided with densification of the films, which suggests that the effect of grain growth did not result in a reduction in densifying rates as previously theorised. At 1 minute of sintering the average grain size greatly increases. This may have had the effect of reducing densifying rates, but this is not confirmed by observations. To understand why the microstructural rearrangement resulted in this, grain growth mechanisms must be considered. At 0.75 minutes of sintering there was a relatively uniform microstructure. Subsequently, microstructural redistribution occurred resulting in larger grains and pores. Large areas of grain-grain contacts, as seen at 1 minute of sintering, can facilitate coalescence where migration of the grain boundary and liquid phase occurs as a result of the flow of matter to larger grains. Coalescence can also occur through solution precipitation whereby matter flows from the opposite side of a smaller grain through the liquid phase towards a larger grain. As a consequence of coalescence larger grains increase in size whereas the sizes of the smaller grains reduce (Rahaman, 1995). The result of this mechanism can be seen as the distribution of the sizes of the grains increased, this can also be seen in the images of film cross sections, as there are larger grains neighbouring very small grains. These results are a strong indication that coalescence occurred, but that the complete consumption of the smaller grains was incomplete at this sintering time.

Following this, the grains decreased in size. Reductions in the sizes of grains are a phenomenon that has not been seen before. Thus, it must firstly be considered if there were erroneous results, which can arise through the production of the film cross sections. This was initially conducted using FIB milling. This is a precise tool where flat cross sections are produced. Although, it was possible that microstructure smearing, as a consequence of the energetic milling ions, resulted in artefacts that affected the observations. However, grain and pore boundaries are relatively well resolved, hence smearing was not seen. Following this, the grain sizes were measured from images of cross sections that were produced from a fracture. This is a common technique used to produce relatively flat cross sections, as it is believed that the velocity of the crack that travels through the silicon substrate was great enough that the effects of the film microstructure did not impede the crack. A modified linear intercept technique was then used to measure the grain sizes, whereby from the images the areas of the grains were measured and then multiplied by the correction factor constant 1.56 which is normally applied when using the linear intercept technique to determine the grain sizes (Wurst and Nelson, 1972). This is a valid method as the grain sizes were compared between similar samples. Therefore, the measurements are considered to be a true artefact of the microstructures. A theory is presented that may explain the reduction in the observed grain sizes. The high density regions and large pores that were observed at 1 minute were no longer seen at 2 minutes of sintering. However, it was observed that there were constant densities of these films. So, it postulated that after 1 minute of sintering there was matter flow towards the large pores as there are lower free energies at these regions. This sintering matter is postulated to have originated from the large grains, resulting in grain size reductions. It is noted that this is a strange phenomenon and that further examinations are required. Investigations into the possible mechanisms that resulted in grain size reductions are presented in section 5.4. Additionally, in Chapter 6 there are further examinations of the grain size increases and decreases during sintering.

The sizes of the grains have a direct effect on the electrical properties observed. This is because the number of domains that can be accommodated within a grain is reliant on

the size the grain (Moulson and Herbert, 1989; Arlt, 1990). Tuttle *et al.* (1995) showed that in PZT films integrated with substrates that: in grains of sizes less than 0.1µm only single domains are accommodated; in grains of sizes between 0.2 to 1.0µm there are single 90˚ domain boundaries; and in grains of sizes greater than 1.0µm there are multiple domain boundaries. When single domains are accommodated within a grain there is a coupling of the grain-domain wall. This results in a clamping effect on the domains, and consequently the domain wall motion contribution to the dielectric and piezoelectric properties is low. Furthermore, tensile stresses arise in the x-y direction in constrained films, and as a result the domains will tend to align in the same direction as domain strains are minimised (Dorey and Whatmore, 2004b; Corkovic et al., 2008). At grain sizes between 0.2 to 1.0µm two domains per grain are assumed to exist. This has a direct effect on reductions in inter-domain strains if there is a ferroelastic domain boundary, and on grain-domain wall coupling, and thus domain re-orientation is increasingly probable. As a result of a domain boundary in a grain, domain wall motion between the neighbouring domains occurs. With the application of a low electric field during electrical measurements, which is not strong enough to pole a sample, there is displacement of the domain wall as the domains expand or shrink. This in-turn results in a contribution to the dielectric displacement and total strain, which is proportional to the displacement of the domain wall (Damjanovic, 1998). Domain wall contribution has been shown to have a direct effect on increases of the piezoelectric effect with increasing grains sizes (Demartin and Damjanovic, 1996). The extrinsic non-lattice contribution of domain wall motion can also have an effect on increases in relative permittivity during its measurement (Zhang et al., 1988). Furthermore, the relative permittivity increases with an increase in the number of domains in a given area, and thus with increases in grain sizes. Therefore, it is postulated that at 1 minute of sintering the observed grains accommodated a greater number of domains compared to the grains observed at any other sintering time. Thus, the peak in electrical properties occurred as a result of grain size increases. To further understand the spontaneous domain orientations in constrained PZT films the reader is directed to Chapter 7.

5.3.3 Region 1: Residual stress

It is known that during constrained sintering tensile stresses arise in-plane with the substrate which occurs because of the competition between the shrinkage of the film and the rigidity of the substrate (Dorey and Whatmore, 2004b). However, to fully understand the sintering that occurred in region 1 the changes in the residual stress in the x-y directions are examined. This is because the tensile stresses that arise in the films during sintering can result in de-sintering or cracking in the worst cases. Following this, compressive stresses can arise in the cooling stage due to thermal expansion mismatches. However, tensile residual stresses will develop which results in the unwanted ferroelastic switching of domains to the x-y directions. It is postulated that a minimisation of the degrading effects of stress at 1 minute of sintering could have been a major reason for the peak in the electrical properties. Residual stress was estimated using XRD measurements of the (002) peak at different sample tilt angles after sintering of the films (Ohno et al., 2008). This was in the form of a gradient which was determined from graphs of 2θ peak position vs. sample tilt. An example of this is displayed in Fig. 40.

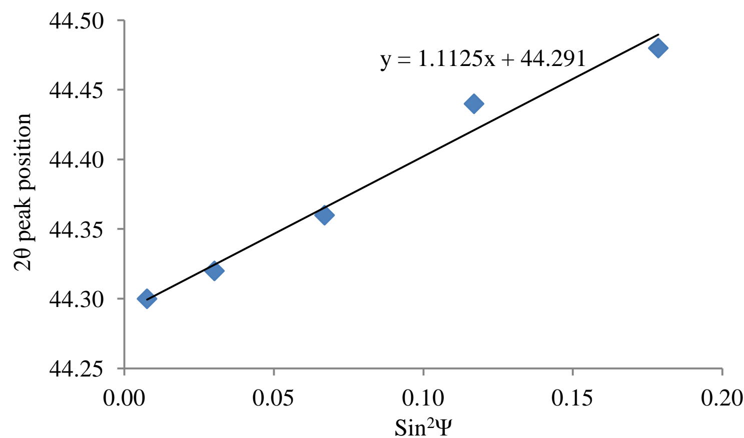

Fig. 40. XRD determined 2θ peak position as a function of sample tilt for an EGS film sintered for 5 minutes.

The reader is reminded of equation 8 from section 2.10.2. The residual stress thus can be estimated from the gradient in Fig. 40, but the Young's modulus and the Poisson's ratio of the film was not known. However, the gradient in Fig. 40 is related to the residual stress, as displayed in equation 13.

$$\partial(sin^2\Psi) = -\frac{\frac{E}{2(1+\upsilon)}.\cot\theta_0.\frac{\pi}{180}}{\sigma}.\partial(2\theta)$$ Equation 8

$$m = -\frac{\sigma}{\frac{E}{2(1+\upsilon)}.\cot\theta_0.\frac{\pi}{180}}$$ Equation 13

Where Ψ is the sample tilt, E is the Young's modulus of the film, υ is Poisson's ratio of the film, θ_0 is the Bragg angle position of an unstressed sample (PZT powder), σ is stress, 2θ is Bragg angle position of a stressed sample, and m is the gradient. The stress related gradient, m, is displayed as a function of sintering time in Fig. 41. It can be seen that there are positive gradients for all samples. This relates to a reduction in the crystal lattice spacing in-plane with the substrate, which occurred as a result of in-plane tensile stresses or strains (Ohno et al., 2008; Zheng et al., 2004; Zhou et al., 2003). This confirms the previous statements that tensile stresses arose in the x-y directions within these films.

Firstly, the residual stress of the EGS powder was examined to identify a stress free state. However, it can be seen that a positive gradient, and thus a residual tensile stress or possibly a strain in the x-y direction was measured. Stresses may have arisen as this powder was made from the sintering of EGS composite slurry, so there may have been a stress between the sintering sol and the powder which did not sinter. However, if a stress did arise this would occur uniformly throughout the powder, and in this XRD method essentially a difference in stress in the x-y directions compared to the z directions is measured. Thus, the stress exhibited by the powder suggests non-uniform stress. As this cannot be the case it is apparent that there were inherent errors in this method. Nonetheless the apparent stress of the powder was used as the baseline, so any increases in the slope can be considered due to tensile stresses. It can then be seen that the residual stress of the un-sintered film was the same as the powder. Stresses may arise during pyrolysation as a consequence of the shrinkage of the films as liquid and organics are removed which was identified in Chapter 4, this shrinkage is opposed by the rigidity of the substrate. It can be seen that in the early stages of region 1 there was

an increase in the slope. Subsequently, there are some variations towards the end of region 1 and through to region 2, but the general trend is that there is a plateau.

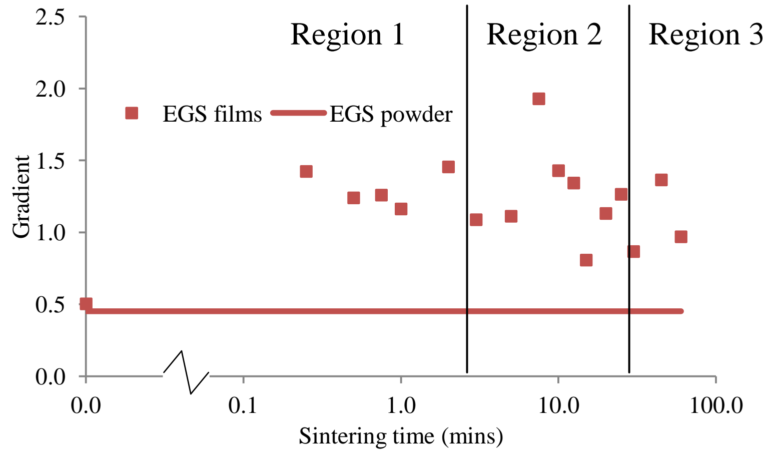

Fig. 41. Variations in the XRD determined gradients, proportional to the residual stress of the EGS films, as a function of sintering time at a processing temperature of 725˚C.

The initial increase in stress when sintering was applied can be explained by a crystallographic change and the action of sintering. At temperatures below 500ºC the CTE of the PZT film and the silicon substrate is well matched, although the CTE of the bottom electrodes is greater than both. As the sintering temperature increases there is a thermal expansion mismatch, but if the temperature was then reduced before a temperature where a crystal change or sintering occurs this stress would be relieved. However, the sol crystallises and forms a perovskite crystal structure at temperatures over 500˚C. The CTE of the PZT above this temperature is greater than that of silicon, so thermal strains in the film can arise (Dorey and Whatmore, 2004b; Corkovic et al., 2008). More significantly residual tensile stresses are exhibited by PZT films due to the action of densifying and non-densifying sintering which is opposed by the rigidity of the substrate and thus results in increases in the strain of the films, which is also proportional to the slope. Therefore, it appears likely that there is full crystallisation within 0.25 minutes of sintering, and that the film strain increases due to sintering. A subsequent plateau in the slope indicates that there is no change in the strain of the material with further sintering, possibly because sintering matter flow is restricted. However, if there is a slight reduction in the slope, then it is possible that matter

rearrangement occurred during sintering that resulted in relaxations in the x-y directions.

For the transitory peak in the electrical properties (Fig. 34 and Fig. 35) to be a function of stress it is likely that there had to be a significant decrease in residual stress at 1 minute. As this was not seen it is concluded that the film stress that was generated during sintering did not have a significant effect on the variation in the electrical properties at this stage. However, at longer sintering times there are similarities in the stress and electric property trends, so the effects of stress may have had an effect on the properties in region 2 and 3.

5.3.4 Region 1: Conclusions

It is concluded that in region 1 there was some densification in the z direction, albeit not considerable, and there was no densification in the x-y directions. Grain size increases occurred up to 1 minute of sintering, but were followed by grain size reductions. Furthermore, tensile stresses developed as a consequence of thermal expansion mismatches with the substrate and through the action of sintering. The strain of the film also increased due to sintering effects, but this may have been gradually relieved with longer sintering times.

It is concluded that the observed transitory peak in electrical properties occurred only due to the increases in the sizes of grains, which resulted in an increase in the number of domains in grains.

5.4 Effect of liquid phase sintering

It was shown in the previous section that significant microstructural redistribution occurred within region 1. This may have been a function of liquid phase sintering, so to evaluate this theory PZT films were processed without sintering aids (NS films). Firstly, the relative permittivity was measured for 5 samples per result and averaged with errors, and is displayed in Fig. 42. It can be seen that in the early stages of region 1 there is an increase in relative permittivity. This is similar to the increase in relative

permittivity of the EGS films, although at lower values. This is followed by a plateau in the remainder of region 1, which is clearly different to the observed relative permittivity of the EGS films. This could mean that the observed transitory peak in properties of the EGS films was a function of liquid phase sintering. This could also mean that the observed grain size increases, and reductions, were a function of liquid phase sintering. To further compare the EGS and NS films, d_{33} results are displayed in Fig. 43. There are decreases in d_{33} seen in region 1, which could indicate ineffective poling. However, in the absence of a transitory peak in relative permittivity it tends to confirm that a transitory peak was not present.

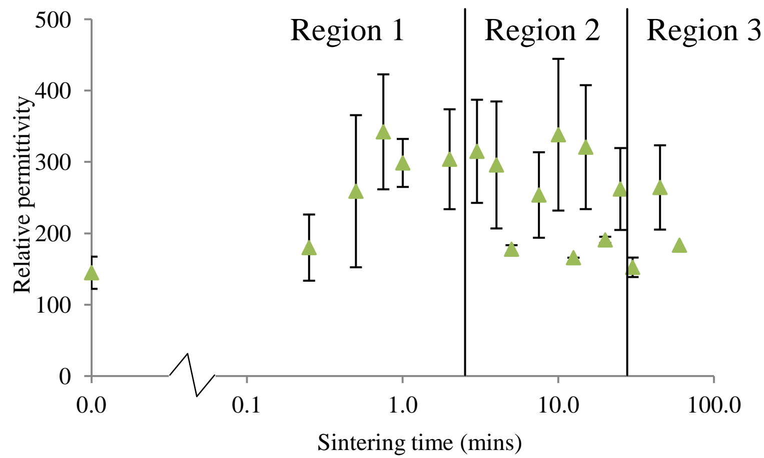

Fig. 42. Variations in relative permittivity and the associated standard deviation of the NS films as a function of sintering time at a processing temperature of 725˚C.

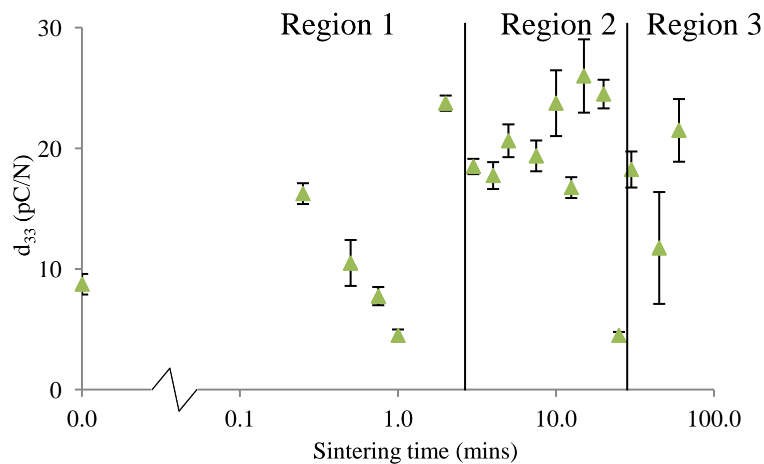

Fig. 43. Variations in d_{33} and the associated standard deviation of the NS films as a function of sintering time at a processing temperature of 725˚C.

It appears that similar microstructural redistribution that occurred in the EGS films was unlikely to have occurred in the NS films. To examine this hypothesis and identify the differences between liquid phase and solid state sintering, microstructure images of FIB milled cross sections are displayed in Fig. 44. There is a degree of microstructure smearing as a consequence of the etching process. However, it can be seen that there is little difference between the microstructures as the porosity and the size of the grains do not appear to change. This is confirmation that significant microstructural redistribution did not occur in region 1 with solid state sintering. This is also confirmation that the microstructural redistribution, and consequently the transitory peak in electrical properties observed for EGS films was a function of liquid phase sintering.

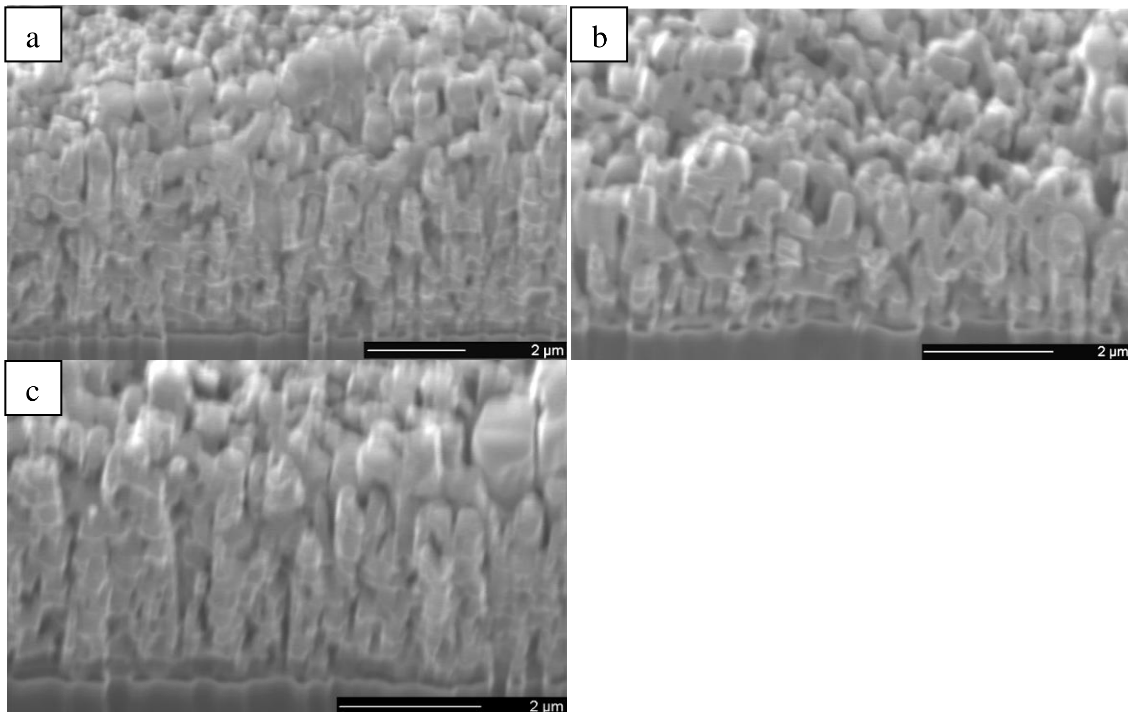

Fig. 44. SEM micrographs of FIB developed cross sections of the NS films sintered at 725˚C for a) 0 minutes, b) 1 minute, and c) 2 minutes, respectively.

To further inspect the processed films, loss results are displayed in Fig. 45. Constant high losses can be seen in region 1, along with a large standard deviation associated with these results which indicates that inconsistent dielectric responses occurred as a consequence of high losses. In comparison the EGS films exhibited much lower losses.

Thereby, it could be considered that there was better sintering of the EGS films, along with possibly lower porosities.

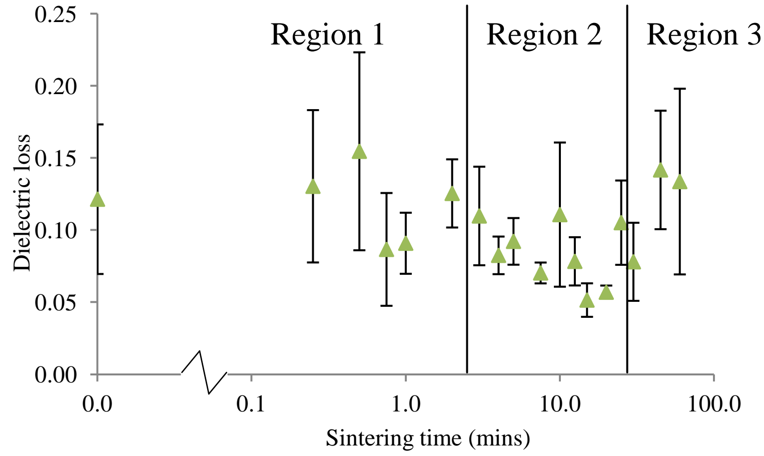

Fig. 45. Variations in dielectric loss and the associated standard deviation of the NS films as a function of sintering time at a processing temperature of 725˚C.

It has been confirmed that microstructural rearrangements and the subsequent increase and decreases in the sizes of the grains were a function of liquid phase sintering. Moreover, it can be assumed that higher sintering rates occurred in the EGS films as a consequence of liquid phase sintering. Thus, to further the understanding of the observed rearrangements in the EGS films, sintering aid theory is considered.

The sintering aids were added during ball milling, and due to the prolonged mixing it can be assumed that the sintering aids were uniformly distributed throughout the slurry. Furthermore, the EHDA deposition process resulted in uniform films, so again it can be assumed that the sintering aids were homogeneously distributed throughout the pyrolysed film. During sintering the films were held at 725˚C, which surpassed the melting point of the sintering aids (Corker et al., 2002). The early stages of liquid phase sintering have been described by Rahaman (1995). The liquid phase disperses rapidly due to the low viscosity of the liquid. The liquid travels towards and stays at the grain-pore boundary in the microstructure. Porosities within a microstructure lead to capillary stress gradients of the liquid, and results in liquid dispersion towards small pores before larger pores (Kwon and Yoon, 1981). Therefore, during early sintering of the EGS films more sintering is assumed to have occurred in general at smaller pores compared

to larger pores. This resulted in densification, which was indicated from shrinkage and loss results. The apparent increase in density at the localised regions resulted in an increase in the area of grain-grain contacts and as a consequence coalescence occurred, resulting in the larger grains which were seen at 1 minute of sintering (Rahaman, 1995; De Jonghe and Rahaman, 2003; Leite et al., 1996). However, it was shown that this development occurred independently of density changes, which was restricted probably due to a combination of grain growth, substrate constraints and the maximum z plane densities already achieved. It was also seen that larger pores opened up. Further redistributions then occurred in the latter stages of region 1, whereby it has been stated that redistribution of the liquid phase occurs towards regions of lower surface free energy (Shaw, 1986). In free sintering this results in a shift of sintering towards porous regions compared to dense regions. Consequently macroscopic densification occurs along with a tending towards microstructure uniformity (Kwon and Yoon, 1981). However, this may result in different effects in constrained sintering. It was seen in the EGS films that the microstructure at 1 minute of sintering exhibited highly dense regions, but also regions of large pores. Therefore, it is likely that the liquid phase redistributed away from the tightly packed granular regions. In-turn it is likely that there was a shift in sintering towards the grain-pore regions. However, it was suggested that there was no significant change in the macroscopic density after sintering for 2 minutes. So, it is possible that the redistribution of the liquid phase resulted in the flow of matter from the dense to the porous regions. As a consequence there may have been de-sintering at the dense regions, resulting in grain size reductions but microstructural uniformity.

In summary, the hypothesis presented indicates that non-uniform liquid phase sintering occurred initially that resulted in grain growth and a non-uniform microstructure. Due to the tendency of liquid phase redistribution that results in an increase in microstructural uniformity, and the densification constraints exhibited, there was a reduction in the area of grain-grain contacts and the sizes of the grains in the films. However, further testing is required to fully understand this process, but this was not conducted in this thesis.

5.5 EGS films: Region 2

In region 2 the relative permittivity and the d_{33} of the EGS films did not change significantly. This may be a consequence of constrained sintering. Examination of this hypothesis is firstly conducted through observations of micrographs, displayed in Fig. 46. There is no visible change in the porosity of the films as sintering times increased. There also appears to be no change in the sizes of the grains. If this is the case, then the lack of sintering is the cause for the electrical property plateau. Closer inspections of density, grains, and stress are presented to examine this theory.

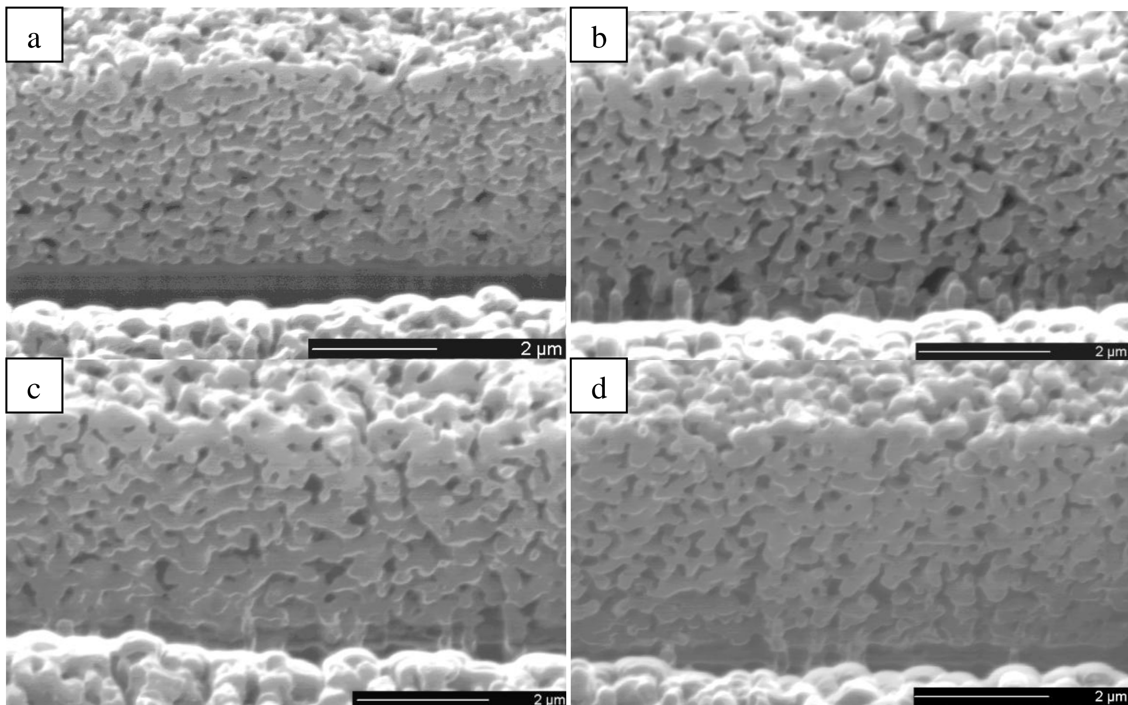

Fig. 46. SEM micrographs of FIB developed cross sections of the EGS films sintered at 725˚C for a) 3 minutes, b) 7.5 minutes, c) 15 minutes, and d) 20 minutes, respectively.

In Chapter 4 it was suggested that there was no significant change in density in region 2. It was theorised that this occurred because maximum achievable densities in the z direction had been obtained in region 1. Furthermore, in this chapter it has been shown that the loss is constant in region 2 (Fig. 37). If the previous assumptions that the porosity of the films is proportional to the loss are correct, then the shrinkage and loss results mostly agree that there was no change in the film densities. It can also be

assumed that there were no changes in the density in the x-y direction because of the restrictions that occur during constrained sintering (Dorey and Whatmore, 2004b). Therefore, from the observations of the electrical property results and the micrographs it is confirmed that there were no changes in the porosity of the films with the sintering times that were applied in region 2. Moreover, in Fig. 39 it is observed that there are constant grain sizes and the associated standard deviation in region 2. This confirms that grain growth did not occur. This may be a consequence of the reduction in the area of grain-grain contacts so coalescence and consequently grain growth was unlikely to have occurred. An alternative theory is that grain growth was also restricted as a direct consequence of substrate restrictions on matter flow. However, this would mean that non-densifying sintering mechanisms were constrained, which has previously been observed to be unconstrained (Cipitria et al., 2009). So, the reason for the restrictions on grain growth is not clear; but as it has been previously identified that the electrical properties are reliant on the sizes of the grains, it is likely that the plateau of the properties was a function of the restricted grain growth. Additionally, in Fig. 41 it can be seen that there is a plateau or possibly a slight reduction in the slope that relates to the film stress. Thus there was no increase in stress or strain as a consequence of the sintering in region 2. This indicates that there was no sintering in region 2, but possibly relaxations occurred.

In comparison there is also constant relative permittivity and d_{33} exhibited by the NS films in region 2. However, it appears that the relative permittivity of the NS films was slightly greater than that exhibited by the EGS films. Selected micrographs are presented in Fig. 47. Again it is difficult to examine because of the microstructure smearing, but it appears that there is no change in the porosity or the grain sizes. It is suggested that this was a result of similar constraints on sintering and the electrical properties as was seen with the EGS films. There were no shrinkage results to identify densification rates so loss results were used to indicate the evolution of the films. There was a plateau seen, which is likely to have occurred because there were no significant changes in the microstructure. However, the loss was greater than that exhibited by the EGS films. It is postulated that this occurred because of more pores present in films when sintering aids were not used. This is because at the grain-pore boundaries there is

an increase in the domain wall motion and increases in loss (He et al., 2004). Furthermore, the relative permittivity of the NS films was slightly greater than that exhibited by the EGS films. This also indicates that there was more domain wall motion in the NS films. However, there were large standard deviations associated with the relative permittivity of the NS films, probably a consequence of the high losses.

There are no direct measurements of the grain sizes, but it is evident from the observed micrographs, and the non-development of the electrical property results that grain growth did not occur. It is postulated that the similar relative permittivity exhibited by the NS and EGS films was therefore a consequence of small grains whereby it is likely that only single domains were accommodated. This is also evident from the grains sizes displayed in Fig. 39, as it can be seen that the grain sizes in region 2 were not much greater than that exhibited by the un-sintered film.

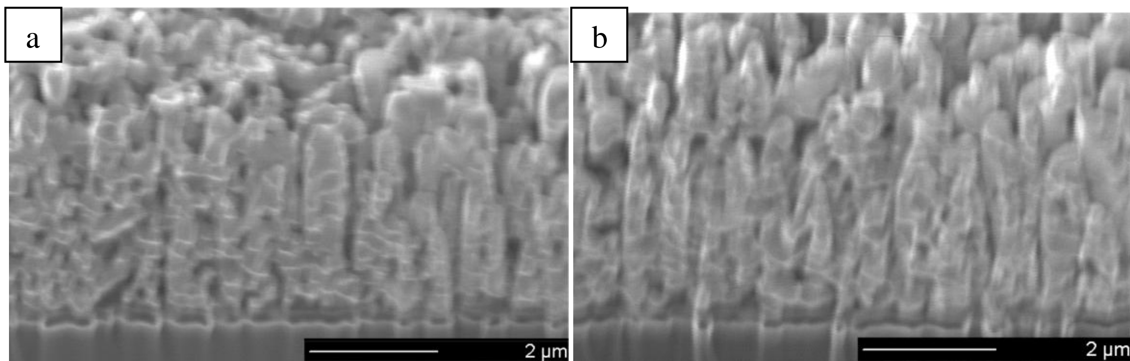

Fig. 47. SEM micrographs of FIB developed cross sections of the NS films sintered at 725˚C for a) 10 minutes, and b) 20 minutes, respectively.

In conclusion, all sintering mechanisms in all directions had essentially stopped in region 2. This occurred regardless of the use of sintering aids. It is concluded that this is a consequence of constrained sintering and indicates the challenges that arise in producing well sintered films when a substrate is integrated.

5.6 EGS films: Region 3

In region 3 the relative permittivity and d_{33} of the EGS films decreased, indicating that the films degraded with longer sintering times. However, the shrinkage results, loss, grain size and stress related slope was constant in region 3. Thus, the sintering restrictions continued, but this does not explain why there were degraded electrical properties observed. Micrographs are displayed in Fig. 48 to examine this. At 30 minutes of sintering the microstructure is similar to that seen in region 2. However, with longer sintering times there appears to be increases in the porosity; but this was not indicated in the shrinkage and loss. It is plausible that what is being seen is a consequence of material loss in the form of lead loss, which is commonly seen in the sintering of PZT. This occurs because lead evaporates due to the volatility at high temperatures or during prolonged sintering (Banerjee and Bose, 2004). A consequence of lead loss is the decrease in the electrical properties of a PZT sample as there is a decrease in the amount of active material. It also appears that the electrical properties of the NS films decreased, though there were large errors so this cannot be accurately stated.

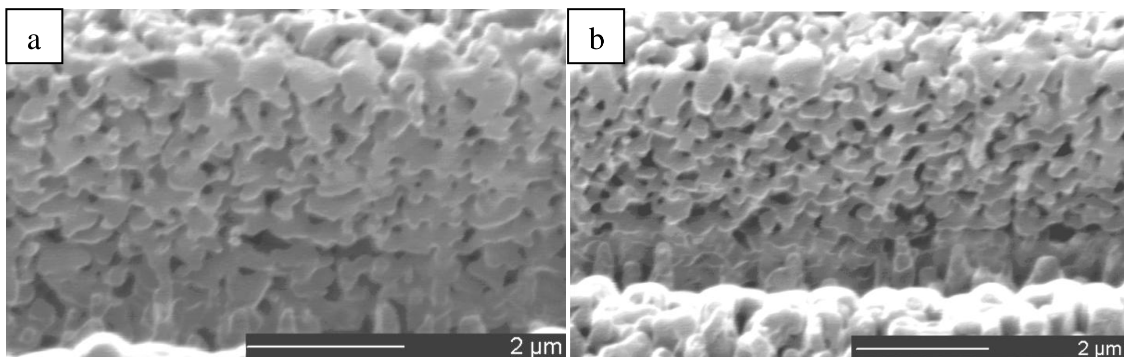

Fig. 48. SEM micrographs of FIB developed cross sections of the EGS films sintered at 725˚C for a) 30 minutes, and b) 60 minutes, respectively.

5.7 Constrained sintering of 2-ME films

It has been identified in this chapter that the best sintering conditions are found when 725°C for 1 minute is applied. However, this has only been found in one sample set.

The aim of this section was to gain a more general understanding of the constrained sintering effects. This was done by preparing 2-ME PZT thick films. The main differences between these and the EGS films were: the inclusion of hard dopants; spin coating deposition; and sol infiltrations to reduce pre-sintered porosities. Following this, the films were subjected to identical sintering conditions.

The analysis of these films was firstly conducted through electrical property measurements. The relative permittivity averaged across 5 samples is displayed in Fig. 49. For consistency, the three regions that were examined in the discussions of the EGS films are also examined in this section. In region 1, up to 2 minutes of sintering, there is a rapid increase in relative permittivity before a levelling off towards the end of the region. This is initially similar the trend that was found with the EGS films, but the relative permittivity is greater. However, there were significant decreases in the relative permittivity of the EGS films towards the end of region 1, which is not seen with the 2-ME films. In region 2, up to 30 minutes, the relative permittivity exhibited a plateau, which is similar to that found with the EGS films, albeit at higher values. Finally, at longer sintering times the relative permittivity decreases, which is also seen with the EGS films. There are clear similarities between the results, thus it is hypothesised that similar constrained sintering mechanisms occurred. However, there were differences observed at 2 minutes of sintering, and the values of the relative permittivity of the 2-ME films were greater. This could be due to the different film preparation processes, but closer inspections are required. Measurements of d_{33} are displayed in Fig. 50. In region 1 there are large increases culminating in an overall peak. This is similar to that seen with the EGS films but at higher values; and again the trends differ at 2 minutes of sintering as a decrease is not observed. Following this, there are gradual decreases throughout region 2 and region 3. This differs from that seen with the EGS films, where a plateau was exhibited. Furthermore, this differs from the relative permittivity trend of the 2-ME films. It is postulated that this can be explained by the hard-doping of the PZT crystal structure. Therefore, the analysis of the relative permittivity and d_{33} are discussed separately.

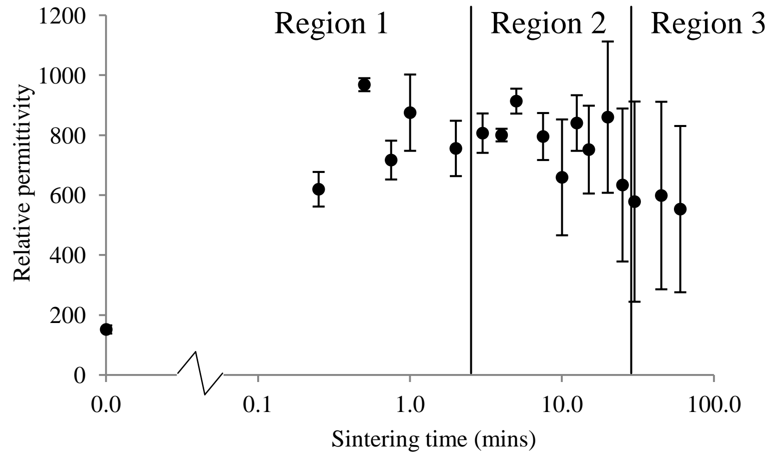

Fig. 49. Variations in relative permittivity and the associated standard deviation of the 2-ME films as a function of sintering time at a processing temperature of 725˚C.

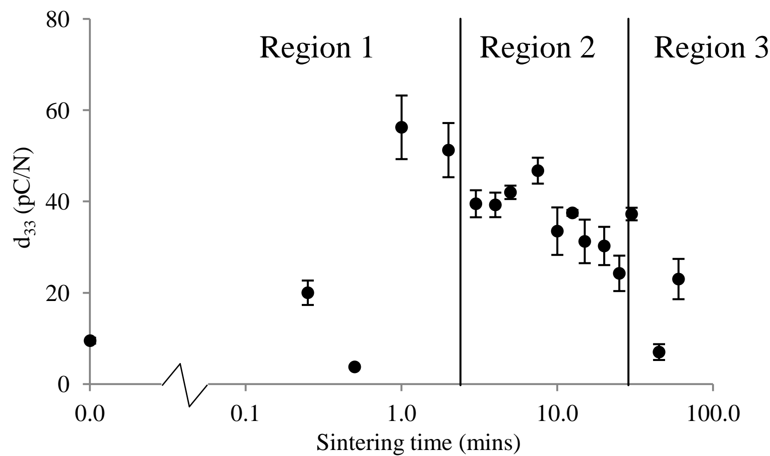

Fig. 50. Variations in d_{33} and the associated standard deviation of the 2-ME films as a function of sintering time at a processing temperature of 725˚C.

5.7.1 2-ME films: relative permittivity

In region 1 the relative permittivity rapidly increased. To understand why this occurred the micrographs are examined, displayed in Fig. 51. It can be seen that the porosities of all the films are low. This was due to the permeation of the sol during the infiltration stage, and the subsequent crystallisation of the material at porous regions. With increasing sintering times there appear to be no significant changes in the relative densities. This can be explained by the effects of constrained sintering, whereby it has previously been shown that densification in the x-y directions is restricted (Dorey and

Whatmore, 2004b). Furthermore, a consequence of the initial low porosities was low surface free energies. Therefore, the densifying sintering mechanisms would have been comparably lower than in the EGS films. However, the effect of the higher relative densities was likely to be a contributing factor to the comparably higher values of relative permittivity; but as previously concluded, densification was unlikely to be the cause for the increase in electrical properties in region 1.

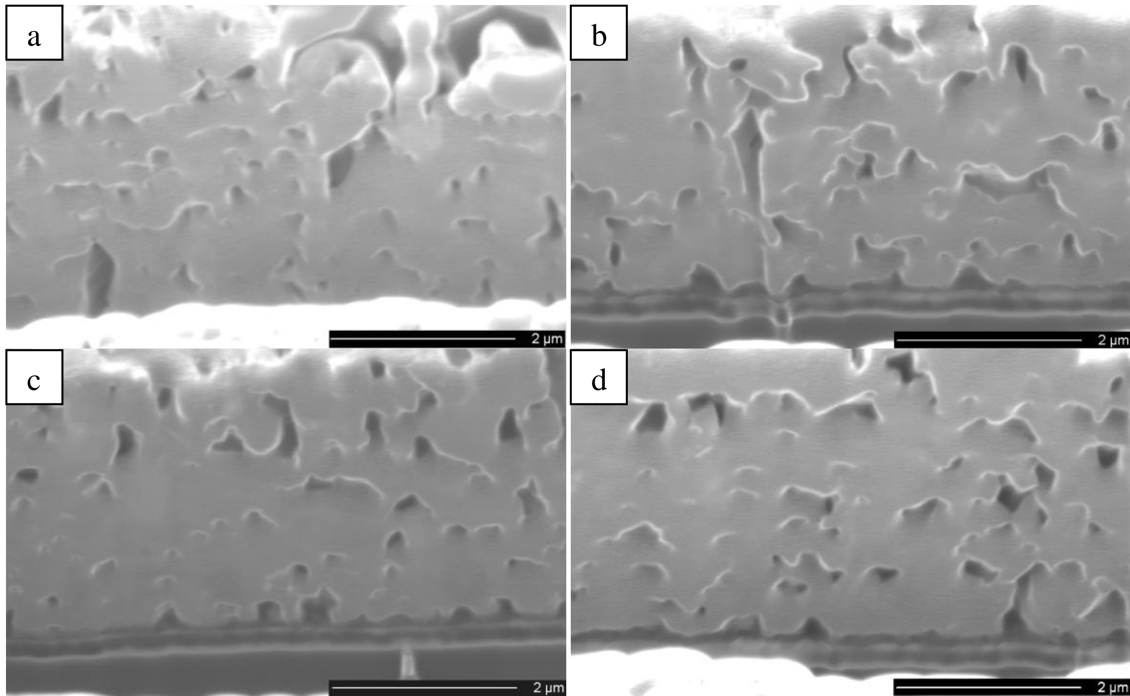

Fig. 51. SEM micrographs of FIB developed cross sections of the 2-ME films sintered at 725˚C for a) 0 minutes, b) 0.75 minutes, c) 1 minute, and d) 2 minutes, respectively.

The grain boundaries were difficult to identify in the micrographs, and images of cross sections using a higher resolution SEM were not conducted. However, it was concluded earlier that grain boundaries were not visible in FIB developed cross sections when there were tightly packed grains, and possibly also large grains. Thus, it is postulated that there were tightly packed grains and possibly large grains in all displayed 2-ME films. However, as the relative permittivity increased with longer sintering times in region 1 it is likely that the size of the grains increased. This is likely to occur through coalescence as a consequence of the tightly packed grains. The levelling off of the relative permittivity towards the end of region 1 could have occurred because grain

sizes no longer increased, which could have been due to a saturation of coalescence. However, with further grain size increases it is unlikely that there would be any change in the number of domains accommodated within a grain anyway. Thus it is possible that grain growth continued without affecting changes in the electrical properties. The comparably greater electrical properties found in the 2-ME films could also be explained by the grain growth mechanisms. It was found in the EGS films that non-uniform grain growth occurred, whereby there were some smaller grains which did not accommodate two domains. In the micrographs of the 2-ME films uniform microstructures are observed. So, it is likely that uniform grain growth occurred which would result in a comparably greater number of grains that accommodated two domains. However, the doping of the PZT structure must also be considered. The 2-ME films were hard-doped and as a consequence there is an increase in domain stability, which has been shown to result in higher dielectric properties (Damjanovic, 1998; Dorey and Whatmore, 2004a). A significant difference between the two sets of films is that major microstructural rearrangement was seen in the EGS films at 2 minutes of sintering, whereas similar rearrangement was not seen in the 2-ME films. Furthermore, it is evident from the micrographs and the relative permittivity results that grain size reductions did not take place in the 2-ME films. It is considered that the strange phenomenon was seen in the EGS films, and that normal grain growth mechanisms occurred in the 2-ME films.

In region 2 the relative permittivity exhibited a plateau. This was also exhibited by the EGS films albeit at lower values, which was postulated to occur because there were constant grain sizes. It is also noted that densification had also stopped. To examine if similar restrictions on sintering also took place in the 2-ME films micrographs are inspected, displayed in Fig. 52. There are high but apparent constant relative densities, suggesting that densification did not occur. Again it is difficult to identify grain sizes; however as there is no significant microstructural redistribution seen or changes in the relative permittivity it is likely that there were no significant changes in the sizes of the grains. Therefore, it is likely that there were similar sintering restrictions that were exhibited by the EGS films in region 2, and consequently there was no development of the electrical properties. Following this, during region 3 the relative permittivity

decreased. It is likely that this also occurred because of lead loss which was found with the EGS films.

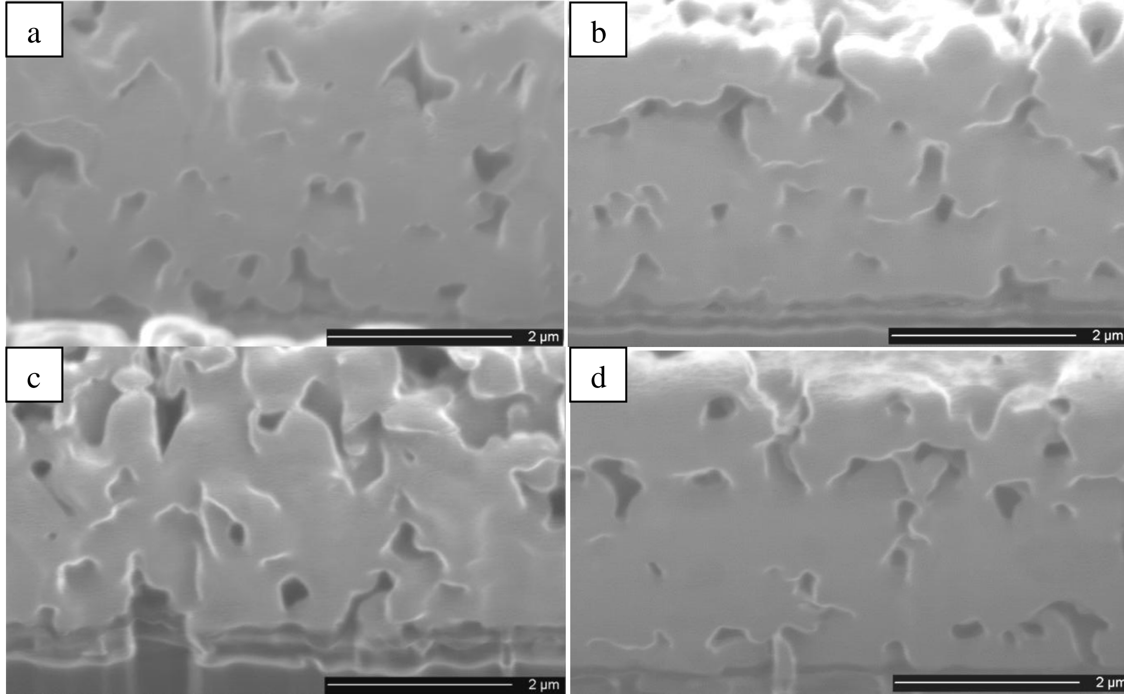

Fig. 52. SEM micrographs of FIB developed cross sections of the 2-ME films sintered at 725˚C for a) 5 minutes, b) 10 minutes, c) 25 minutes, and d) 30 minutes, respectively.

It is concluded that the relative permittivity of the 2-ME films increased with larger grains because of increases in the number of domains accommodated within the grains. It is possible however that grain growth continued with longer sintering times, but the relative permittivity did not change because there was no change in the number of domains accommodated within these grains. It is also concluded that the relative permittivity decreased in region 3 because of lead loss. It is also believed that there were no significant changes in the density of the 2-ME films.

5.7.2 2-ME films: d_{33}

The XRD tilting method was used to identify a slope from which residual stresses can be inferred, this is displayed in Fig. 53. It can be seen that the trend of the exhibited d_{33} in Fig. 50 and the slope in Fig. 53 are almost identical, but inverted. It is postulated that the variations in the stress had a direct effect on the d_{33} of the 2-ME films. The reason

for the changes in the slope is firstly examined. Direct comparisons between these results and that determined for the EGS films cannot be conducted. This is because the elastic properties of the films differ, meaning that the values of the gradients do not relate to the same residual stress. Firstly, it can be seen that the gradient of the powder is almost at zero. Thus, the powder is at a stress free state which is assumed to have occurred as a consequence of free sintering. The un-sintered film evidently exhibited a larger tensile stress than the powder. The stress was likely to have originated from the sol infiltrations. Upon pyrolysation the sol solidifies then crystallises at porous regions and the excess liquid evaporates. Consequently there is differential shrinkage of the sol and the ceramic layer, which results in localised tensile stresses (Dauchy and Dorey, 2007a). With sintering the slope decreases up to 1 minute of sintering. This is different to the trend seen in the EGS films, whereby stress increased as a consequence of a crystallographic change and subsequently thermal expansion mismatches. A crystallographic change is also assumed to have occurred in the 2-ME films, but there must be another effect during sintering which effected stress decreases. Following this, there are gradual and continuous increases in the remainder of region 1 and throughout region 2 and region 3.

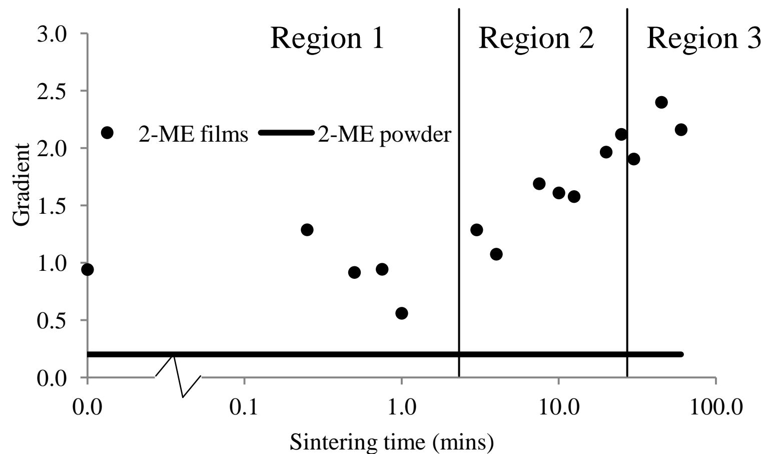

Fig. 53. Variations in the XRD determined gradients, proportional to the residual stress of the 2-ME films, as a function of sintering time at a processing temperature of 725˚C.

It is not immediately clear why the observed trend of the slope occurred, so the effects that can affect the slope are discussed. Stresses occur in sintering due to densification, phase transformations and thermal stress (Ohno et al., 2008; Zheng et al., 2004). It can

be assumed that all films are of the same phase and it is likely that the exhibited CTE of films is similar because the temperature at which the crystallographic change occurs was surpassed. This means that it is possible that the variations in the slope were a consequence of densification. If this is the case then the reduction in the slope in region 1 occurred as a consequence of relaxations in the x-y directions. Following this, the gradual increases in the slope occurred due to constant densification in the x-y directions. However, this clearly cannot be the case because densification in the x-y directions is restricted during constrained sintering (Dorey and Whatmore, 2004b). The slope is also proportional to the strain of the material. This could have increased during sintering with continuous grain neck growth so that the bonding becomes stiffer, which has been indicated to be unconstrained during constrained sintering (Cipitria et al., 2009). However, the reason for the reduction at 1 minute of sintering is still unclear, but is most likely due to stress relaxations.

If the slope indicates the strain of the material then the exhibited d_{33} of the 2-ME films was likely to be a consequence of the variations in the strain. Firstly, in region 1 there was an increase in d_{33}. This occurred as a consequence of larger grains and thus an increase in domains within the grains. In this way there is a reduction in domain pinning because of a reduction in grain-domain wall coupling. However, the crystal structure was hard-doped, so domain re-orientation was partially restricted anyway (Dorey et al., 2002). Furthermore, ferroelastic domain boundaries arise in the larger grains, consequently there is a reduction in inter-domain strains which can have an effect on a greater probability of 180º domain switching during poling. Throughout region 2 there were decreases in d_{33}, even though it was apparent that there were large grains in these films. It is postulated that these decreases occurred as a consequence of increases in the strain of the films in the x-y directions. This has an effect of an increasing number of domains orientated in this direction prior to poling as a consequence of the strains at the domain boundaries minimising. Furthermore, when the strain increases in the x-y directions there are greater inter-domain strains during poling when domains are switched to an orientation which is approximately perpendicular to the substrate. As a consequence, there is a greater probability that the domains relax back to the x-y directions after the poling field is removed (Dorey and

Whatmore, 2002; Dorey et al., 2007). In region 3 there were further decreases in d_{33}. It is also postulated that this was a consequence of increasing film strain. There was also the added effect of lead loss, whereby there was a reduction in the amount of active material.

5.8 Chapter conclusions

This chapter has fulfilled the aims set out; as the understanding of constrained sintering has been furthered and the evolution of the electrical properties of PZT thick films are better understood. This was examined using a 3 region model. As a result of the substrate inclusion, it is concluded that sintering densifying mechanisms are fully restricted in the x-y direction in all 3 regions. However, in region 1 of sintering there is densification in the z direction, but the most effective route to increase densities is through using the sol infiltration method. Most notably there is grain growth in region 1. This occurs as large areas of grain-grain contacts facilitate coalescence. However, in the EGS films this is followed by grain size reductions, which occur only with liquid phase sintering. This was postulated to occur due to a liquid phase re-distribution in a non-uniform microstructure, however this requires further examinations. This phenomenon is not seen in the 2-ME films. In region 2 it is concluded that no sintering occurs in EGS or the NS films, but grain neck growth continues in 2-ME films. Finally, in region 3 again no sintering occurs, but lead loss occurs resulting in a reduction in active material. Furthermore, tensile stresses arise in PZT thick films as a consequence of mismatches in the CTE with the substrate and strains that develop during sintering. It is concluded that this did not affect sintering, but manifested as a residual stress which did affect domain orientations.

It is concluded that to optimise the dielectric and piezoelectric properties of PZT thick films that the grain sizes should be greater than 0.2µm. This is because of an increase in the number of domains accommodated within a grain, which may result in a ferroelastic domain boundary and increases in domain wall motion that effects increases in dielectric properties. Furthermore, there is a reduction in inter-domain strains and grain-domain wall coupling. There is also the effect of film strains that result in

decreases in piezoelectric properties of hard-doped PZT. These optimised films were found to occur after 1 minute of sintering in two different PZT systems. Therefore, there is no requirement to sinter for longer than 1 minute. This discovery could affect the future sintering processes used with film technology.

Chapter 6

Rastering sintering of constrained PZT thick films

6.1 Introduction

In the previous chapter the highest values of dielectric and piezoelectric properties of PZT thick films were obtained at 1 minute of sintering. This work was conducted on small areas but real systems are much larger, so the aim of this chapter was to evaluate the sintering of large areas using the halogen bulb while obtaining high electrical properties. This was done by using a method called rastering sintering, whereby the halogen bulb was held in position and an EGS PZT film was passed through the sintering spot using a motorised stage. The diameter of the sintering spot was approximately 5mm but the exact size was not known, so the exact sintering times were not known. Investigations of the sintering conditions of the films were first conducted by monitoring the properties and microstructures of PZT films passed through the sintering spot in single line scans. Results were compared with findings in Chapter 5 in order to postulate a stage speed and sintering time relationship. Following this a rastering pattern was applied by using multiple parallel single line scans, and the effect of separations between parallel line scans was examined.

6.2 Effect of stage speed on the electrical properties

The relative permittivity of 5 samples per result as a function of stage speed of line scan sintered samples is displayed in Fig. 54. A three region model that was similarly applied in the examinations of relative permittivity in Chapter 5 is also applied here. Firstly, at the slowest stage speeds, which relates to the longest sintering times, the relative permittivity is initially low. This gradually increases as the stage speeds increase and thus the sintering times decrease. This culminates in high values of relative permittivity at mid-stage speeds, where there is a plateau seen. Finally, at the quick stage speeds over 0.20mm/s the relative permittivity gradually decreases. This region relates to the shortest sintering times. In the following measurements of d_{33} an almost identical trend of the three regions was observed (Fig. 54). The trend of the electrical properties is similar to that seen in Chapter 5 as there is an increase in the electrical properties as sintering time decreases, followed by the degradation of electrical properties. Thus, it is postulated that similar sintering mechanics occurred.

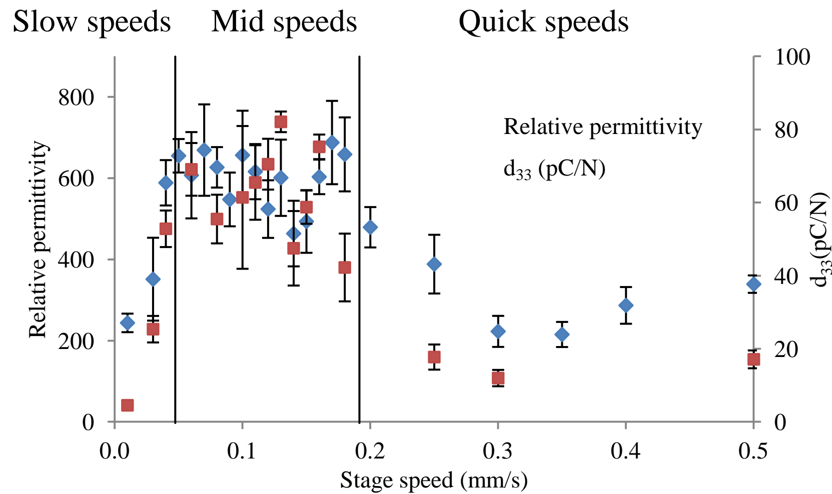

Fig. 54. Variations in relative permittivity and d_{33} and the associated standard deviation as a function of the applied stage speed at a processing temperature of 725˚C.

6.2.1 Slow speeds

The relative permittivity and d_{33} are initially low, but subsequently increase with quicker stage speeds (Fig. 54). In order to understand the reason for this trend, micrographs are examined in Fig. 55. At the slowest speed there are small grains and pores between grains. As the speed increases there is possibly a reduction in porosity as there is an increase in the areas of grain-grain contacts. It is however evident that the sizes of the grains increase as the stage speeds increase. This was quantified (using the modified linear intercept technique), and grain sizes are displayed in Fig. 56. The gradual increase in grain sizes as stage speeds increase can be seen. Therefore, as the sintering time of the films increase as the stage speeds decrease, it is concluded that there are reductions in the sizes of the grains as sintering times increase. This was also seen when spot sintering was used (Chapter 5), as grain size reductions after 1 minute of sintering was observed. This confirms that grain size reductions are not a measurement artefact but a newly discovered phenomenon. It was previously postulated that this occurred as a consequence of liquid phase re-distribution, it is however no clearer why this occurs.

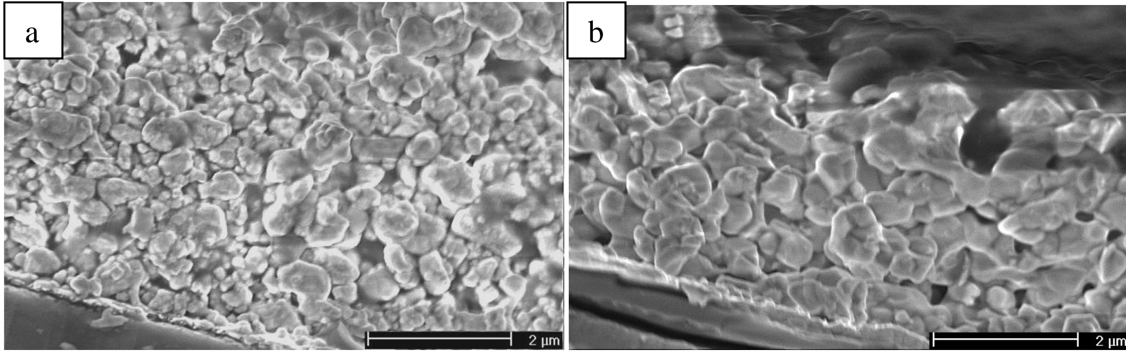

Fig. 55. SEM micrographs cross sections of films sintered at 725˚C at stage speeds of a) 0.01mm/s and b) 0.04mm/s, respectively.

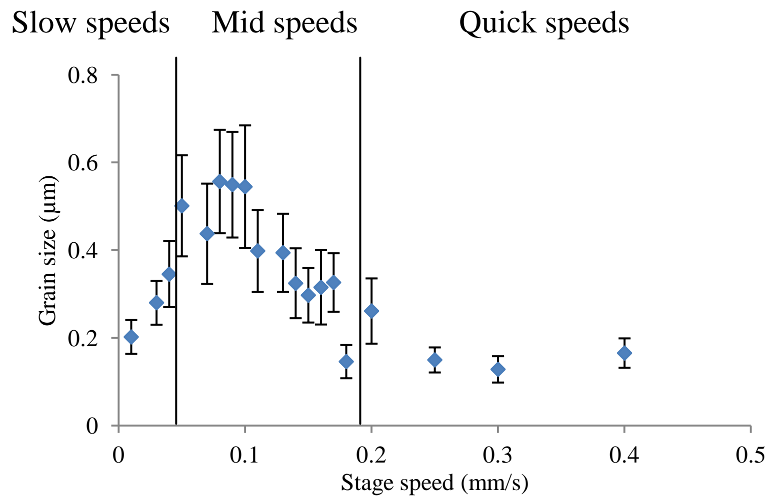

Fig. 56. Variations in the grain size and the associated standard deviation as a function of stage speed at a processing temperature of 725˚C.

It is evident from the examinations of the microstructures that the greater electrical properties that were observed at quicker stage speeds in this region were a result of larger grain sizes. This is concluded as this was also found in Chapter 5, and as the theory states that there is a direct correlation between larger grains and higher relative permittivity (Moulson and Herbert, 1989). The reader is reminded that Tuttle *et al.* (1995) found single domains accommodated in domains in grains smaller than 0.2µm, single 90˚ domain boundaries in grains between 0.2 to 1µm in size, and multiple 90˚ domain boundaries in grains greater in size than 1µm. Thus, it appears that at quicker stage speeds there were a greater number of domains accommodated within a grain, and consequently an increase in relative permittivity.

6.2.2 Mid speeds

In this region there are high values of electrical properties across a plateau (Fig. 54). This is examined as a function of the microstructures, which are displayed in Fig. 57. Compared to the microstructures seen at slow speeds there is an increase in the area of grain-grain contacts, and the pores that are visible are large in size. It is also evident that the sizes of the grains are greater. As the stage speeds quickened the grains are possibly smaller in size, but again there are large areas of grain-grain contacts seen. From the quantification of the grain sizes (Fig. 56) it can be seen that the sizes of the grains are large at mid speeds. However, it also appears that there is a peak in grain size towards the middle of this region, and slightly smaller grains with quicker stage speeds. As the film sintering times increased with slower stage speeds, this means that grain growth occurred at shorter sintering times, before a slowing of these rates. The grain growth mechanisms were postulated in Chapter 5 and it is believed that similar sintering conditions occurred using the line scan sintering method. This is whereby the increases in the area of grain-grain contacts facilitated coalescence via the migration of grain and liquid phase boundaries. The coalescence mechanism is also indicated from the standard deviation seen in Fig. 56. The standard deviation increases as the grain sizes increase, thus represents a greater range of grain sizes which is a consequence of some grains increasing in size and some not increasing in size. Following the region of grain growth, the sizes of the grains are constant at 0.05-0.10mm/, thus it appears that there was discontinuation coalescence.

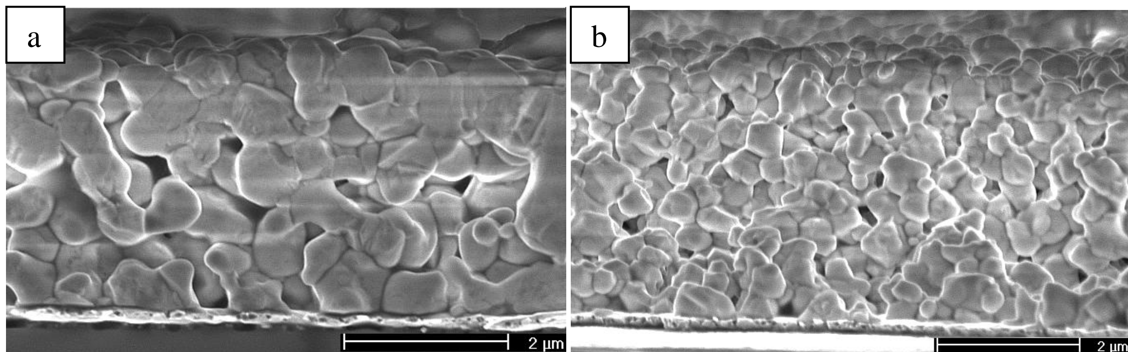

Fig. 57. SEM cross sections images of films sintered to 725˚C at stage speeds of a) 0.10mm/s, and b) 0.14mm/s, respectively.

The high values of the electrical properties were again a function of the large grain sizes. However, there were variations in the sizes of the grains, but not in the electrical properties in the mid stage speed region. This can be explained by the observations made by Tuttle *et al.* (1995). As stated, there are 90º domain boundaries in grains in a size range of 0.2 to 1µm. In the mid speed region all grains were within this range. Thus, there was no difference in the amount of domains accommodated in the grains between the different films, and consequently there were no changes in the electrical properties.

6.2.3 Quick speeds

Finally, at the quickest stage speeds the relative permittivity and d_{33} reduce. Micrographs of these films are displayed in Fig. 58. At the slowest speeds in this region there are large areas of grain-grain contacts, and the grains are large, although not as big as at mid speeds. At the quicker stage speeds the grains are much smaller, and there is a lower area contact between the grains as the porosity at these regions is greater. Thus, it is evident that at the quicker stage speeds, which relate to the shortest sintering times, the sintering time was not long enough to initiate considerable grain growth. As the speeds decreased and hence sintering times increased, there was more microstructural development as there was enough time for matter diffusion and consequently grain growth to occur.

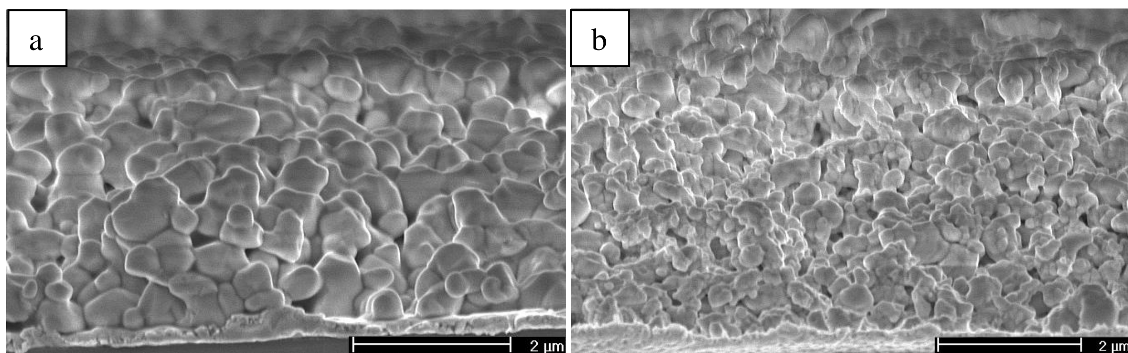

Fig. 58. SEM cross sections images of films sintered to 725˚C at stage speeds of a) 0.20mm/s, and b) 0.30mm/s, respectively.

The relationship between the microstructural development and the electrical properties is based upon grain growth. So at the slowest stage speeds in this region the grains

were relatively large, so the properties were high. However, as the stage speeds increased there were smaller grains and consequently the electrical properties were lower.

6.2.4 Conclusions

The aim of the single line scan sintering studies was fulfilled, whereby sintering conditions were found that resulted in high electrical properties. It is concluded that the sizes of the grains had a direct effect on the electrical properties. Furthermore, using comparisons with the findings in Chapter 5 a relationship between the stage speeds and the sintering times can now be postulated. It was found that at the shortest sintering times, quickest stage speeds, that there were initially small grains but grain growth then started to occur. This was similar to the microstructural development that occurred in region 1 up to 0.75 minutes of spot sintering (Chapter 5). When the sintering times increased, as the stage speeds were reduced in the mid stage speed region, grain growth continued resulting in large grains. Grain growth rates then reduced towards the middle of the mid stage speed region, but the grains were large at this point. Along with this the greatest electrical properties were found. This was similar to that observed in region 1 after 1 minute of spot sintering whereby the greatest grain sizes and electrical properties were found (Chapter 5). Finally, as the sintering times were further increased at the slower stage speeds the sizes of the grains reduced. This was also found at 2 minutes of spot sintering and longer, and thus at the end of region 1 and through region 2 (Chapter 5).

Therefore, it is concluded that the quick speeds related to sintering times of less than 0.75 minutes; the mid speeds to around 1 minute of sintering; and the slowest speeds related to 2 minutes of sintering and greater.

6.3 Comparison of spot and line scan sintering

It has been shown that similar grain sizes and electrical properties were found at 1 minute of spot sintering and at mid-stage speeds when considering the standard deviation errors. However, there were a greater number of samples where high

electrical properties were found while sintering using the line scan sintering method. This could have appeared because there were relatively large increments between each sintering time used in the spot sintered method, whereas there were small increments of stage speeds used in the line scan sintering method which related to small increments in the sintering time. Thus, it is postulated that a similar number of high property films as obtained in the line scan sintering method could be obtained using spot sintering, if a similar increment in sintering times were used. To examine this theory, firstly the sintering times that the line scan sintered films were subjected to are predicted. The predicted sintering times are displayed in Fig. 59. These predictions were made using two approaches: first sintering times were predicted by assuming an approximate sintering zone diameter of 5mm (noted as sintering spot diameter); and secondly in the previous section predictions were determined by comparing the properties and microstructures to that found in Chapter 5 (noted as microstructural comparisons). It can be seen that the two routes used to predict sintering times are generally in agreement, suggesting that these predictions are accurate. This also indicates that the approximation of the diameter of the sintering spot was appropriate.

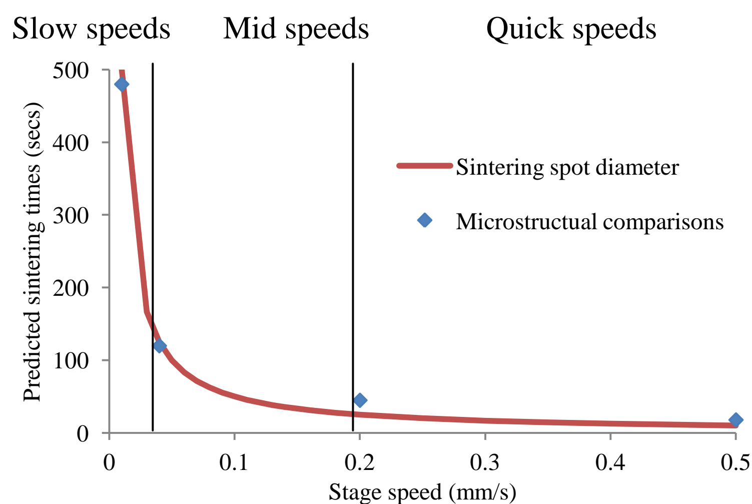

Fig. 59. Predicted sintering times determined through approximate spot size and comparisons with results in Chapter 5.

Comparisons of the sintering times for each of the 3 regions of material behaviour for spot and line scan sintering can now be conducted, and are displayed in Table 1. There are overlaps of the regions for line scan sintering because of the degree of uncertainty of

the sintering times. It can be seen that region 1 and quick stage speeds were at similar sintering times. However, grain growth occurred earlier in the sintering schedule when line scan sintering was used, thus the mid stage speed region started at an earlier sintering time than region 2. Furthermore, in comparison the mid stage speed region lasted for a longer period of time. Subsequently, grain size reductions in region 3 and at slow stage speeds occurred at similar sintering times. However, decreases in electrical properties of line scan sintered films occurred comparably later in the sintering schedule. This may have occurred if the sizes of the grains produced at shorter sintering times were larger in line scan sintered films, and subsequently the threshold grain size where single domains are accommodated within grains, when electrical properties reduce, occurred later in the sintering schedule. Alternatively, if it is proven that identical sintering occurred, this could just be an artefact of inaccurate sintering time predictions.

Table 1. Comparisons of the regions outlined for spot sintering and line scan sintering as a function of sintering time.

	Sintering time (seconds)	
	Spot sintering	Line scan sintering
Region 1/quick stage speeds	0-45	10-45
Region 2/mid stage speeds	45-120	27-125
Region 3/slow stage speeds	120+	120-500

To understand why the regions of the two sintering methods did not align completely, the differences between the two methods are examined. During spot sintering the bulb was focussed on a single area. The bulb was turned on and a region of approximately 5mm in diameter was heated. The sintering spot reached a maximum temperature of 725˚C within 10 seconds. Therefore, a rapid ramp rate was applied. When the sintering time was complete, the film was cooled to room temperature in air. All sintered regions which were evaluated were produced on one silicon wafer at a separation of 10mm. With the application of sintering of a neighbouring region, it was found in Chapter 4 that the heat transfer across the wafer resulted in temperatures in excess of 350˚C. So after the sintering and cooling of an evaluated region, it was then heated 3 or 4 more

times to temperatures greater than 350˚C depending on the number of neighbouring regions sintered.

During line scan sintering the bulb was turned on before the sintering spot was directed towards the film. The film was then moved through the sintering zone. In this way the edge of the film that was first exposed would have been heated almost instantaneously. However, the subsequent exposed regions were gradually heated. This is because there was heat conduction across the wafer which resulted in gradient heating before the sintering zone reached the material. Similar reductions in the temperature of a sintered region would have occurred as the sintering spot travelled away from the sintered region. Therefore, before sintering of a given area, a ramp rate occurred, and following sintering of a given area, a cooling rate occurred.

Due to the differences in the two methods in heating, it appears that there may have been a disparity between the effective sintering times. This is because the sintering times in the spot sintering method related to the time that the bulb was switched on and switched off, not the time the film was held at the isothermal temperature. As the films were heated from room temperature, the actual sintering time may have been less than that that was stated. This is because of the time taken for the full temperature to be reached which was believed to be less than 10 seconds, but as the apparent optimised sintering times were at such short times this could relate to a considerable amount of the apparent sintering time. This is compared to the line scan sintered films which were already at a high temperature before the film was exposed to the sintering zone. It is possible that these temperatures surpassed 680ºC when at a close proximity to the sintering zone, the point at which the sintering aids are activated. This could mean that the sintering times were longer than predicted. Therefore, it is assumed that sintering can take place comparably earlier in the schedule when using the line scan method because the film is already at a high temperature before it is exposed to the sintering zone exhibited by the bulb. This explains why grain growth occurs earlier in the line scan sintering schedule. Taking these into account, it is probable that region 2 and the mid stage speed regions actually took place at similar sintering times. This would also mean that it is probable that a similar number of high property films could be obtained

using spot sintering. However, there is a very short period of time in which high properties can be obtained, and as the increments between each sintering time in spot sintering was relatively large this range of high property films was probably missed. In conclusion, there are very similar sintering conditions that take place when using the spot and line scan sintering method. Consequently there were very similar resultant microstructures and properties obtained. However, it is concluded that to obtain the apparent optimised conditions the line scan sintering method is a more robust technique because there is a high level of control on sintering time, and removes the element of human error in the timing of the short sintering times which are present in the spot sintering method.

6.4 Effect of rastering sintering on the electrical properties

In this chapter it has been identified that a stage speed of 0.10mm/s provides sintering conditions where high electrical properties can be obtained. Therefore, this was applied in an automated rastering system of multiple parallel line scans in order to sinter large areas of PZT film on a silicon wafer. In this method the variable of the separation between each line scan is considered. It is postulated that to obtain the optimum overlap a separation of 5.0mm should be used because this was the approximate diameter of the sintering spot. However, separations of 1.0-7.0mm were used in order to identify the best sintering conditions achievable.

6.4.1 Electrical properties

The electrical properties were evaluated at over 20 regions per sample positioned randomly, and averaged. The relative permittivity of the films produced is displayed in Fig. 60. Firstly, it can be seen that the relative permittivities are low compared to those obtained using the line scan method at 0.10mm/s. These low values of relative permittivity are at a plateau. There is a possible small peak at a separation of 2.0mm, but it is such a low value that it isn't considered as a peak. A similar plateau of low values of d_{33} is also seen, which is displayed in Fig. 61.

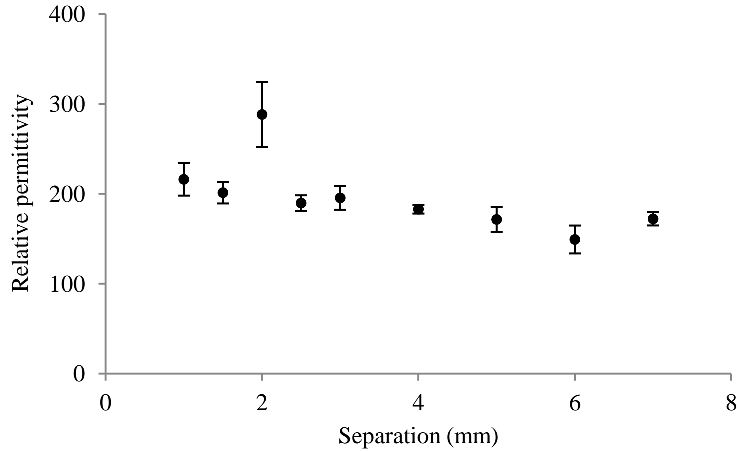

Fig. 60. Variations in relative permittivity and the associated standard deviation as a function of stage separation at a stage speed of 0.10mm/s and a processing temperature of 725˚C.

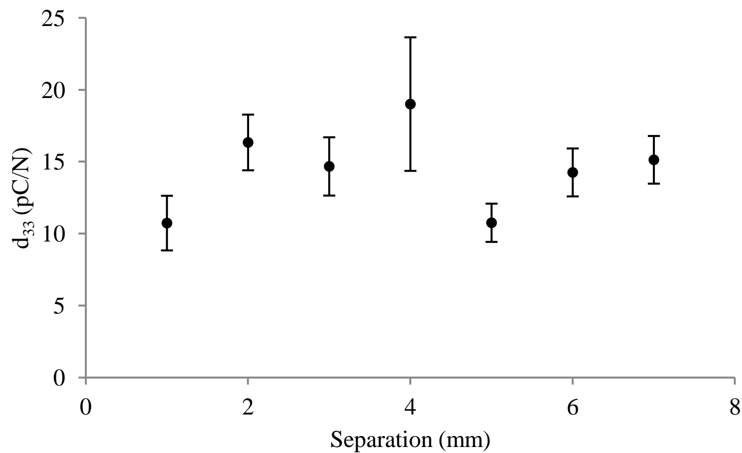

Fig. 61. Variations in d_{33} and the associated standard deviation as a function of stage separation at a stage speed of 0.10mm/s and a processing temperature of 725˚C.

To examine why low electrical properties are observed, micrographs are presented in Fig. 62. It appears apparent that at the smaller separations there was lower porosity. However, it can be seen that in all these images there were small grains in comparison with the grains seen at mid stage speeds with line scan sintering (Fig. 57). It has previously been observed that high electrical properties occur when microstructures exhibit large grains and large areas of grain-grain contacts. This was not observed using the rastering sintering method, confirming that the apparent optimised sintering conditions were not achieved.

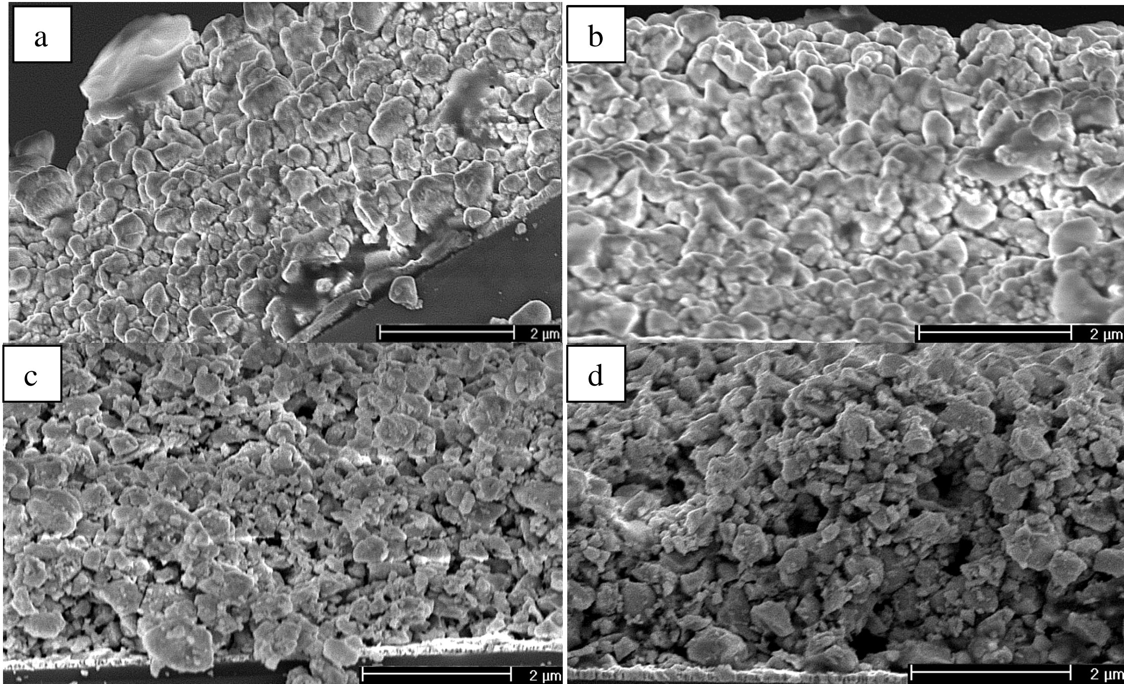

Fig. 62. SEM micrographs cross sections of films sintered at 725˚C using separations of a) 1.0mm, b) 2.0mm, c) 5.0mm, and d) 7.0mm respectively.

There is also the quantification of the sizes of the grains (using the modified linear intercept technique), displayed in Fig. 63. It can be seen that there is a plateau throughout at 0.16 to 0.18μm. Therefore, this confirms that low electrical property films were produced because of the occurrence of fine grains in these films, whereby single domains are accommodated due to grain sizes of less than 0.2μm (Tuttle B.A. et al., 1995). However, it is not known if small grain sizes are obtained as a consequence of under optimum sintering, or due to reductions in the sizes of the grains which occurs when over optimum sintering.

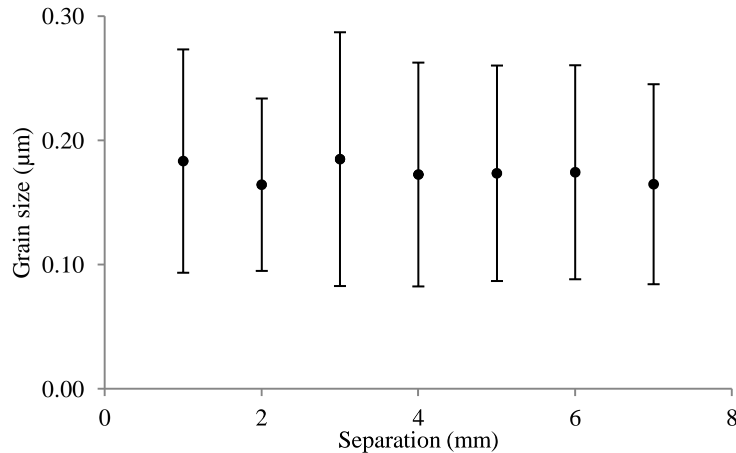

Fig. 63. Variations in the grains sizes and the associated standard deviation as a function of separation at a stage speed of 0.10mm/s and a processing temperature of 725˚C.

6.4.2 Sintering method analysis

To identify the reason why fine grained structures were found, it is useful to analyse the sintering technique. A schematic of a line scan sintered film is displayed in Fig. 64. The discrepancy in the sintering times at regions A, B and C are considered. The longest exposure time will be at the centre of the spot, A, and is gradually reduced at B and C. However, the diameter of the evaluated region was 2.0mm, whereas the width of the sintering spot was approximately 5mm. The sintering time at the centre of the evaluated region, at a speed of 0.10mm/s was approximately 50 seconds. Using trigonometry, the sintering time at the edge of the evaluated region was determined to be 45.8 seconds. Thus, there was reasonably uniform sintering across the evaluated region. This is assuming the sintering spot was parallel to the evaluated region.

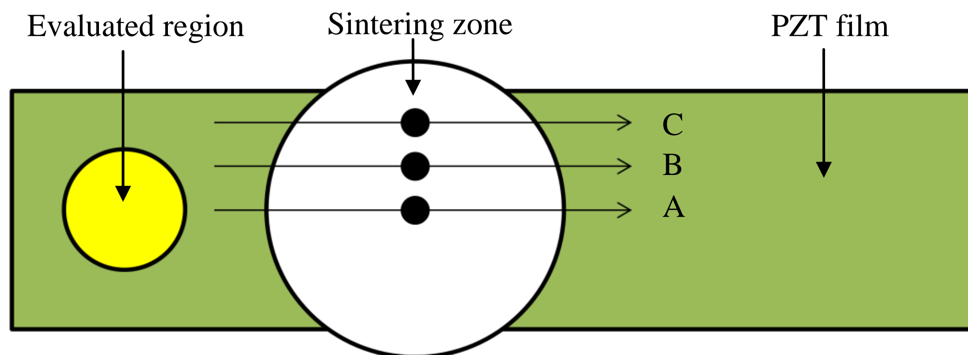

Fig. 64. Schematic of a line scan sintered film, with evaluations of sintering times at different regions.

The added effect of a separation in rastering sintering results in a more complex method. As a consequence of a sintering spot with an approximate diameter of 5mm, at separations lower than 1.75mm a region may be sintered four times by overlapping parallel line scans, as displayed in Fig. 65 A. At separations from 1.75 to 2.5mm a region may be sintered three times by overlapping line scans, displayed in Fig. 65 B. At separations from 2.5 to 5.0mm a region may be sintered twice, displayed in Fig. 65 C. At a separation of 5.0mm there is no overlap, displayed in Fig. 65 D, due to a circular sintering zone however, the regions near the edges of the line scans are hardly sintered. At separations greater than 5.0mm, regions between each parallel scan would not be exposed to the sintering zone, and thus would not be sintered, displayed in Fig. 65 E. In this way the regions exposed to the sintering zone would be sintered to apparent optimised conditions. However, in the rastering sintering method the regions that were evaluated were positioned randomly and the probability of evaluating a well sintered region is low.

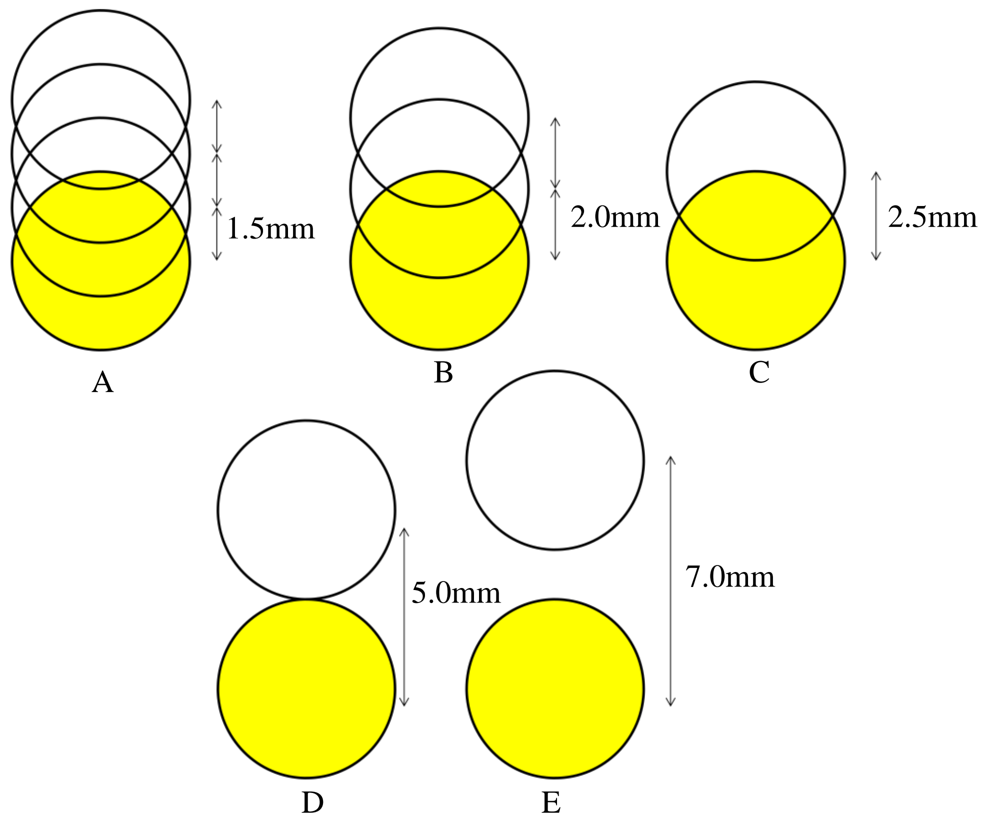

Fig. 65. Schematic of rastering sintering using a separation of a) 1.5mm, b) 2.0mm, c) 2.5mm, d) 5.0mm, and e) 7.0mm.

It is now useful to closer examine the sintering time within a given region. This is done by identifying the width of the first sintering spot, highlighted in Fig. 66, at a given position from the centre of the spot, x_n. This was done between +2.5mm and -2.5mm, at increments of 0.01mm. The width at each position was determined using the Pythagoras theorem. Following this, a parallel line scan at a given separation, s_n, was introduced, and the width of the sintering spot at x_n was again calculated. This was continued until there were no further parallel scans that overlapped the original spot. This was also done when there were 3 and 4 regions of overlap. The widths were determined using equation 14.

$$W_n = 2\ X\ \sqrt{(R_{ss}^2 - [s_n - x_n]^2)} \qquad \text{Equation 14}$$

Where W_n is the width of the sintering spot and R_{ss} is the radius of the sintering spot.

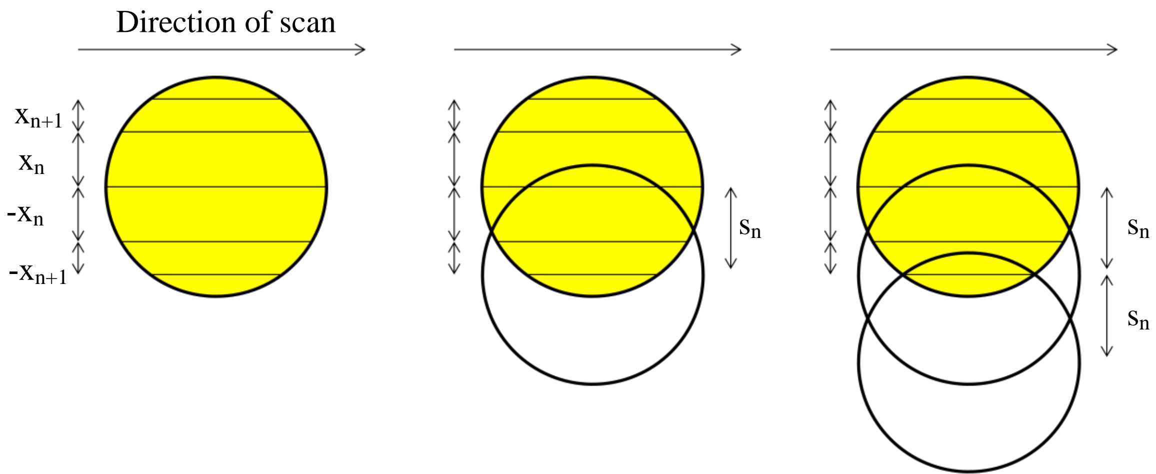

Fig. 66. Schematic used to determine sintering spot widths.

In the next step the sintering time was determined from the calculated widths and a stage speed of 0.10mm/s. As a consequence a profile of the sintering time across a region of -2.5mm and +2.5mm was determined. The sintering time determined at a line scan separation of 1.5mm is displayed in Fig. 67. It can be seen that there is a relatively consistent sintering time across the region. However, the combined sintering time is in excess of 125 seconds, which is beyond the point where grain size reductions have been

seen to occur. Therefore, it is concluded that the films which were sintered using a rastering separation of 1.5mm or less exhibited small grains because of over-sintering.

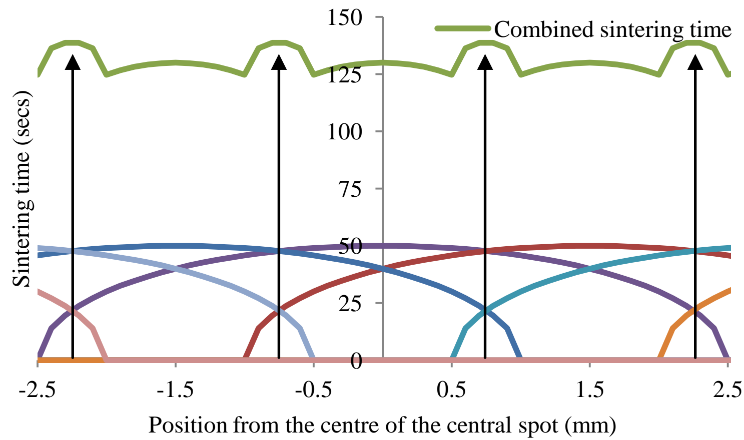

Fig. 67. Sintering time across a 5mm region using a stage speed of 0.10mm/s and a separation of 1.5mm.

In Fig. 68 the predicted sintering time with a separation of 2.0mm is displayed. It can be seen that there is again a relatively consistent sintering time across a given region. The sintering time is lower than that found when using a separation of 1.5mm, and may result in a sintering time before grain size reductions have been shown to occur. So it appears that apparent optimised conditions could be found using this separation. However, this was not seen in the examinations of the films processed using a rastering separation of 2.0mm. Thus, as the sintering time is near the upper limit of the optimised conditions, it is possible over-sintering still occurred.

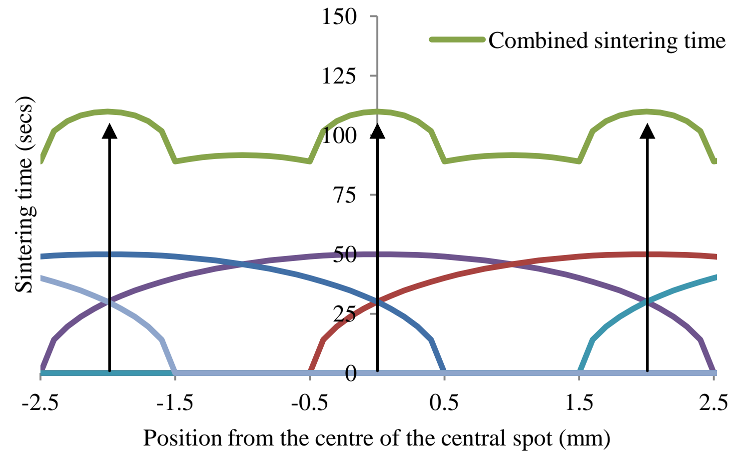

Fig. 68. Sintering time across a 5.0mm region using a stage speed of 0.10mm/s and a separation of 2.0mm.

In Fig. 69 the predicted sintering time with a separation of 2.5mm is displayed. It can be seen that there is an increase in the range of the sintering times. It is possible that the optimised sintering conditions may be found at this separation, but high functionality films were not found in the examinations. This may have occurred because of the inconsistency of the sintering across a region resulting in an evaluated region being of a graded functionality.

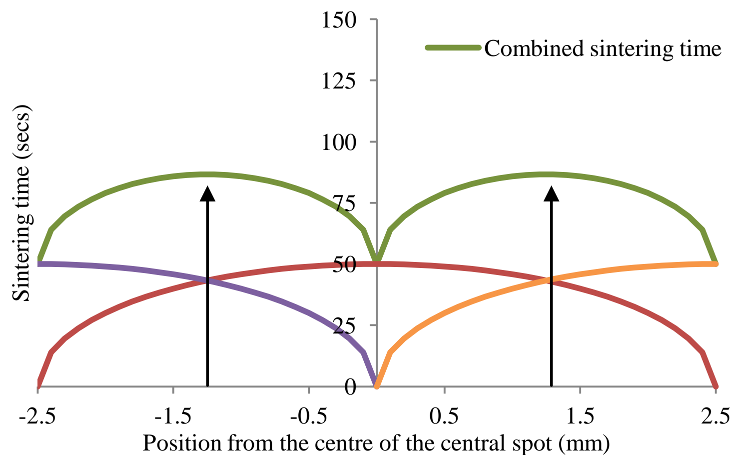

Fig. 69. Sintering time across a 5.0mm region using a stage speed of 0.10mm/s and a separation of 2.5mm.

In Fig. 70 the predicted sintering time with a separation of 3.5mm is displayed. It can be seen that the central region is essentially line scan sintered, and at the edges there is

an overlap of two parallel line scans. Compared to that seen at a separation of 2.5mm, the range of the sintering times reduces, but it is apparent that there would have been a difference in the sintering at the overlapped and non-overlapped regions. However, again the sintering times fall within the apparent optimised zone, but this was not found during the examinations of the films.

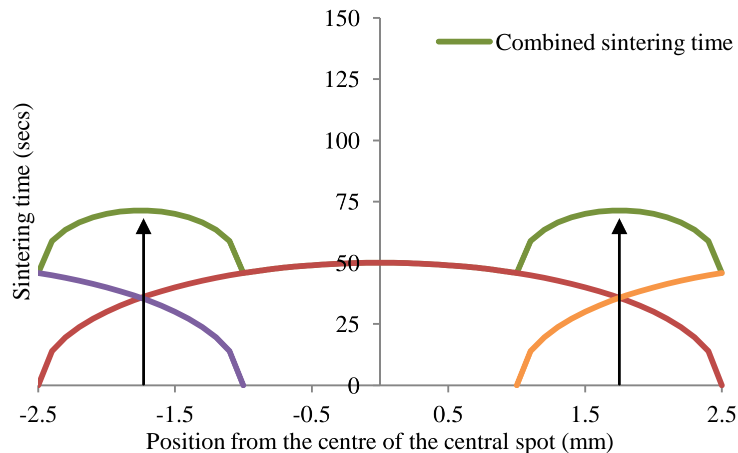

Fig. 70. Sintering time across a 5.0mm region using a stage speed of 0.10mm/s and a separation of 3.5mm.

From these results it is postulated that the best separation to use is around 2.0mm. This is because there was relatively consistent sintering across a given region with sintering times lower than 125 seconds which has previously been shown to result in large grains. However, it was also shown that apparent optimised sintering times occur at larger separations. These predictions are not consistent with the observations of the sintered films. This could be explained by an under-prediction of the sintering times that occurred, because the thermal conductivity across the wafer has not been considered. It was postulated that with line scan sintered films sintering occurred earlier in the schedule compared to the spot sintered films because a given region was already at a high temperature before exposure to the sintering zone. This effect would be more pronounced during rastering sintering, because of the long exposure time to the sintering zone resulting in the substrate being at a high temperature throughout the procedure. This means that a region could have been heated for a long period of time even though it was not directly exposed to the sintering zone, which could result in sintering occurring earlier in the schedule compared to films subjected to line scan

sintering, resulting in essentially longer comparable sintering times. It could also result in sintering of regions which were not exposed to the sintering zone if the temperatures were high enough. Therefore, it appears likely that the sintering times displayed were under- predicted.

So at a separation of 2.0mm, although consistent sintering appeared to have occurred, it is likely that sintering for longer than 125 seconds occurred. Thus, the slightly larger relative permittivity seen at this separation was likely to be a function of slightly larger grains as the process of grain size reductions was still occurring. At decreased separations grain size reductions had finished, resulting in a minimisation of the sizes of the grains. At a separation greater than 2.0mm there still should have been some regions that were sintered to the apparent optimum sintering times. However, due to the inconsistent sintering across a given region that was predicted, it was likely that the microstructures across a given region was graded and so the optimum sintered regions may not have been evaluated, but upon further inspection these regions may be found. Furthermore, there would be a graded functionality across an evaluated region which may have had the consequence of an overall degradation when the electrical properties were measured. Moreover, when evaluating the electrical properties for films sintered using a separation of 5.0mm and above, the potential high properties that may have been obtained at certain regions were not found, probably as a result of infrequent optimised regions and the random positioning of the electrodes.

6.4.3 Conclusions

The aim of this section to develop a fully automated sintering system in order to produce high property films was not fulfilled. This was because this method resulted in films that exhibited small grains. This occurred at a separation of 2.0mm or lower because these films were sintered for too long as a consequence of overlapping parallel line scans and high temperatures that resulted from thermal conductivity across the substrate. However, over the evaluated region there was consistent sintering. This did not occur at larger separations which was partially the reason for the exhibited low electrical properties. Therefore, in conclusion using a spot as a sintering zone in rastering sintering was unsuccessful because a balance of a consistent sintering time

across an evaluated region within the required optimised sintering times cannot be achieved.

6.5 Chapter conclusions

The aim of this chapter to produce large areas of PZT thick films with high electrical properties was partially fulfilled. During line scan sintering the thermal conductivity across the substrate was used as an advantage so that the time is reduced until the full sintering temperature is reached. In this way a robust technique was developed whereby large grains and high electrical properties can be repeatedly obtained because of the high degree of control on the sintering times. However, when this approach was used in rastering sintering this was not successful because undesirable sintering times or inconsistent sintering occurred. This was a function of having a spot as a sintering zone. However, these issues could be overcome if a square sintering zone was used. In this way a separation could be chosen so that there was no overlap or non-sintered regions. Moreover, a further effect that could be analysed is the temperature variant across the 5.0mm diameter sintering spot which could have had an effect on the sintering of the films.

In conclusion, the greatest electrical properties are found when the line scan sintering method is used. This could be applied in industrial processes to replace current sintering in furnace processes. This would result in a reduction in processing times and energy used during the sintering process. However, this does mean that possibly awkward beam shaped structures have to be manufactured prior to sintering.

Chapter 7

Stress induced domain switching

7.1 Introduction

In this project the highest dielectric and piezoelectric properties of the processed PZT films have been found at short sintering times. The electrical properties, however, are still inferior to that found with bulk materials. One major reason for this is the tensile stresses that arise as a consequence of constrained sintering. This was shown in Chapter 5 to occur mainly as a consequence of the action of film sintering which is opposed by the rigidity of the substrate. A result of these tensile stresses is domains orientated in-plane with the substrate. The domains can be re-orientated by poling the film; however it has been shown that a result of domain pinning is a reduction in the efficiency of poling (Dorey and Whatmore, 2002). An alternative method to inducing the re-orientation of domains is to apply a compressive stress parallel to the electrodes, which has been shown to result in an increase in domains orientated perpendicular to the electrodes, thus resulting in increased d_{33} responses (Jones et al., 2008; Lee et al., 2007; Kumazawa et al., 1998).

In this chapter the effect of a compressive stress on 2-ME PZT thick films is examined. The aim was to identify sintering and stress conditions that effects domain orientation so that high dielectric and piezoelectric properties can be obtained. This was done using a four point bend rig to apply an in-plane compressive stress to PZT films that had been sintered using the spot sintering method for 0-60 minutes at 725°C. The dielectric properties were measured while the stress was applied. The stress was maintained during room temperature poling, but the d_{33} coefficient was measured after the removal of the poling field and the stress.

7.2 Effect of a compressive stress on dielectric properties

The relative permittivity and loss of the unstressed PZT films were first measured. The films were then put under increasing compressive stresses and the properties were re-measured. Typical relative permittivity responses as a function of the applied stresses are displayed in Fig. 71. It can be seen that there is a linear relationship. The gradients of the linear fits were used to summarise the electrical properties of all processed

samples as a function of sintering time. The associated R^2 values indicated to the accuracy of the fit, and were used to determine error bars in the analysis.

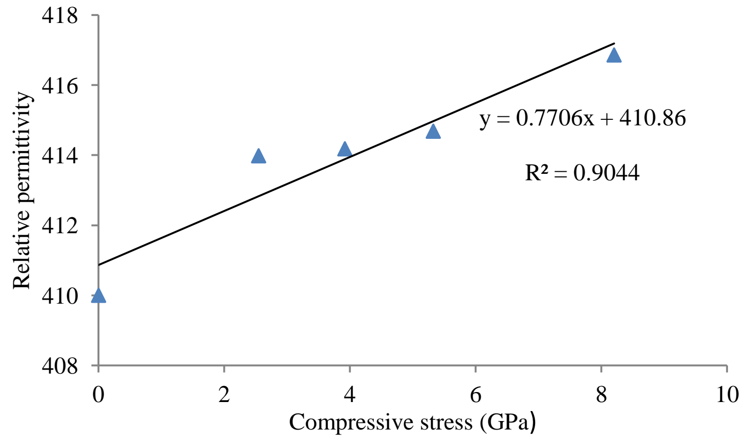

Fig. 71. Variations in relative permittivity of a 2-ME PZT thick film sintered for 7.5 minutes as a function of applied compressive stress.

The gradients of the linear fits of relative permittivity are displayed in Fig. 72. A three region model is considered as it has previously been shown that there are three regions of material behaviour as a function of sintering time. It can be seen that for most samples there are positive gradients, which relate to increasing relative permittivity with increasing compressive stress. In region 1 there are low values observed, except at 1 minute of sintering where there is an isolated negative gradient. This could be an erroneous result, but due to the previously discovered abnormal results found at 1 minute of sintering this will be examined. In region 2 it can be seen that there are increasing gradients, indicating that these films were more susceptible to the stress effects that result in relative permittivity increases. In region 3 there is a decrease in the slope resulting in negligible changes in relative permittivity.

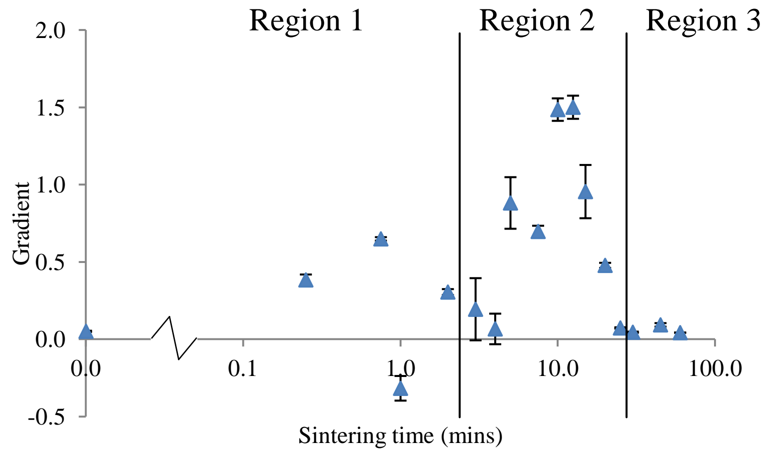

Fig. 72. Variations in the gradient of the linear fit of relative permittivity of 2-ME PZT thick films as a function of sintering time.

To put these result into context, displayed in Fig. 73 is the relative permittivity of the PZT films when unstressed and when a compressive stress of 8GPa was applied, which was near the maximum compressive stress applied. Along with this the difference in relative permittivity from an unstressed to a stressed system is displayed. Firstly, it can be seen that the relative permittivity when the films were unstressed is similar to that found with the 2-ME PZT films in Chapter 5. The change in relative permittivity when the compressive stress was applied is small. In comparison with the slopes seen in Fig. 72, region 1 is similar. In region 2 it is apparent that there is a plateau in the difference in relative permittivity, and again it can be seen that there are negligible changes in region 3.

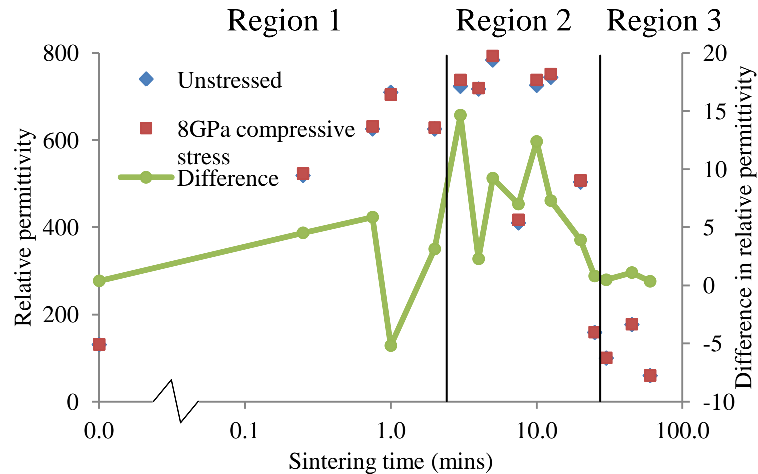

Fig. 73. Variations in relative permittivity of 2-ME PZT thick films unstressed, at a compressive stress of 8GPa, and the difference at these states as a function of sintering time.

The gradients of the linear fits of dielectric loss are displayed in Fig. 74. In region 1 and 2 there are constant gradients seen. These indicate that there was a constant increase in loss in region 1 and 2 with the application of a compressive stress. In region 3 there are negligible gradients, and thus changes in loss. The loss of the unstressed films and the loss after a compressive stress of 8GPa was applied, along with the difference between these are displayed in Fig. 75. It can be seen that there is a plateau in region 1 and 2 as the change in loss is small, but there is an increase in region 3.

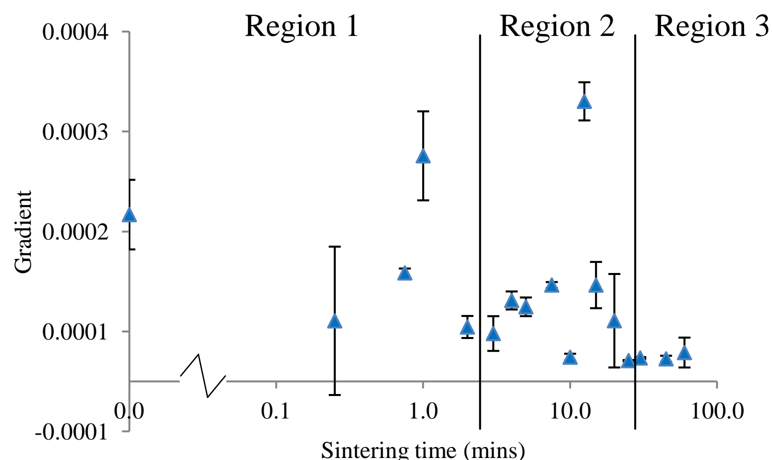

Fig. 74. Variations in the gradient of the linear fit of dielectric loss of 2-ME PZT thick films as a function of sintering time.

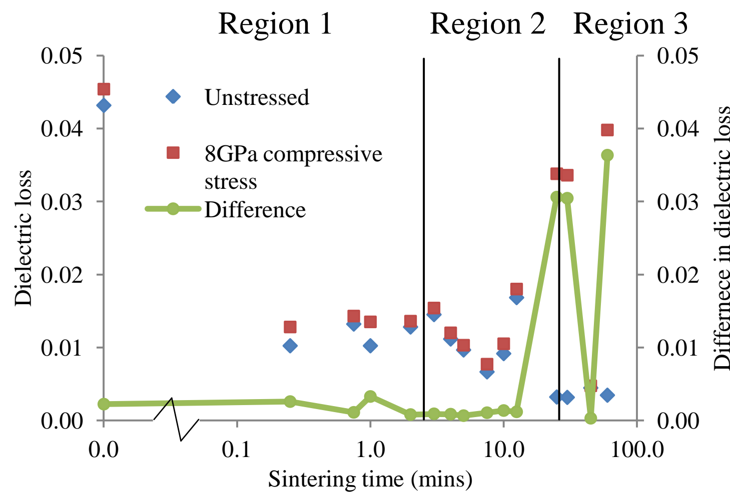

Fig. 75. Variations in dielectric loss of 2-ME PZT thick films unstressed, at a compressive stress of 8GPa, and the difference at these states as a function of sintering time.

7.3 Domain switching

It is apparent that the properties increased with a compressive stress, to examine why this occurred firstly the spontaneous domain orientations in the films after sintering is considered. Approximate domain formations within grains that accommodate two domains are displayed in Fig. 76. In Fig. 76 A and B there are ferroelectric boundaries between neighbouring domains which exhibit minimised electrostatic energies but not elastic energies. Domains may develop in this way in processed PZT films as a consequence of the tensile stresses that develop in the same direction. In Fig. 76 C, D and E there are ferroelastic domain boundaries which exhibit minimised electrostatic and elastic energies. Therefore, these domain orientations may spontaneously occur in the grains of the constrained sintered films, but the occurrence of the domain formation illustrated in Fig. 76 C is more likely to arise because the domains are in the same plane as the tensile stress. In Fig. 76 F the orientations of the domains are in the z direction with a ferroelectric domain boundary exhibited. In constrained sintered films this is very unlikely to spontaneously occur, but may develop during poling.

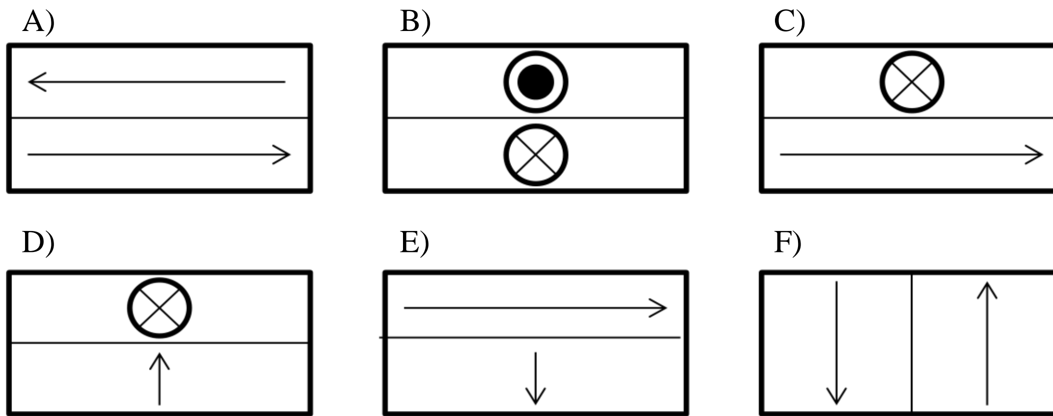

Fig. 76. Illustration of possible 180° domain orientations in the A) x direction, and B) y direction; 90° domain orientations in the C) x-y directions, D) x-z directions and E) y-z directions; and F) 180° domain orientations in the z direction.

The domain orientations exhibited by the PZT films has a marked effect on the dielectric properties. There are contributions to the dielectric properties from 90° domain wall vibrations, Δl, which is illustrated in Fig. 77. The domain walls may shift with an electric field or an elastic strain, which results in certain domains expanding and others shrinking. The displacement of the domain wall relies on the damping and force constants exhibited by the domain walls per unit area; and the magnitude of the external field or strain. The vibrations result in contributions to the dielectric displacement and total strain of the sample. Consequently, the domain wall vibrations contribute to increases in relative permittivity, dielectric loss, elastic compliance and piezoelectric coefficients. However, it has been stated that 180° domain walls do not contribute to the relative permittivity (Damjanovic, 1998).

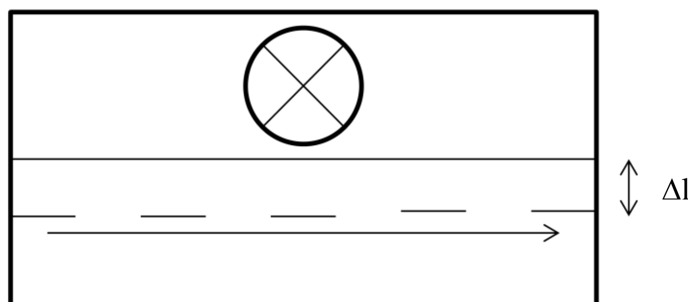

Fig. 77. Vibration, Δl, of a 90° domain boundary.

It is postulated that in the processed films domain orientations similar to that exhibited in Fig. 76 A, B and C switched to orientations similar to that illustrated in Fig. 76 D and E when the compressive stress was introduced. This is proposed because it is assumed that with the application of the compressive stress the domains tend to switch towards the z direction (Jones et al., 2008; Lee et al., 2007; Kumazawa et al., 1998). It is also probable that there was the occurrence of orientations similar to that illustrated in Fig. 76 F, as the effects of the compressive stress was probably enough to overcome the tensile stresses that arose during sintering. However, as the tensile stresses increased this domain switching would be increasingly restricted, resulting in orientations illustrated in Fig. 76 D and E being more probable. Secondly, it was observed that the relative permittivity increased with increasing compressive stress. This indicates that in some grains that accommodated 180° domain boundaries domain switching occurred resulting in 90° domain boundaries. As a result there is an increase in domain wall vibrations and consequently higher relative permittivity. Furthermore, it was observed that the loss increased with the application of the compressive stress. Loss increases also occur because of an increase in domain wall vibrations. Thus, it is evident that there was an increase in 90° domain boundaries with the application of a compressive stress. However, it is postulated that the domains were clamped in the switched z directions. This should result in reductions in the domain wall motion contribution to the relative permittivity, and loss should decrease as a consequence. It is postulated that this was not seen because the domain wall vibrations in grains which exhibit domain orientations similar to that illustrated in Fig. 76 D and E occur in the z direction (Fig. 77), but the compressive stress will only restrict the vibrations in the x and y directions.

The three regions of material behaviour can now be considered. In region 1 there was a small increase in relative permittivity and loss with the application of the compressive stress. It was shown in Chapter 5 that at the beginning of region 1 a significant portion of the grains only accommodate single domains. So it is postulated that the compressive stress effect on the dielectric properties is low because only in grains in which there are domain boundaries are domain wall vibrations enhanced. At 1 minute of sintering there was a decrease in relative permittivity with the application of the compressive stress. The grains within this film have been shown to mostly

accommodate two domains. However, it was shown in Chapter 5 that the strain was at a minimum after 1 minute of sintering. Thus, domain switching to the z direction with the application of the compressive stress would occur more readily as the domain clamping in-plane with the substrate is at a minimum. It is postulated that the small decrease in relative permittivity with the application of the compressive stress occurred because there was an increase in the number of grains that accommodated domain formations similar to that illustrated in Fig. 76 F. So as described, this will result in a decrease in the domain wall vibration contribution to the dielectric properties. In region 2 there was an increase in the slope as the relative permittivity increased with the application of the compressive stress. There was also a constant loss increase seen. Thus, both sets of results are in agreement that domain wall vibrations increased with the introduction of a compressive stress. It is assumed that most grains in these films accommodate at least two domains and that 90° domain switching occurred with the application of the compressive stress. However, in Chapter 5 it was shown that film strains increased in region 2. So it is increasingly unlikely that domain formations similar to that illustrated in Fig. 76 F developed. Thus, it is apparent that domain switching occurred within grains that resulted in an increase in 90° domain boundaries and consequently domain wall vibrations were enhanced resulting in the relative permittivity increases. In region 3 there are almost negligible increases in relative permittivity and loss with the stress. It has previously been shown that there was lead loss in region 3, thus it is likely that this is the dominant effect, meaning that the compressive stress had little effect.

7.4 Effect of a compressive stress on piezoelectric properties

The gradients of the linear fits related to d_{33} are displayed in Fig. 78. It can be seen that there are negative gradients exhibited by most samples. This is seen because there were gradual decreases in the d_{33} of the films as the compressive stress was increased. Furthermore, it can be seen that the observed trend was similar to that seen in Fig. 72, but inverted. In region 1 there are negligible gradients seen, indicating that the d_{33} responses were not significantly affected by the introduction of the compressive stress. However, at 0.75 and 1 minute of sintering there are low R^2 values and thus large error

bars, which occurred as a consequence of a poor linear fit. Considering these errors, it is possible that the d_{33} increases with a compressive stress. In region 2 there are increases in the gradients observed and in region 3 there are negligible changes in d_{33} seen when the stress was applied.

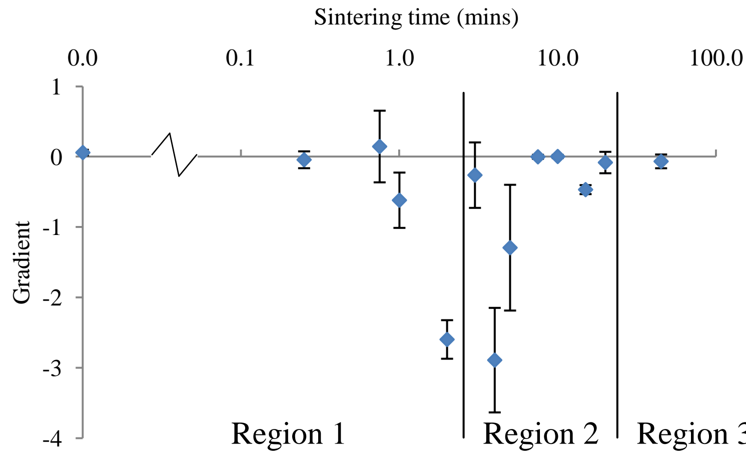

Fig. 78. Variations in the gradient of the linear fit of d_{33} of 2-ME PZT thick films as a function of sintering time.

To put these results into context, the values of the d_{33} measured are displayed in Fig. 79. In the unstressed system in region 1 there are low values of d_{33}, indicating that the poling of these samples was inefficient. Consequently, when the compressive stress was applied there are only small changes in d_{33} seen. The unstressed d_{33} then increases in the remainder of region 1 and region 2. It can be seen that there are large decreases in d_{33} when the compressive stress was introduced. In region 3 there are decreases in the d_{33} responses, and negligible changes when the compressive stress was applied.

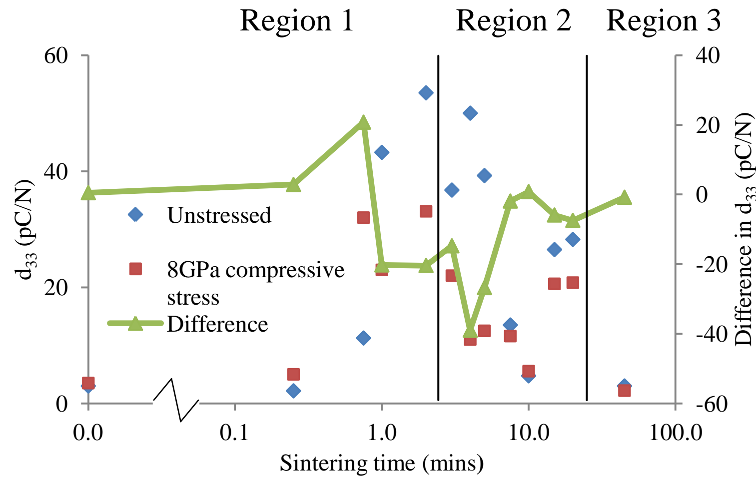

Fig. 79. Variations in d_{33} of 2-ME PZT thick films unstressed, at a compressive stress of 8GPa, and the difference at these states as a function of sintering time.

To understand why decreases in d_{33} were seen when the compressive stress was introduced the effect of poling is examined. The spontaneous domain orientations that arise in the films after sintering result in a non-polar material, and consequently a non-piezoelectric material. With the application of poling, domains may re-orientate aligned with the field resulting in a net polarisation. An illustration of the effect of poling that results in an originally non-polar set of domains exhibiting the piezoelectric effect as the domains are directed upwards in the z direction is displayed in Fig. 80. However, not all domains switch with a poling field because of the effect of domain boundary strains. It has been stated that a consequence of the tendency towards elastic strain minimisation at the domain boundary is the limited 90° switching but 180° switching can be almost complete (Moulson and Herbert, 1989). Therefore, it is likely that ferroelastic domain boundaries, as shown in Fig. 80 remain after poling. However, in the processed constrained films domain re-orientation is increasingly restricted as a result of tensile stresses that are in-plane with the substrate and grain-domain wall coupling (Dorey and Whatmore, 2002). Furthermore, the d_{33} response during measurement is dampened by the effect of the substrate (Damjanovic, 1998). Consequently, d_{33} similar to that found with bulk materials cannot be obtained.

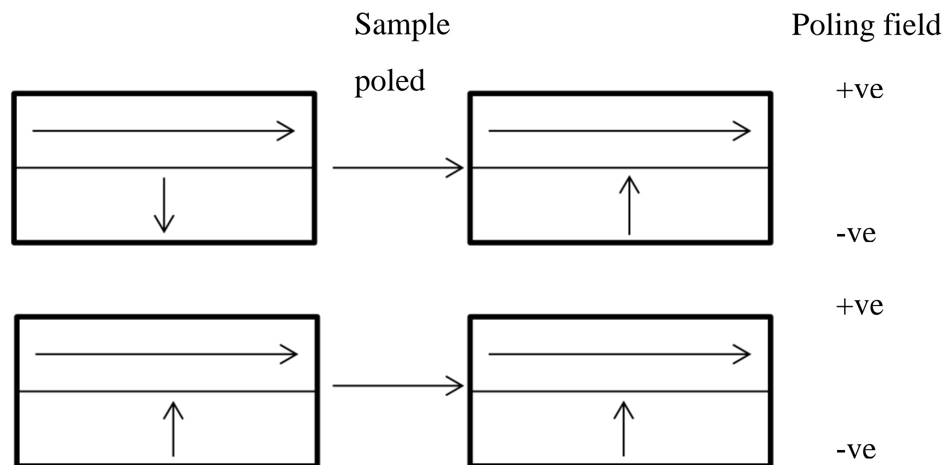

Fig. 80. Illustration of ferroelastic and ferroelectric domains re-orientated during poling.

The effect of poling when a compressive stress is introduced is now examined. It has been shown by Jones *et al.* (2008) that the application of poling with a compressive stress can result in domains switched to a plane perpendicular to the electrodes that exhibited non-180° spontaneous orientations. However, this occurred in bulk materials where grains accommodated multiple domains. Therefore, similar non-180° switching is unlikely to occur in constrained films. The effect of the compressive stress has been shown earlier in this chapter to result in domain switching to the z direction, and it is assumed that the domains are switched equally in the z direction facing up and down. The effect of the compressive stress is likely to result in the domains 'pinned' in these directions, so when the poling field is applied the domains in the 180° orientation are unlikely to switch. A schematic of the most likely result is displayed in Fig. 81, whereby domains that face down in the z direction, which would normally switch 180° under normal poling conditions, will be restricted in its motion. This is along with the restricted 90° domain switching due to domain boundary strain effects. Therefore a reduction in domains aligned in the z direction is exhibited when poling under a compressive stress, and consequently d_{33} reduces.

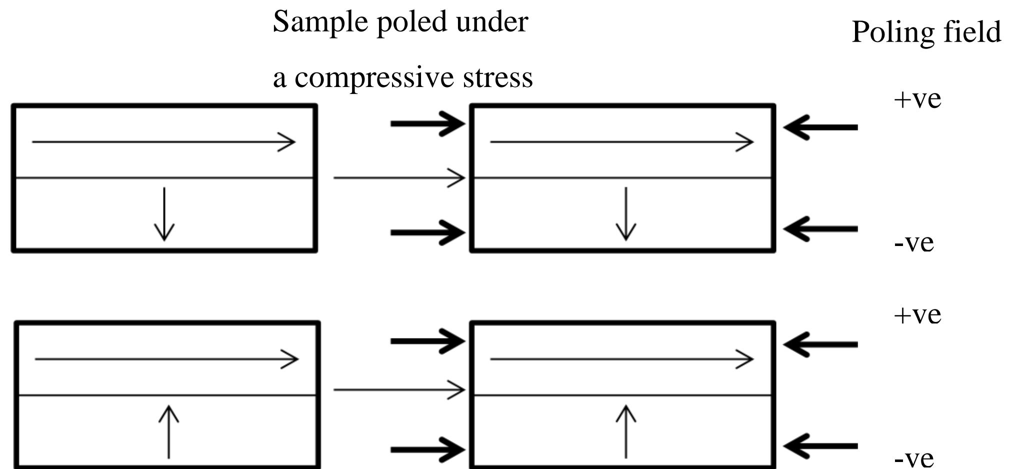

Fig. 81. Illustration of ferroelastic and ferroelectric domains re-orientated during poling and a compressive stress.

The three regions of material behaviour can now be considered. In region 1 the poling was not efficient, so there was initially a low d_{33} and thus low changes in d_{33} when the stress was applied. This is because there were mostly single domains accommodated within the grains in these films, and thus complete grain-domain wall coupling so the effect of poling and a compressive stress was not significant. Towards the end of region 1 and in region 2 there were large decreases in d_{33} when the stress was applied. In these films the grain sizes were large and it is assumed that most grains accommodated at least two domains. The decrease in d_{33} was believed to be due to the described clamping effect of the compressive stress, illustrated in Fig. 81. This resulted in an increase in oppositely orientated domains in the z direction, and thus a decrease in d_{33} compared to films under normal poling conditions. Finally, in region 3 there were low d_{33} responses as a consequence of lead loss, and thus only small changes with an applied stress.

7.5 Conclusions

The aim of this chapter was to increase dielectric and piezoelectric properties by applying a compressive stress. It was however found that dielectric properties only slightly increased, and piezoelectric properties decreased. It is concluded that a result of a compressive stress is an increase in domains orientated in the z direction, but there is

also an increase in domain ‘pinning’. An introduced compressive stress has been more effective in bulk materials because they exhibit larger grains and thus greater numbers of domains are accommodated, consequently domain re-orientation is more likely. Furthermore, a compressive stress has been shown to result in favourable domain switching in films when heating was also applied (Lee et al., 2007), which results in increased compliance of domain switching. Therefore, it is concluded that a compressive stress can be a useful tool in increasing the electrical properties of PZT films as 180º domain switching readily occurs. However, in the method presented in this chapter there were small grains and room temperature poling that resulted in increased levels of domain ‘pinning’ and consequently decreases in piezoelectric properties.

Chapter 8

Conclusions and future work

8.1 Introduction

The aim of this thesis was to develop a better understanding of the microstructural and stress development in PZT thick films during constrained sintering. It was theorised that this would allow the processing of films with superior dielectric and piezoelectric properties. To accomplish this aim, the evolution of shrinkage of constrained sintered films was investigated in Chapter 4. This was followed in Chapter 5 by the examination of the microstructural and stress evolution of the films. This led to a better understanding of the effects of constrained sintering on the dielectric and piezoelectric properties of PZT films. In Chapter 6 this work was expanded upon using a novel sintering method to sinter larger areas of the films. Finally, the effect of a compressive stress on the films was examined in Chapter 7. It was found that the sintering of PZT thick films under constrained sintering conditions resulted in three distinct regions of behaviour exhibited. In region 1 there were grain size increases and consequently increases in the electrical properties of the films. This was followed, in the EGS films, by reductions in the sizes of the grains and the electrical properties. In all processed films in region 2 sintering essentially stopped and consequently there were constant electrical property responses. In region 3 there was degradation observed as lead evaporation occurred. The findings in all chapters will now be linked using the 3 region model.

8.2 Evolution of PZT films under constrained sintering

8.2.1 Region 1

With the application of a sintering temperature the sintering aids melted resulting in a liquid phase that was assumed to initially flow towards the smaller pores. As a result a non-uniform microstructure developed with regions of tightly packed grains and also of large pores. Consequently, there was film shrinkage in the z direction, but it was assumed that there was no shrinkage in x-y directions because of the restrictions in these directions as a consequence of the effects of the integrated substrate. The best method found to gain high relative densities of constrained films is by infiltrating the ceramic with sol.

The large areas of grain-grain contacts at the regions of tightly packed grains facilitated coalescence through grain boundary migration, liquid boundary migration, and solution precipitation. As a consequence the average grain sizes within the films increased. More uniform grain growth was assumed to have occurred when sol infiltrations were used as there were larger areas of grain-grain contacts, and consequently coalescence occurred more uniformly across the microstructure. This is found when 1 minute sintering is applied using the spot sintering method. However, using the line scan sintering method where smaller time increments are used, this can be found between 27 to 125 seconds of sintering. It was concluded that sintering occurred slightly earlier in the schedule when using the line scan method as a consequence of the high degree of thermal conductivity across the substrate from the sintering zone, essentially pre-sintering a region. Grain growth did not occur to the same extent at these sintering times when sintering aids were not used. Furthermore, tensile stresses and strains arise as a consequence of the action of sintering of a constrained film. However, the 2-ME films exhibited a low residual stress at 1 minute of sintering, possibly because of a minimised strain.

Later in region 1 there were grain size reductions in the EGS films, which was confirmed to be a consequence of liquid phase sintering. This occurred when using the spot, line scan and rastering sintering methods. However, this did not occur in the 2-ME films. The grain size reductions are postulated to occur as a consequence of liquid phase redistributions in a non-uniform microstructure resulting in a flow of matter away from the dense regions. However, as this is a new phenomenon seen, this requires further examinations. The reader is referred to section 8.5 for the future work regarding this subject. It was also found that densification of the films had finished by the end of region 1, presumably because the maximum obtainable shrinkage in the z direction had been achieved.

8.2.2 Region 2

It is concluded that in region 2 for all processed films, sintering densifying matter flow had essentially stopped. This is also concluded for non-densifying matter flow, but it

was postulated that limited grain growth did occur in the 2-ME films. However, this did not result in any increases in the electrical properties as there was no change in the number of domains accommodated within grains. Furthermore, the strain exhibited by the 2-ME films increased in region 2, which had a direct effect on an increase in domain 'pinning', and consequently the piezoelectric properties of these films reduced. However, there was no variation in the stress or strain of the EGS films which occurred as a consequence of the restricted sintering.

8.2.3 Region 3

In region 3 it is concluded that again sintering matter flow does not occur. However, the most prominent effect found was that of lead loss which occurred as a consequence of increases in the volatility of the lead. This resulted in a decrease in active material within the films, thus the electrical properties decreased. As a result there was degradation of the films, and it was concluded that sintering times in region 3 must be avoided.

8.3 Effect of constrained sintering on electrical properties

The effects of constrained sintering result in tensile stresses in-plane with the substrate. As a consequence domains became orientated in this direction. There is also the effect of domain 'pinning' that originates from the clamping effect of the substrate and grain-domain wall coupling in smaller grains. Consequently it is difficult to obtain high electrical properties in PZT films. It was found that there were no changes in the electrical properties when densification occurred during sintering. The greatest electrical properties were found when films exhibited large grains. This was found to occur between 27 to 125 seconds of sintering using the line scan method, in which grains were in the size range of 0.2 to 1μm where two domains are accommodated within a grain (Tuttle B.A. et al., 1995). This resulted in the increase in the amount of domains in a given area, and thus an increase in electrical properties. Another effect on the electrical properties was the occurrence of ferroelastic domain boundaries within some grains. As a result the dielectric properties increased as there was an added contribution from 90° domain wall vibrations, which is not seen in single domain grains

or at 180° domain boundaries. It is believed that not all the grains accommodated ferroelastic domain boundaries however as it was indicated that there were increases in the amount of ferroelastic domain boundaries, and thus relative permittivity when a compressive stress was introduced. The piezoelectric properties also increased when the number of domains accommodated within grains increased. This occurred because there was a decrease in grain-domain wall coupling, and consequently a decrease in domain 'pinning'. However, with the application of a compressive stress during room temperature poling there is an increase in domains 'pinned' oppositely in the z direction, resulting in lower piezoelectric responses.

8.4 Conclusions

It is concluded that the optimised conditions during constrained sintering are to sinter for less than 2 minutes using the line scan sintering method, whereby there is a high control over the sintering time that is applied. This is concluded regardless of the use of sintering aids. In this way the maximum film densities and grain sizes greater than 0.2μm in size are obtained. This results in high electrical properties of constrained films as the grain sizes are large enough to accommodate ferroelastic domain boundaries. As a consequence there are increases in domain wall vibrations and reductions in domain pinning. However, additional sintering should not be applied as this leads to degradation of the films. These discoveries could be applied in industrial processes of the production of electroceramics integrated with rigid substrates. This can lead to increases in the functionality of the product, but also a reduction in production times and costs.

8.5 Future work

Future work that could possibly be a long term project is to examine the origin of stress at the film-substrate interface and the possibilities of reducing the level of stress in the film. In this procedure PZT thick films are to be manufactured in the same processes as presented in this thesis, and sintered in the same way. The cross section is then exposed using the fracture method. Using Raman spectroscopy the stress at the interface can be

determined. This is done first by determining a Raman spectrum of an unstressed system, for example PZT powder. The Raman spectra at the interface is then determined. A shift in the exhibited phonon frequency in comparison with the unstressed system indicates a residual stress, which can be accurately quantified (Ohno et al., 2008). Wang *et al.* (2007) used a similar process, whereby the laser of the Raman spectrometer was rastered across the material so that a stress map of the material could be determined and pasted over the optical image of the material. A similar method could be applied to the cross section of a processed PZT thick film so that stress at the interface can be mapped. In this way the origin of the stress in the films can be closely monitored as a function of sintering time, thus the processing method that results in the lowest stress can be examined. This method can also be scaled up so that the stress over the entire film is mapped. The investigations could be extended by introducing a stress modifying buffer layer between the substrate and film and re-measuring the stress at the interface. If the stress can be successfully reduced at the interface, the stress of the film may also reduce and as a consequence the effects of constrained sintering reduced. Tokumitsue *et al.* (1995) used $SrTiO_3$ buffer layers between a PZT film and a silicon substrate. This was predominantly to separate the volatile lead with the substrate. However, this buffer layer is crystalline and exhibits a lower CTE than that of a silicon substrate. Thus, using a $SrTiO_3$ buffer layer could result in a reduction in stresses in the PZT film. Another example of a buffer layer is that of $PbTiO_3$ used by Shimizu *et al.* (1994). However, it is possible that the stress that arises in crystalline buffers layers is transferred into the PZT film. An alternative route is to use a deformable layer. For instance, a porous silicon layer could be grown on a standard silicon substrate. The densification of the integrated PZT film would be less inhibited during sintering as the porous silicon layer would deform. To examine if these methods or different buffer layers has an effect on stress reductions, the aforementioned Raman spectroscopy method can be conducted at the interfaces.

There are also some short term investigations that could build upon the current work. In this project the greatest electrical properties of PZT thick films were found with the use of the 2-ME slurry, sol infiltrations and the application of line scan sintering. These were not utilised together however, thus superior electrical properties may be found if 2-

ME PZT thick films are line scan sintered. Furthermore, in Chapter 4 shrinkage was measured, but it was found that there were some issues with the accuracy of the work. So with the use of dilatometry a higher degree of shrinkage accuracy could be determined. However, the dilatometer would have to be robust so that the effect of evaporated lead would not damage the equipment.

A major restricting issue in the obtainable electrical properties found in this project was the effect of the substrate, where the consequences were tensile stresses and domain 'pinning' in the films. One route to reduce these effects which was partially examined was to use PZT as a substrate. In this way the thermal expansion of the film and the substrate is matched. In this method 90μm thick free-standing tape cast PZT were cut into disks and sintered at a temperature of 800°C. The EGS slurry was deposited on the PZT substrate using EHDA and sintered at a temperature of 725°C. However, it was found that the tape cast PZT curled at the edges, resulting in a deformed shape. Furthermore, the structure was very brittle and thus difficult to handle. For future work, these issues could be overcome if the densification of the PZT substrate is inhibited. Alternatively, fully sintered bulk PZT could be used, whereby the stability and strength of the material may be sufficient.

Finally, with the future work a better understanding of the mechanisms of the observed grain size reductions needs to be gained. It was confirmed in this thesis that this only occurred during liquid phase sintering. However, the theories presented did not fully explain the mechanics of grain size reductions, and it is important for future processing that this is better understood. One aspect of investigation would be to identify the exact positions of the liquid phase in the samples. A route to do this is by sintering films using the line scan sintering method so that there are small increments between the sintering times. The liquid phase within these films could then be mapped using high magnification TEM, so that a model of the liquid phase distributions with sintering time could be developed. Thus, the theory of liquid phase redistributions could then be confirmed or refuted.

References

Abreu Jr., A., Zanetti, S. M., Oliveira, M. A. S. and Thim, G. P. (2005), "Effect of urea on lead zirconatetitanate - Pb(Zr0.52Ti0.48)O3 - Nanopowders synthesized by the Pechini method", *Journal of the European Ceramic Society,* vol. 25, no. 5, pp. 743-748.

Arlt, G. (1990), "Twinning in ferroelectric and ferroelastic ceramics: stress relief", *Journal of Materials Science,* vol. 25, no. 6, pp. 2655-2666.

Banerjee, A. and Bose, S. (2004), "Free-standing lead zirconate titanate nanoparticles: Low-temperature synthesis and densification", *Chemistry of Materials,* vol. 16, no. 26, pp. 5610-5615.

Bardaine, A., Boy, P., Belleville, P., Acher, O. and Levassort, F. (2008), "Influence of powder preparation process on piezoelectric properties of PZT sol-gel composite thick films", *Journal of Sol-Gel Science and Technology,* vol. 48, no. 1-2, pp. 135-142.

Barrow, D. A., Petroff, T. E. and Sayer, M. (1995), "Thick ceramic coatings using a sol gel based ceramic-ceramic 0-3 composite", *Surface and Coatings Technology,* vol. 76-77, no. 1 -3 pt 1, pp. 113-118.

Bortolani, F. and Dorey, R. A. (2009), "Synthesis of spherical lead zirconate titanate (PZT) nanoparticles by electrohydrodynamic atomisation", *Advances in Applied Ceramics,* vol. 108, no. 6, pp. 332-337.

Cai, P. Z., Green, D. J. and Messing, G. L. (1997), "Constrained densification of alumina/zirconia hybrid laminates, I: Experimental observations of processing defects", *Journal of the American Ceramic Society,* vol. 80, no. 8, pp. 1929-1939.

Chao, X., Yang, Z., Chang, Y. and Dong, M. (2009), "Temperature dependence piezoelectric properties of low temperature sintered PZT-PFW-PMN ceramics with additive LiSbO3", *Journal of Alloys and Compounds,* vol. 477, no. 1-2, pp. 243-249.

Chen, B. -., Huang, C. -. and Wu, L. (2003), "Crack alleviation processing of lead zirconate titanate thin films deposited by sol-gel method", *Thin Solid Films,* vol. 441, no. 1-2, pp. 13-18.

Cipitria, A., Golosnoy, I. O. and Clyne, T. W. (2009), "A sintering model for plasma-sprayed zirconia thermal barrier coatings. Part II: Coatings bonded to a rigid substrate", *Acta Materialia,* vol. 57, no. 4, pp. 993-1003.

Cloupeau, M. and Prunet-Foch, B. (1994), "Electrohydrodynamic spraying functioning modes: a critical review", *Journal of Aerosol Science,* vol. 25, no. 6, pp. 1021-1036.

Corker, D. L., Zhang, Q., Whatmore, R. W. and Perrin, C. (2002), "PZT 'composite' ferroelectric thick films", *Journal of the European Ceramic Society,* vol. 22, no. 3, pp. 383-390.

Corkovic, S., Whatmore, R. W. and Zhang, Q. (2008), "Development of residual stress in sol-gel derived Pb (Zr,Ti) O3 films: An experimental study", *Journal of Applied Physics,* vol. 103, no. 8.

Damjanovic, D. (1998), "Ferroelectric, dielectric and piezoelectric properties of ferroelectric thin films and ceramics", *Reports on Progress in Physics,* vol. 61, no. 11, pp. 1267-1324.

Dauchy, F. (2007), "PZT Thick Film Development, Fabrication and Model of a 50MHz Thickness Mode Piezoelectric Ultrasonic Transducer", *Thesis (unpublished),* .

Dauchy, F. and Dorey, R. A. (2007a), "Patterned High Frequency Thick Film Mems Transducer", *Integrated Ferroelectrics,* vol. 90, no. 1, pp. 42-52.

Dauchy, F. and Dorey, R. A. (2007b), "Thickness mode high frequency MEMS piezoelectric micro ultrasound transducers", *Journal of Electroceramics,* vol. 19, no. 4, pp. 383-386.

De Jonghe, L. C. and Rahaman, M. N. (2003), "Handbook of Advanced Ceramics", .

Dean, J., Aldrich-Smith, G. and Clyne, T. W. (2011), "Use of nanoindentation to measure residual stresses in surface layers", *Acta Materialia,* vol. 59, no. 7, pp. 2749-2761.

Demartin, M. and Damjanovic, D. (1996), "Dependence of the direct piezoelectric effect in coarse and fine grain barium titanate ceramics on dynamic and static pressure", *Applied Physics Letters,* vol. 68, no. 21, pp. 3046-3048.

Dong, W., Lu, X., Cui, Y., Wang, J. and Liu, M. (2007), "Fabrication and characterization of microcantilever integrated with PZT thin film sensor and actuator", *Thin Solid Films,* vol. 515, no. 24 SPEC. ISS., pp. 8544-8548.

Dorey, R. A., Dauchy, F., Wang, D. and Berriet, R. (2007), "Fabrication and characterization of annular thickness mode piezoelectric micro ultrasonic transducers", *EEE Transactions on Ultrasonics, Ferroelectrics, and Frequency Control,* vol. 54, no. 12, pp. 2462-2468.

Dorey, R. A., Stringfellow, S. B. and Whatmore, R. W. (2002), "Effect of Sintering Aid and Repeated Sol Infiltrations on the Dielectric and Piezoelectric Properties of a Pzt Composite Thick Film", *J.Eur.Ceram.Soc,* vol. 22, no. 16, pp. 2921-2926.

Dorey, R. A. and Whatmore, R. W. (2002), "Apparent reduction in the value of the d33 piezoelectric coefficient in PZT thick films", *Integrated Ferroelectrics,* vol. 50, pp. 111-119.

Dorey, R. A. and Whatmore, R. W. (2004a), "Electrical Properties of High Density Pzt and Pmn-Pt/pzt Thick Films Produced using Comfi Technology", *J.Eur.Ceram.Soc,* vol. 24, no. 6, pp. 1091-1094.

Dorey, R. A. and Whatmore, R. W. (2004b), "Electroceramic Thick Film Fabrication for Mems", *Journal of Electroceramics,* vol. 12, no. 1/2, pp. 19-32.

Evans, D. R. and Craig, V. S. J. (2006), "Sensing cantilever beam bending by the optical lever technique and its application to surface stress", *Journal of Physical Chemistry B,* vol. 110, no. 11, pp. 5450-5461.

Garino, T. J. and Bowen, H. K. (1987), "Deposition and sintering of particle films on a rigid substrate.", *Journal of the American Ceramic Society,* vol. 70, no. 11, pp. c. 315-c. 317.

Garino, T. J. and Harrington, H. M. (1992), "Ferroelectric Thin Film II Symposia.", *MRS Symposia Proceedings No. 243 (Materials Research Society, Pittsburgh, PA),.,* , pp. 341.

Guillon, O., Weiler, L. and Rödel, J. (2007), "Anisotropic microstructural development during the constrained sintering of dip-coated alumina thin films", *Journal of the American Ceramic Society,* vol. 90, no. 5, pp. 1394-1400.

Gupta, T. K. (1972), "Possible correlation between density and grain size during sintering.", *Journal of the American Ceramic Society,* vol. 55, no. 5, pp. 276-277.

Haigh, R. D. and Whatmore, R. W. (2009), "On the processing conditions and interfacial chemistry of composite PZT thick films on platinised silicon substrates", *Sensors and Actuators, A: Physical,* vol. 151, no. 2, pp. 203-212.

He, X. -., Ding, A. -., Zheng, X. -., Qiu, P. -. and Luo, W. -. (2003), "Preparation of PZT(53/47) thick films deposited by a dip-coating process", *Microelectronic Engineering,* vol. 66, no. 1-4, pp. 865-871.

He, Z., Ma, J. and Zhang, R. (2004), "Investigation on the microstructure and ferroelectric properties of porous PZT ceramics", *Ceramics International,* vol. 30, no. 7, pp. 1353-1356.

Hsueh, C. H., Luttrell, C. R. and Cui, T. (2006), "Thermal stress analyses of multilayered films on substrates and cantilever beams for micro sensors and actuators", *Journal of Micromechanics and Microengineering,* vol. 16, no. 11, pp. 2509-2515.

Jayasinghe, S. N. and Edirisinghe, M. J. (2002), "Effect of viscosity on the size of relics produced by electrostatic atomization", *Journal of Aerosol Science,* vol. 33, no. 10, pp. 1379-1388.

Jeon, Y., Chung, J. and No, K. (2000), "Fabrication of PZT thick films on silicon substrates for piezoelectric actuator", *Journal of Electroceramics,* vol. 4, no. 1, pp. 195-199.

Jeon, Y. B., Sood, R., Jeong, J. -. and Kim, S. -. (2005), "MEMS power generator with transverse mode thin film PZT", *Sensors and Actuators, A: Physical,* vol. 122, no. 1 SPEC. ISS., pp. 16-22.

Jones, J. L., Kounga, A. B., Aulbach, E. and Granzow, T. (2008), "Domain switching during electromechanical poling in lead zirconate titanate ceramics", *Journal of the American Ceramic Society,* vol. 91, no. 5, pp. 1586-1590.

Jones, J. L., Motahari, S. M., Varlioglu, M., Lienert, U., Bernier, J. V., Hoffman, M. and Üstündag, E. (2007), "Crack tip process zone domain switching in a soft lead zirconate titanate ceramic", *Acta Materialia,* vol. 55, no. 16, pp. 5538-5548.

Kholkin, A. L., Yarmarkin, V. K., Wu, A., Avdeev, M., Vilarinho, P. M. and Baptista, J. L. (2001), "PZT-based piezoelectric composites via a modified sol-gel route", *Journal of the European Ceramic Society,* vol. 21, no. 10-11, pp. 1535-1538.

Kozuka, H. and Takenaka, S. (2002), "Single-step deposition of gel-derived lead zirconate titanate films: Critical thickness and gel film to ceramic film conversion", *Journal of the American Ceramic Society,* vol. 85, no. 11, pp. 2696-2702.

Kumar, B. P., Kumar, H. H. and Kharat, D. K. (2006), "Effect of porosity on dielectric properties and microstructure of porous PZT ceramics", *Materials Science and Engineering B: Solid-State Materials for Advanced Technology,* vol. 127, no. 2-3, pp. 130-133.

Kumazawa, T., Kumagai, Y., Miura, H., Kitano, M. and Kushida, K. (1998), "Effect of external stress on polarization in ferroelectric thin films", *Applied Physics Letters,* vol. 72, no. 5, pp. 608-610.

Kwon, O. J. and Yoon, D. N. (1981), "Closure of isolated pores in liquid phase sintering of W-Ni.", *The International journal of powder metallurgy & powder technology,* vol. 17, no. 2, pp. 127-129, 131.

Láng, G. G. and Seo, M. (2000), "On the electrochemical applications of the bending beam method", *Journal of Electroanalytical Chemistry,* vol. 490, no. 1, pp. 98-101.

Lee, J. -., Park, C. -., Kim, M. and Kim, H. -. (2007), "Effects of residual stress on the electrical properties of PZT films", *Journal of the American Ceramic Society,* vol. 90, no. 4, pp. 1077-1080.

Leite, E. R., Nobre, M. A. L., Longo, E. and Varela, J. A. (1996), "Microstructural development of ZnO varistor during reactive liquid phase sintering", *Journal of Materials Science,* vol. 31, no. 20, pp. 5391-5398.

Li, X., Shih, W. Y., Vartuli, J. S., Milius, D. L., Aksay, I. A. and Shih, W. -. (2002), "Effect of a transverse tensile stress on the electric-field-induced domain reorientation in soft PZT: In situ XRD study", *Journal of the American Ceramic Society,* vol. 85, no. 4, pp. 844-850.

Moulson, A. J. and Herbert, J. M. (1989), *Electroceramics: Materials, Properties, and Applications,* 2nd ed, Routledge, Chichester, UK.

Muralt, P. (1997), "Piezoelectric thin films for mems", *Integrated Ferroelectrics,* vol. 17, no. 1-4, pp. 297-307.

Ohno, T., Malić, B., Fukazawa, H., Wakiya, N., Suzuki, H., Matsuda, T. and Kosec, M. (2008), "Origin of compressive residual stress in alkoxide derived PbTiO3 thin film on Si wafer", *Japanese Journal of Applied Physics,* vol. 47, no. 9 PART 2, pp. 7514-7518.

Ong, R. J., Berfield, T. A., Sottos, N. R. and Payne, D. A. (2005a), "Sol-Gel derived Pb(Zr,Ti)O3 thin films: Residual stress and electrical properties", *Journal of the European Ceramic Society,* vol. 25, no. 12 SPEC. ISS., pp. 2247-2251.

Ong, R. J., Payne, D. A. and Sottos, N. R. (2005b), "Processing effects for integrated PZT: Residual stress, thickness, and dielectric properties", *Journal of the American Ceramic Society,* vol. 88, no. 10, pp. 2839-2847.

Pechini, M. P. (1967), "Method of preparing lead and alkaline earth titanates and niobates and coating method using the same to form a capacitor.", *United States Patent Office,* .

Praveenkumar, B., Kumar, H. H. and Kharat, D. K. (2006), "Study on microstructure, piezoelectric and dielectric properties of 3-3 porous PZT composites", *Journal of Materials Science: Materials in Electronics,* vol. 17, no. 7, pp. 515-518.

Qiu, S., Zheng, X., Gao, C., Gan, X., Chen, J., Yang, C. and Fan, H. (2009), "Pb(Zr0.95Ti0.05)O3 powders and porous ceramics prepared by one-step pyrolysis process using non-aqueous Pechini method.", *Ceramics International,* vol. 35, no. 2, pp. 733-740.

Rahaman, M. N. (1995), *Ceramic Processing and Sintering,* 2nd ed, Marcel Dekker, Inc.

Randall, C. A., Kim, N., Kucera, J. -., Cao, W. and Shrout, T. R. (1998), "Intrinsic and extrinsic size effects in fine-grained morphotropic-phase-boundary lead zirconate titanate ceramics", *Journal of the American Ceramic Society,* vol. 81, no. 3, pp. 677-688.

Rodrigues, S. A. S., Rolo, A. G., Khodorov, A., Pereira, M. and Gomes, M. J. M. (2010), "Determination of residual stress in PZT films produced by laser ablation

with X-ray diffraction and Raman spectroscopy", *Journal of the European Ceramic Society,* vol. 30, no. 2, pp. 521-524.

Sader, J. E. (2001), "Surface stress induced deflections of cantilever plates with applications to the atomic force microscope: Rectangular plates", *Journal of Applied Physics,* vol. 89, no. 5, pp. 2911-2921.

Sangsubun, C., Watcharapasorn, A. and Jiansirisomboon, S. (2009), "Sol-gel derived PZT and PZTN ceramics: A role of sintering temperature", *Ferroelectrics,* vol. 382, no. 1 PART 3, pp. 147-152.

Shaw, T. M. (1986), "Liquid redistribution during liquid-phase sintering.", *Journal of the American Ceramic Society,* vol. 69, no. 1, pp. 27-34.

Shimizu, M., Sugiyama, M., Fujisawa, H. and Shiosaki, T. (1994), "Control of orientation of Pb(Zr, Ti)O3 thin films using PbTiO3 buffer layer", *Japanese Journal of Applied Physics, Part 1: Regular Papers & Short Notes & Review Papers,* vol. 33, no. 9 B, pp. 5167-5171.

Sōmiya, S., Aldinger, F., Claussen, N., Spriggs, R. M., Uchino, K., Koumoto, K. and Kaneno, M. (2003), "Handbook of Advanced Ceramics", .

Stoney, G. G. (1909), "The tension of metallic films deposited by electrolysis.", *Proc. R. Soc. Lond,* vol. 82, pp. 172-175.

Tokumitsu, E., Itani, K., Moon, B. and Ishiwara, H. (1995), "Crystalline quality and electrical properties of PbZrxTi1-xO3 thin films prepared on SrTiO3-covered Si substrates", *Japanese Journal of Applied Physics, Part 1: Regular Papers & Short Notes & Review Papers,* vol. 34, no. 9 B, pp. 5202-5206.

Townsend, P. H., Barnett, D. M. and Brunner, T. A. (1987), "Elastic relationships in layered composite media with approximation for the case of thin films on a thick substrate", *Journal of Applied Physics,* vol. 62, no. 11, pp. 4438-4444.

Tsai, C. -., Chu, S. -. and Lu, C. -. (2009), "Doping effects of CuO additives on the properties of low-temperature- sintered PMnN-PZT-based piezoelectric ceramics and their applications on surface acoustic wave devices", *IEEE transactions on ultrasonics, ferroelectrics, and frequency control,* vol. 56, no. 3, pp. 660-668.

Tuttle B.A., Garino T.J., Voig, J. A., Headley T.J., Dimos D. and Eatough M.O. (1995), "Relationships between ferroelectric 90° domain formation and electrical properties of chemically prepared Pb(Zr, Ti)O3 thin films.", *Science and Technology of Electroceramic Thin Films,* , pp. 117.

Van Werde, K., Vanhoyland, G., Mondelaers, D., Den Rul, H., Van Bael, M. K., Mullens, J. and Van Poucke, L. C. (2007), "The aqueous solution-gel synthesis of perovskite Pb(Zr1-x, Tix)O3 (PZT", *Journal of Materials Science,* vol. 42, no. 2, pp. 624-632.

Wang, D., Edirisinghe, M. J. and Dorey, R. A. (2008), "Formation of PZT crack-free thick films by electrohydrodynamic atomization deposition", *Journal of the European Ceramic Society,* vol. 28, no. 14, pp. 2739-2745.

Wang, D., Rocks, S. A. and Dorey, R. A. (2009), "Micromoulding of PZT film structures using electrohydrodynamic atomization mould filling", *Journal of the European Ceramic Society,* vol. In Press, Corrected Proof.

Wang, Z., Zhu, W., Zhao, C. and Tan, O. K. (2003), "Dense PZT thick films derived from sol-gel based nanocomposite process", *Materials Science and Engineering B: Solid-State Materials for Advanced Technology,* vol. 99, no. 1-3, pp. 56-62.

Wang, X. and Atkinson, A. (2007), "Piezo-spectroscopic mapping of the thermally grown oxide in thermal barrier coatings", *Materials Science and Engineering A,* vol. 465, no. 1-2, pp. 49-58.

Whatmore, R. W. (1999), "Ferroelectrics, microsystems and nanotechnology", *Ferroelectrics,* vol. 225, no. 1-4, pp. 179-192.

Wright, G. J. and Yeomans, J. A. (2008), "The influence of screen-printing parameters on the microstructure and gas permeance of a zirconia electrolyte", *Journal of the European Ceramic Society,* vol. 28, no. 4, pp. 779-785.

Wu, A., Miranda Salvado, I. M., Vilarinho, P. M. and Baptista, J. L. (1998), "Lead zirconate titanate prepared from different zirconium and titanium precursors by sol-gel", *Journal of the American Ceramic Society,* vol. 81, no. 10, pp. 2640-2644.

Wu, D., Zhou, Q., Shung, K. K., Bharadwaja, S. N., Zhang, D. and Zheng, H. (2009), "Dielectric and piezoelectric properties of PZT composite thick films with variable solution to powder ratios", *Journal of the American Ceramic Society,* vol. 92, no. 6, pp. 1276-1279.

Wurst, J. C. and Nelson, J. A. (1972), "Linear intercept technique for measuring grain size in two-phase polycrystalline ceramics ", *J. Am. Ceram. So,* vol. 55, pp. 109.

Xie, J., Hu, M., Ling, S. and Du, H. (2006), "Fabrication and characterization of piezoelectric cantilever for micro transducers", *Sensors and Actuators A: Physical,* vol. 126, no. 1, pp. 182-186.

Yang, A., Wang, C. -., Guo, R. and Huang, Y. (2010), "Microstructure and electrical properties of porous PZT ceramics fabricated by different methods", *Journal of the American Ceramic Society,* vol. 93, no. 7, pp. 1984-1990.

Yu, Y. H., Lai, M. O., Lu, L. and Yang, P. (2008), "Measurement of residual stress of PZT thin film on Si(1 0 0) by synchrotron X-ray rocking curve technique", *Journal of Alloys and Compounds,* vol. 449, no. 1-2, pp. 56-59.

Zaghete, M. A., Varela, J. A., Cilense, M., Paiva-Santos, C. O., Las, W. C. and Longo, E. (1999), "Effect of isostructural seeding on the microstructure and piezoelectric properties of PZT ceramics", *Ceramics International,* vol. 25, no. 3, pp. 239-244.

Zhang, Y. and Zhao, Y. -. (2006), "Applicability range of Stoney's formula and modified formulas for a film/substrate bilayer", *Journal of Applied Physics,* vol. 99, no. 5.

Zhang, Q. M., Pan, W. Y., Jang, S. J. and Cross, L. E. (1988), "Domain wall excitations and their contributions to the weak-signal response of doped lead zirconate titanate ceramics", *Journal of Applied Physics,* vol. 64, no. 11, pp. 6445-6451.

Zhao, J. -., Ryan, T., Ho, P. S., McKerrow, A. J. and Shih, W. -. (1999), "Measurement of elastic modulus, Poisson ratio, and coefficient of thermal expansion of on-wafer submicron films", *Journal of Applied Physics,* vol. 85, no. 9, pp. 6421-6424.

Zheng, X., Li, J. and Zhou, Y. (2004), "X-ray diffraction measurement of residual stress in PZT thin films prepared by pulsed laser deposition", *Acta Materialia,* vol. 52, no. 11, pp. 3313-3322.

Zhou, Y. C., Yang, Z. Y. and Zheng, X. J. (2003), "Residual stress in PZT thin films prepared by pulsed laser deposition", *Surface and Coatings Technology,* vol. 162, no. 2-3, pp. 202-211.